Max-Planck-Institut
für Meteorologie

MAX-PLANCK-GESELLSCHAFT

International Max Planck Research School
on Earth System Modelling

Internal tides simulated by a 1/10° OGCM

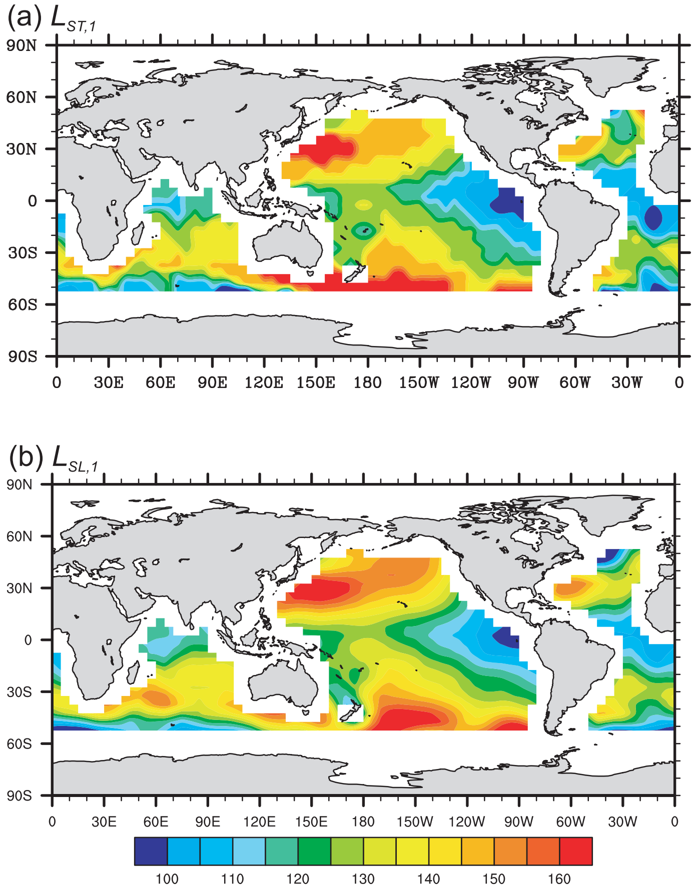
(a) $L_{ST,1}$
90N
60N
30N
0
30S
60S
90S
0
30E
60E
90E
120E
150E
180
150W
120W
90W
60W
30W
0
(b) $L_{SL,1}$
100
110
120
130
140
150
160

Zhuhua Li

Hamburg 2016

Berichte zur Erdsystemforschung
Reports on Earth System Science

179
2016

Hinweis

Die Berichte zur Erdsystemforschung werden vom Max-Planck-Institut für Meteorologie in Hamburg in unregelmäßiger Abfolge herausgegeben.

Sie enthalten wissenschaftliche und technische Beiträge, inklusive Dissertationen.

Die Beiträge geben nicht notwendigerweise die Auffassung des Instituts wieder.

Die "Berichte zur Erdsystemforschung" führen die vorherigen Reihen "Reports" und "Examensarbeiten" weiter.

Anschrift / Address

Max-Planck-Institut für Meteorologie
Bundesstrasse 53
20146 Hamburg
Deutschland

Tel./Phone: +49 (0)40 4 11 73 - 0
Fax: +49 (0)40 4 11 73 - 298

name.surname@mpimet.mpg.de
www.mpimet.mpg.de

Notice

The Reports on Earth System Science are published by the Max Planck Institute for Meteorology in Hamburg. They appear in irregular intervals.

They contain scientific and technical contributions, including Ph. D. theses.

The Reports do not necessarily reflect the opinion of the Institute.

The "Reports on Earth System Science" continue the former "Reports" and "Examensarbeiten" of the Max Planck Institute.

Layout

Bettina Diallo and Norbert P. Noreiks
Communication

Copyright

Photos below: ©MPI-M
Photos on the back from left to right:
Christian Klepp, Jochem Marotzke,
Christian Klepp, Clotilde Dubois,
Christian Klepp, Katsumasa Tanaka

Internal tides simulated by a 1/10° OGCM

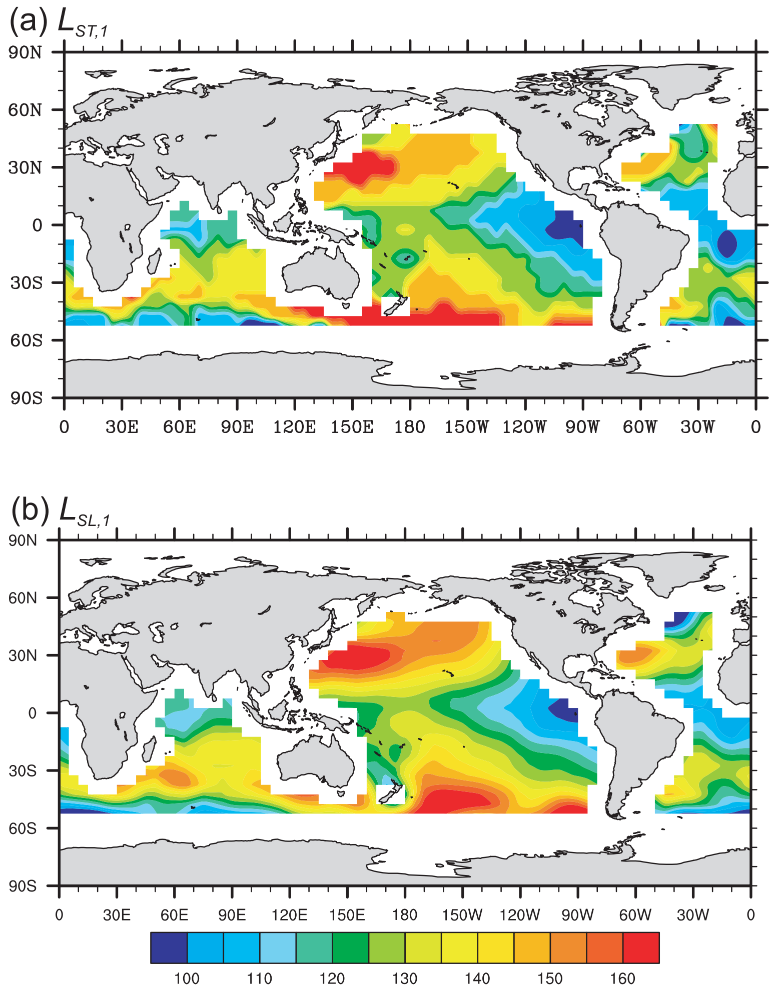
(a) $L_{ST,1}$
90N
60N
30N
0
30S
60S
90S
0
30E
60E
90E
120E
150E
180
150W
120W
90W
60W
30W
0
(b) $L_{SL,1}$
90N
60N
30N
0
30S
60S
90S
0
30E
60E
90E
120E
150E
180
150W
120W
90W
60W
30W
0
100
110
120
130
140
150
160

Dissertation with the aim of achieving a doctoral degree
at the Faculty of Mathematics, Informatics and Natural Sciences
Department of Earth Sciences of Universität Hamburg

submitted by

Zhuhua Li

Hamburg 2016

Zhuhua Li

Max-Planck-Institut für Meteorologie
Bundesstrasse 53
20146 Hamburg

Tag der Disputation: 26.4.2016

Folgende Gutachter empfehlen die Annahme der Dissertation:

Dr. Jin-Song von Storch
Prof. Dr. Carsten Eden

Berichte zur Erdsystemforschung / Max-Planck-Institut für Meteorologie 179
Reports on Earth System Science / Max Planck Institute for Meteorology 2016

ISSN 1614-1199

Abstract

Diapycnal mixing is a major candidate in maintaining the large-scale meridional overturning circulation in the ocean, attributed principally to the breaking of internal waves, with winds and tides serving as the primary wave sources. As a first step to accurately estimate how much tidal energy is fed into turbulent mixing, it is crucial to achieve a detailed understanding of the low-mode internal tides, the most energetic part of internal tides. On the other hand, to study submesoscale variability by the next generation altimeter mission SWOT, the low-mode internal tides having larger length scales need to be predicted and removed, for which detailed quantification are required for these waves, whose signatures in the surface elevations are most evident.

In this thesis, a concurrent simulation of the eddying general circulation, barotropic and internal tides with the 1/10° STORMTIDE model is used to derive a near-global quantification of the freely propagating low-mode internal tides of the M_2 and K_1 tidal constituents. The three-dimensional baroclinic tidal velocities are analyzed by using the wavenumber spectral analysis. Thus, the low modes of internal tides are separated by a detailed analysis of spectral peaks of the wavenumber spectrum, and are quantified by the resulting wavelengths. The results are compared with solutions of the Sturm-Liouville eigenvalue problem and of the eigenvalue problem further simplified by the WKB approximation.

Two modes of the M_2 internal tide are captured in our model, ranging within 100-160 km and 45-80 km for mode 1 and 2, respectively. Due to the larger length scales of the K_1 internal tide, three modes (mode 1 to 3) are captured, presenting the ranges of 200-400 km, 100-200 km, 60-120 km, respectively. All modes of the M_2 and K_1 internal tides reveal, to different degrees, a zonal asymmetry and a poleward increase of the wavelengths. The largest magnitudes and the strongest spatial variations of the wavelengths occur in the Pacific, with larger values in the western than in the eastern Pacific for both tidal constituents.

The magnitudes and geographical distributions of the tidal constituents compare well with those from the standard Sturm-Liouville eigenvalue problem. Hence, the simulated internal tides are, to the first approximation, linear internal waves that satisfy the local dispersion relation. Since the Sturm-Liouville eigenvalue problem depends only on the Coriolis frequency f and stratification N, the observed zonal asymmetry and poleward increase are accounted for by the effect of N and f, respectively. The mode-1 M_2 internal tides are determined by both, whereas the mode-2 M_2 internal tides are controlled primarily by N only. The K_1 internal tides are determined by the combined role of N and f, with the f-effect being dominant.

The WKB-simplified Sturm-Liouville eigenvalue problem presents the relative discrepancies up to 15% when compared with the standard Sturm-Liouville eigenvalue problem. Hence, neglecting the details of the vertical variations of N could be problematic in deriving the wavelengths in the near-global ocean for the M_2 and K_1 internal tides, although smaller relative discrepancies are found in certain regions.

The presence of the K_1 critical latitude at 30° in this high-resolution simulation enables us to investigate the vertical energy distributions of the freely propagating and bottom-trapped K_1 internal tides. The STORMTIDE model is capable of capturing the different characteristics of the K_1 internal tides in the vertical that are the surface concentration and the bottom amplification of the kinetic energy in sub- and supercritical latitudes, respectively. The kinetic energy is stronger in shallower than deeper ocean regions both equatorward and poleward of 30°. A strong decreasing rate of the bottom-amplified K_1 kinetic energy and a further upward energy reduction above the level of energy minima are present in shallow waters poleward of 30°.

Zusammenfassung

Diapyknische Vermischung spielt eine große Rolle in der Aufrechterhaltung der großskaligen Meridionalen Umwälzbewegung im Ozean, hauptsächlich durch das Brechen von internen Wellen, die durch Winde und Gezeiten entstehen. Um möglichst genau abschätzen zu können, wie viel Gezeitenenergie der turbulenten Vermischung zugeführt wird, ist ein genaues Verständnis der „low-mode“ internen Gezeiten, dem energiereichsten Teil der internen Gezeiten, von großer Bedeutung. Um submesoskalige Variabilität mit der Altimetermission der Zukunft, SWOT, untersuchen zu können, müssen andererseits die low-mode internen Gezeiten mit größeren Längenskalen prognostiziert und abgezogen werden. Dafür ist eine genaue Quantifizierung dieser Wellen, dessen Rolle sich in der Wasserspiegelhöhe klar abzeichnet, notwendig.

In dieser Doktorarbeit wird eine gemeinsame Simulation der turbulenten allgemeinen Zirkulation und der barotropen und internen Gezeiten mit dem 1/10° STORMTIDE Modell genutzt, um die frei propagierenden low-mode internen Gezeiten der M_2 und K_1 Komponenten der Gezeiten beinahe global zu quantifizieren. Die dreidimensionalen baroklinen Gezeitengeschwindigkeiten werden mithilfe von spektraler Wellenzahlanalyse untersucht. Daher werden die „low modes“ (oder „niedere Moden“) der internen Gezeiten mit einer genauen Analyse der Spektrallinien eines Wellenzahlspektrums heraus gesucht und mit der resultierenden Wellenlänge quantifiziert. Die Ergebnisse werden mit dem Sturm-Liouville Eigenwertproblem und dem mit der WKB-Näherung weiter vereinfachten Eigenwertproblem verglichen.

Zwei Moden der M_2 internen Gezeiten werden von unserem Modell erfasst: von 100-160 km und 45-80 km für Mode 1, bzw. Mode 2. Da die K_1 internen Gezeiten eine größere Längenskala haben, werden hier drei Moden erfasst (Mode 1 bis 3), die entsprechend von 200-400 km, von 100-200 km und von 60-120 km reichen. Alle Moden der M_2 und K_1 internen Gezeiten zeigen, im verschiedenen Maße, eine zonale Asymmetrie und eine polwärtige Zunahme der Wellenlängen. Die größten Wellenlängen und die

mit den meisten räumlichen Abweichungen treten im Pazifik auf, mit größeren Werten im West- als im Ost-Pazifik für beide Komponenten der Gezeiten.

Die Größenordnungen und die geographischen Verteilungen der Gezeitenkomponenten sind gut mit denen aus dem ursprünglichen Sturm-Liouville Eigenwertproblem vergleichbar. Daher sind die simulierten internen Gezeiten in erster Näherung lineare interne Wellen, die die lokale Dispersionsrelation erfüllen. Da das Sturm-Liouville Eigenwertproblem nur von der Coriolisfrequenz f und der Schichtung N abhängt, resultiert die beobachtete zonale Asymmetrie und die polwärtige Zunahme aus dem Effekt von f bzw. von N. Die Mode-1 M_2 internen Gezeiten werden von beiden bestimmt, während die Mode-2 M_2 internen Gezeiten hauptsächlich von N alleine kontrolliert werden. Die K_1 internen Gezeiten werden von dem gemeinsamen Effekt von N und f bestimmt, wobei der Effekt von f dominiert.

Das WKB-vereinfachte Sturm-Liouville Eigenwertproblem zeigt relative Abweichungen von bis zu 15% im Vergleich zu dem ursprünglichen Sturm-Liouville Eigenwertproblem. Daher könnte es problematisch sein, Einzelheiten der vertikalen Variation von N beim Ableiten der Wellenlängen im beinahe globalen Ozean für die M_2 und K_1 internen Gezeiten zu vernachlässigen, obwohl einige Regionen kleinere relative Abweichungen zeigen.

Die Anwesenheit des K_1 kritischen Breitengrades bei 30° in dieser hoch aufgelösten Simulation erlaubt es uns die vertikale Energieverteilung der frei propagierenden und der am Boden gefangenen K_1 internen Gezeiten zu untersuchen. Das STORMTIDE Modell ist in der Lage die unterschiedlichen Eigenschaften der K_1 internen Gezeiten in der Vertikalen, das heißt die Oberflächenkonzentration und die Bodenverstärkung der kinetischen Energie in unter- bzw. über-kritischen Breiten, zu erfassen. Die kinetische Energie ist stärker in flacheren als in tieferen Ozeanregionen äquator- und auch polwärts von 30°. Eine starke Abnahme der bodenverstärkten K_1 kinetischen Energie und weiter oben eine Energieabnahme oberhalb des Levels der Energieminima kommt in flachen Gewässern polwärts von 30° vor.

Contents

1 Introduction **1**

1.1 Motivation 1

1.2 Thesis objective 10

1.3 Outline of the thesis 11

2 The M_2 internal tide simulated by a 1/10° OGCM **13**

2.1 Introduction 14

2.2 The STORMTIDE model 16

2.3 Methods 20

2.3.1 Details in deriving the baroclinic M_2 tidal velocities 20

2.3.2 Two-dimensional wavenumber spectral analysis 21

2.3.3 The Sturm-Liouville eigenvalue problem 23

2.3.4 The WKB-simplified eigenvalue problem 25

2.4 Kinetic energy of the M_2 internal tide 25

2.5 Wavelengths of the model-simulated M_2 internal tide 28

2.5.1 Characteristics of wavenumber spectra 28

2.5.2 Geographical distribution of wavelengths 32

2.5.3 Comparison with the distribution obtained by solving the eigenvalue problem 33

2.6 Relative roles of N and f in determining the wavelengths 36

2.7 Applicability of the WKB-simplified eigenvalue problem 41

2.8 Concluding remarks 43

3 The K_1 internal tide simulated by a 1/10° OGCM **45**

3.1 Introduction 46
3.2 Kinetic energy of the K_1 internal tide 50
3.3 Wavelengths of the model-simulated K_1 internal tide 52
    3.3.1 Characteristics of the wavenumber spectra 52
    3.3.2 Geographical distributions of the K_1 wavelengths 61
    3.3.3 Comparison with the distributions obtained by solving the eigenvalue problem 67
    3.3.4 Relative roles of N and f in determining the wavelengths 70
3.4 Application of the WKB-simplified eigenvalue problem 72
3.5 Role of the critical latitude 73
    3.5.1 Kinetic energy section of the propagating K_1 internal tide 73
    3.5.2 Kinetic energy section of the trapped K_1 internal tide 77
    3.5.3 Bottom energy distributions of the K_1 internal tide 78
3.6 Concluding remarks 82

4 Concluding remarks and outlook **89**
4.1 Concluding remarks 89
4.2 Outlook 93

Appendix A Remarks on the methods **95**
A.1 Two-dimensional wavenumber spectral analysis of the previous method . 95
A.2 Discussions concerning two methods 96

Appendix B Comparisons of $L_{SL,1}$ from model-simulated and observational N **101**

Appendix C Effect of the model resolution on internal tide simulation **105**

Bibliography **109**

List of Figures **123**

List of Tables **133**

Acknowledgements **135**

Publications **137**

Chapter 1

Introduction

1.1 Motivation

The meridional overturning circulation (MOC) exerts a significant impact on both modern and ancient climate and climate variability (e.g., Rahmstorf 2006; Marshall and Speer 2012, and references therein) due to its significant role in transporting heat, fresh water and carbon. It is thus crucial to identify the physical mechanisms that drive the MOC and diagnose its sensitivity to variations of external driving forces, which determines its further evolution and responses to the continued global climate change. Discussions on the drivers of the MOC starts from the consideration of buoyancy forcing. The tank experiments carried out by Sandström (1908) suggest that a deeper heating source than the cooling is necessary in driving the overturning circulation in the absence of other external forcing mechanisms. In reality, however, heating and cooling both occur at the ocean surface at roughly the same level, which alone enables merely a surface-intensified circulation driven by very weak convection, but is impossible to drive a deep overturning circulation. Due to heat losses to the atmosphere and salt rejection during the sea ice growth, dense waters are continuously formed and sink to great depths in high latitudes, leading to an increase of the water density. The buoyancy forcing is, however, pointed out to provide too less energy to efficiently drive the MOC (Oort et al. 1994; Faller 1966). Other mechanisms are thus required to reduce the density of the waters in order to sustain the density balance. The only possible mechanical energy sources are believed to be winds and tides (Munk and Wunsch 1998).

There are two main candidates for driving the steady state MOC, diapycnal mixing (causing water parcels to cross the surfaces of equal density) and winds (e.g., Munk and Wunsch 1998; Kuhlbrodt et al. 2007; Marshall and Speer 2012), as depicted in Fig. 1.1. The former is the energy feeding into turbulent motions from winds and tides via the breaking of the resulting internal waves, at work primarily in low latitudes, and the latter is the direct kinetic energy input to the large-scale motions which is further converted to the potential energy via upwelling, occurring mainly in the Southern Ocean. Note that the regions for dense water formation are rather small and localized compared to the wide spreading of upwelling. A detailed description of these driving processes is found in Kuhlbrodt et al. (2007), with an emphasis on the wind-driven upwelling in Marshall and Speer (2012). Here we will only focus on the mechanism of diapycnal mixing, whose key role in maintaining the Atlantic MOC (AMOC) is outlined, for instance, in Zickfeld et al. (2007), but is still not fully understood.

Given diapycnal mixing as the principal forcing to return deep dense waters back to the surface, about 0.4 Terawatt (TW; 1 TW = 10^{12} W) of the power supply would be required to balance a rough estimate of the global deep water formation rate of 30 SV (1 SV = 10^6 m^3 s^{-1}) through the mixing-driven upwelling (Munk and Wunsch 1998; Wunsch and Ferrari 2004). Taking into account the widely used value of the mixing efficiency 0.2 (Osborn 1980), 2 TW of the power supply from winds and tides is thus required. Only 20% of the injected energy to turbulence is converted from turbulent kinetic energy to the potential energy through the buoyancy flux, whereas the rest is dissipated to the production of heat. This estimate of the power supply is consistent with estimates of the amount of energy available from winds and tides in the deep ocean, where each is contributing approximately 1 TW (Munk and Wunsch 1998; Egbert and Ray 2000; Wunsch and Ferrari 2004; Kuhlbrodt et al. 2007). However, large uncertainty is involved in the estimate (Munk and Wunsch 1998).

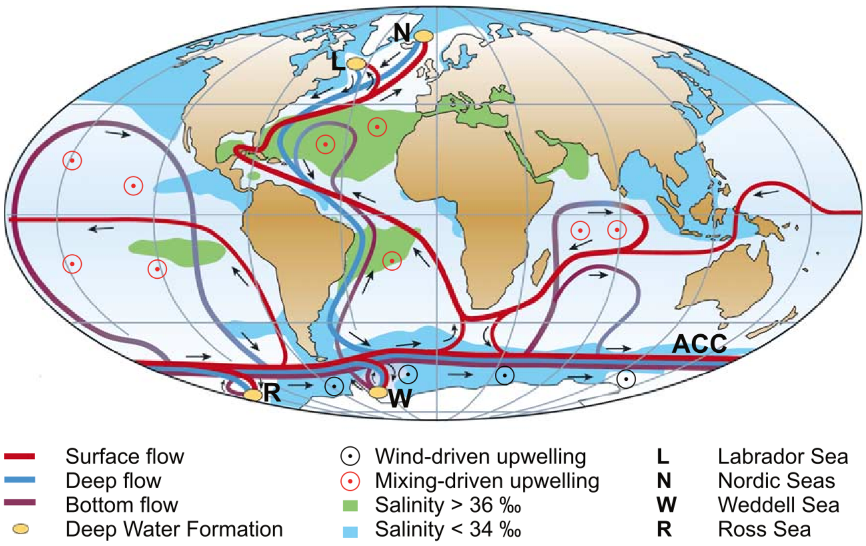
N
L
ACC
R
W
Surface flow
Deep flow
Bottom flow
Deep Water Formation
Wind-driven upwelling
Mixing-driven upwelling
Salinity > 36 ‰
Salinity < 34 ‰
L Labrador Sea
N Nordic Seas
W Weddell Sea
R Ross Sea

Figure 1.1: Simplified sketch of the global overturning circulation system. Surface currents are shown in red, deep waters in light blue and bottom waters in brown. From Kuhlbrodt et al. (2007).

The energy pathways of winds and tides and the associated energetics are sketched in Fig. 1.2, indicating the key role of internal waves in the energy cascade from winds and tides to turbulent mixing. Freely propagating internal waves can only exist with a frequency ω satisfying $f \leqslant \omega \leqslant N$ in the stratified ocean, with f and N being the Coriolis and buoyancy frequencies, respectively. These waves are energetic in a finite frequency bandwidth between f and N, but they become much weaker in the spectral energy beyond this range (Fig. 1.3). Particularly energetic motions are found at the near-inertial and tidal frequencies, named the near-inertial internal waves and internal tides, respectively. These waves are well rising above the rest of the spectrum between f and N, which is called the continuum of internal wave spectrum.

Winds provide the main energy source for the generation of the near-inertial waves (NIWs) with the frequency band located at around 1.0-1.2f (Alford et al. 2016), with other possible forcing mechanisms discussed in the latest review by Alford et al. (2016). The winds exert the forcing directly at the sea surface, exciting inertial waves, or called inertial oscillations that are currents rotating at the local f in the mixed layer. These

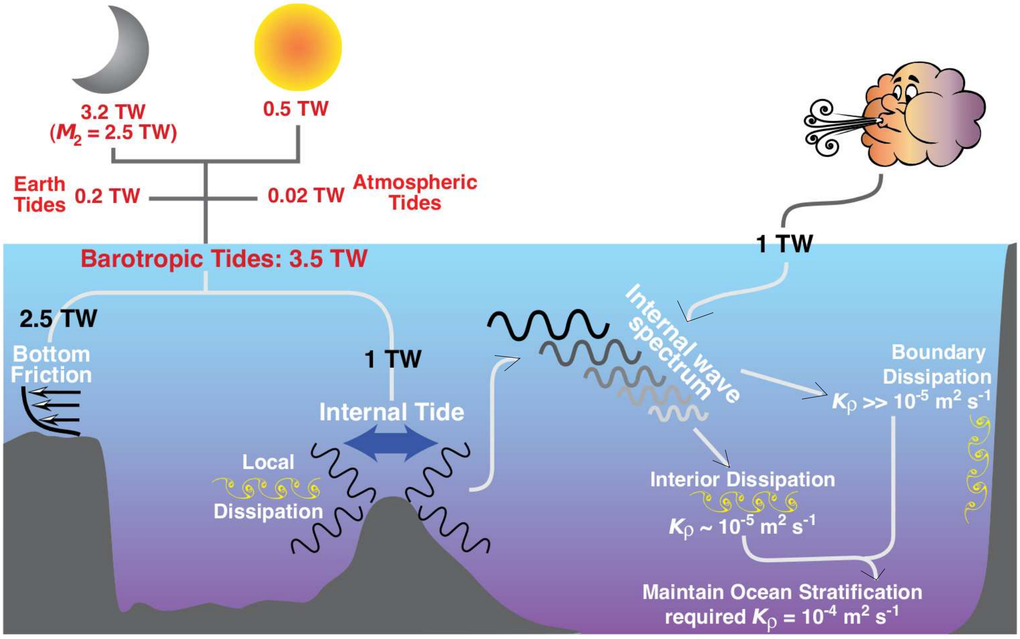
3.2 TW
(M_2 = 2.5 TW)
0.5 TW
Earth Tides
0.2 TW
0.02 TW
Atmospheric Tides
Barotropic Tides: 3.5 TW
1 TW
2.5 TW
Bottom Friction
1 TW
Internal Tide
Local
Dissipation
Internal wave spectrum
Boundary Dissipation
$K_\rho >> 10^{-5}$ m^2 s^{-1}
Interior Dissipation
$K_\rho \sim 10^{-5}$ m^2 s^{-1}
Maintain Ocean Stratification
required $K_\rho = 10^{-4}$ m^2 s^{-1}

Figure 1.2: Schematic of energy pathways in the ocean. Astronomical forcing generates barotropic tides (3.5 TW) primarily in the ocean, with 2.5 TW of barotropic tidal energy lost to bottom friction in shallow seas. Approximately 1 TW is converted to internal tides in the deep ocean, most of which enters the internal-wave-driven energy cascade from large scales to mixing scales. The wind provides about 1 TW into the internal wave spectrum. From Carter et al. (2012).

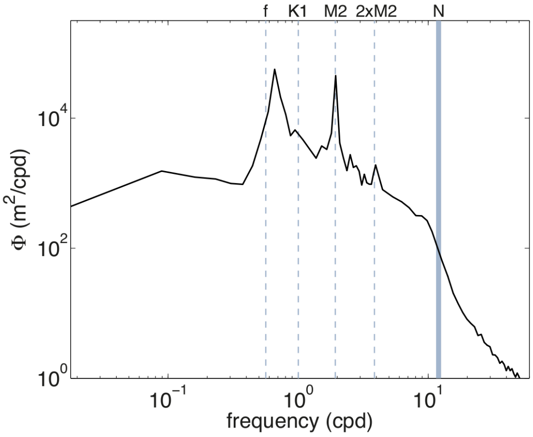

Figure 1.3: Time-mean spectrum of vertical displacements measured at approximately 3200 m in the open ocean. The Coriolis frequency f and the buoyancy frequency N denote the range where freely propagating energetic internal waves can exist. Additional vertical dashed lines represent the main internal tidal constituents that are the principal lunar semidiurnal tide M_2, the diurnal tide K_1 and the compound tide M_4 ($=2\times\mathrm{M}_2$) of the semidiurnal tide. From Köhler (2013).

waves are mostly vigorously generated under sudden wind events, for instance, storm and cyclone tracks, near their critical latitudes, and propagate equatorward in the horizontal (Garrett 2001). The wind-generated power input to the near-inertial motions is, however, still under debate. The value is suggested to be around 0.3-0.7 TW based on the slab ocean models, which is estimated by using the realistic wind stress products and simplified ocean dynamics (Alford 2001; Watanabe and Hibiya 2002; Alford 2003), and to be 0.4 TW on a basis of the general circulation model estimation (Furuichi et al. 2008; Simmons and Alford 2012; Jochum et al. 2013). By applying various temporal and spatial resolutions of wind stress forcing to a global eddy-permitting ocean general circulation model (Rimac et al. 2013), the value of the wind power input into the NIWs is suggested to be 0.3-1.1 TW, with the temporal variations predominant over the spatial variations in the wind stress field.

These NIWs are partly dissipated in the oceanic mixed layer, where they are generated, via turbulent mixing, whilst the rest propagates horizontally towards the equator and vertically slowly into the deep ocean. Only the energy escaping from the turbulent mixed layer can freely propagate and exist in the stratified ocean as near-inertial internal gravity waves. The breaking of these waves provides energy for deep ocean turbulent mixing and thus for the large-scale overturning circulation. Only a small fraction, 10-25%, of the wind-induced near-inertial energy flux is found to pass through the mixed surface layer and be injected into the ocean's interior, based on estimates of the ocean general circulation models with constant mixed layer depths for limited area (Furuichi et al. 2008; Zhai et al. 2009). When diagnosing with spatially and temporally varying mixed layer depth in the global ocean (Rimac 2014), there is only 10.8% of the wind power input, amounting to approximate 0.037 TW, radiating into the ocean's interior. It indicates the necessity for other energy sources for deep mixing. Hence, in the following, we will focus on the second major energy source for deep ocean mixing induced by ocean tides.

Oceanic barotropic tides, a significant component of oceanic motions, are generated by the gravitational force from the sun and moon on the whole water body, causing the uniform movement of the entire water column. Owing to their uniform vertical structure, barotropic tides are widely simulated by numerical tide-only models that are based on shallow water equations with realistic geometry and bathymetry applied. In order to compute ocean tides with the highest accuracy possible, data assimilation techniques were developed to include observations from tide gauges (Parke and Hendershott 1980; Schwiderski 1980) and satellite altimetry (Cartwright and Ray 1990). The ocean tide products from those models are used for tidal corrections in geodetic observations and in particular for altimetry and gravity satellite observations (Plag and Perlman 2009). Furthermore, various purely hydrodynamic global tide models, unconstrained by observations (referred to as ”forward”, ”unconstrained”, or ”non-data-assimilating” models), have been developed, (e.g., Jayne and St. Laurent 2001; Carrère and Lyard 2003; Egbert et al. 2004). The accuracy of global barotropic tide models, including constrained and unconstrained model approaches, is comprehensively assessed against various tidal observations in Stammer et al. (2014). In the deep ocean, ocean models have the highest accuracy in the representation of the barotropic tidal elevation. In coastal regions and in high-latitude regions, models show larger errors, mainly due to stronger nonlinear effects and a reduced availability of satellite observations.

Apart from causing the rise and fall of the sea level, barotropic tides also impact the ocean circulation via tidal currents (rather than tidal elevations). One way to diagnose this effect is by implementing tides in general ocean circulation models and perform concurrent simulations of tides and circulation (Schiller and Fiedler 2007; Müller et al. 2010). In these first attempts with the coarse-resolution (O(100 km)) models, the tidal currents and circulation interact via nonlinear bottom friction and by increased vertical velocity shear induced by strong tidal currents. This effect is at work principally in shallow seas (e.g., Egbert and Ray 2003), but is insignificant in the deep ocean as a result of the rather weak tidal current velocities (e.g., Jayne and St. Laurent 2001). Due to the low-resolution used in these models (Schiller and Fiedler 2007; Müller et al. 2010), internal tides, widely accepted as the principal mechanism for tidal dissipation in the deep ocean, cannot be resolved. Their effect on diapycnal mixing is commonly missed in the coarse-resolution model studies.

Diapycnal diffusivity is used to quantify turbulent mixing across the surfaces of equal density that has an essential control on the MOC, and was initially widely accepted to be constant [10^{-4} m^2 s^{-1} in Munk (1966)], indicating an uniform distribution of the slow upwelling over large regions in the ocean (Stommel and Arons 1959). It is, however, challenged by observations. Diffusivity is found to be rather weak in the vast regions of the ocean's interior, with the value around 10^{-5} m^2 s^{-1} (Moum and Osborn 1986; Ledwell et al. 1993; Gregg et al. 2003), and several orders of magnitude larger near rough topography or continental slopes (Polzin et al. 1997; Ledwell et al. 2000; Moum et al. 2002; Garabato et al. 2004). Hence, diapycnal diffusivity is revealed by observations to be strongly spatially variable.

In numerical ocean models, a uniform value of diffusivity (around 10^{-5} m^2 s^{-1}) is commonly applied, accounting for the weak interior mixing caused by nonlocal sources, primarily due to internal waves (Munk and Wunsch 1998). As a major component of internal waves, internal tides that radiate away and dissipate remotely from the generation sites contribute largely to this weak background mixing. Part of internal tides is, however, dissipated locally near the topography features, enhancing the bottom mixing there. Hence, diapycnal diffusivity associated with tides has a strong horizontal variability, with small values over a vast smoothing area and large values near rough topography. This horizontal variability is, however, not taken into account in many ocean general circulation models (OGCMs). The modified Bryan and Lewis scheme (Bryan and Lewis 1979) is instead commonly employed, which presents a horizontal homogeneous, but vertically varying profile, and represents the background mixing primarily related to the breaking internal tides that radiate away from the original sources. There is, however, no observational evidence for the horizontal homogeneity in diapycnal diffusivity. The horizontal inhomogeneity is thus further considered in some models (e.g., Hasumi and Suginohara 1999; Huang and Jin 2002), but the energy constraint supplied by tides to the deep ocean is neglected.

Tidal mixing parameterization that is energetically constrained is proposed by St. Laurent and Garrett (2002), which describes the mixing of internal tides at their generation sites. The energy conversion from barotropic to internal tides needs to be specified in this parameterization, 30% of which, corresponding to the high-mode internal tides, is considered to contribute to the locally elevated tidal mixing over rough topography in the deep ocean. This parameterization has been employed by several studies in the ocean/climate models (Simmons et al. 2004b; Saenko and Merryfield 2005; Saenko 2006; Jayne 2009; Exarchou et al. 2012, 2014), in which tidal mixing induced by internal tides cannot be resolved directly. Note that due to a lack of an overall precise parameterization of turbulent motions with the large-scale quantities that are resolvable in the OGCMs, diapycnal diffusivity is often treated as a tunning parameter in numerical models for a better simulation of the large-scale observable quantities. In contrast, tidal mixing in this parameterization (St. Laurent and Garrett 2002) is allowed to evolve with the model state, both spatially and temporally. By replacing the uniform diapycnal diffusivity or the horizontally uniform but bottom-intensified profile, the spatially varying diffusivity is taken into account, which is associated with the localized intensified tidal mixing over rough topography in the deep ocean. These results reveal a significant impact of tidal mixing on the simulated MOC, in particular on the deep MOC, and on the responses of simulated climate to atmospheric CO_2 increase, and reveal also a remarkable improvement of the ocean state.

The low-mode internal tides are considered to be standing waves in the vertical, superposed by the waves and their reflection from the surface. These waves have a larger spatial scale than high modes, and mainly radiate away from the generation sites and propagate into the ocean's interior (e.g. Alford 2003). They are observed to be able to propagate over 1000 km away from their original sources (Ray and Mitchum 1996) and contribute to the background mixing when they break (Fig. 1.2) (e.g., Munk and Wunsch 1998; Exarchou et al. 2012). The low- and high-mode internal tides both contribute to the mixing in the open ocean, providing approximately 1 TW power to the deep ocean (Munk and Wunsch 1998; Egbert and Ray 2003). In the state-of-the-art tidal mixing parameterization (St. Laurent and Garrett 2002), however, only high modes that account for 30% of internal tide energy converted from barotropic tides in the open ocean are taken into account. The other 70% associated with low modes is left unspecified, but only strongly simplified in the contribution to the weak background mixing. Since the low-mode internal tides possess the major part of internal wave energy, it is crucial to take their detailed effect on mixing into account. To understand this process, we need to better understand the low-mode internal tides in a realistic setting with realistic stratification and circulation. The concurrent simulation of the circulation and tides (barotropic and internal tides) is thus vital to bring us the required knowledge.

The global concurrent simulation of eddying general circulation and barotropic and internal tides is first reported in Arbic et al. (2010) by using the HYbrid Coordinate Ocean Model (HYCOM). The simulated three-dimensional total tidal currents are evaluated by the historical current meter measurements (Timko et al. 2013), while the internal tide signatures on sea surface elevations are evaluated by along-track altimeter data (Shriver et al. 2012), whose stationarity is estimated in Shriver et al. (2014). All these evaluations show the skill of the HYCOM in simulating internal tides. The scientific applications of the HYCOM are also carried out by Richman et al. (2012) for the impact of internal waves on sea surface height wavenumber spectra and by Müller et al. (2015) for the internal wave kinetic energy spectra and nonlinear interactions. Müller et al. (2012) present another high-resolution concurrent simulation of circulation, eddies and barotropic and internal tides by the STORMTIDE model (details of this model described in Chapter 2), with an evaluation of the simulated barotropic tides compared to tidal gauges and internal tide signatures compared to altimeter data. In this thesis, we take into account the three-dimensional baroclinic tidal current velocities, which are not available from satellite altimeter data. These velocities are then analyzed by performing the two-dimensional wavenumber spectral analysis in order to gain the detailed quantification of the simulated low-mode M_2 and K_1 internal tides in the deep ocean.

The internal tide signatures on the sea surface height are observed in the satellite altimeter data, to which low modes are the major contributors. Since the next generation altimeter missions aim at studying submesoscale motions, internal tides need to be predicted and removed, especially for low modes. The knowledge we gain in this thesis would lead to a better understanding of the low-mode internal tides.

1.2 Thesis objective

Barotropic tidal energy is dissipated mainly by scattering into internal tides in the deep ocean when barotropic tidal currents flowing over rough topography. To understand how internal tides further contribute to diapycnal mixing, it is important to understand the processes related to the generation, propagation and dissipation of internal tides, in particular of low modes that are the most energetic part of internal tides. Since satellite altimeter data provide only the signatures of internal tides in sea level heights with integrations of various modes, it is difficult to derive details of these processes from altimeter data. The high-resolution ocean general circulation models are thus indispensable tools, which can also provide us the three-dimensional baroclinic tidal velocities. It is, however, not clear whether 0.1° horizontal resolution is good enough for this purpose. The first question is thus raised in the following.

- Which resolution is required to properly resolve the low-mode internal tides?

In order to study the processes with regard to the generation, propagation and dissipation of internal tides, we need to find ways to quantify the low-mode internal tides. This brings us to the second question.

- What is the appropriate technique that can be used to quantify the simulated low-mode internal tides?

In the concurrent simulation of the eddying circulation and tides, internal tides exist in a spatially varying wave environment that has realistic stratification and circulation. Thus, these waves interact in a realistic manner with themselves and the medium (eddies, circulation, and so forth), including the potential nonlinear interactions. The relatively complex wave environment and interactions are, however, not involved in linear wave theory. This leads us to the third question.

- What are the properties of the low-mode internal tides that are directly related to the spatially varying wave environments and hence difficult to assess using linear wave theory only? How to interpret these results?

1.3 Outline of the thesis

This thesis comprises two major chapters. They are written in the style of journal publications and thus can be read independently. Chapter 2 [1] has been published and Chapter 3 [2] is in preparation for submission.

---

[1] Li, Z., J.-S. von Storch, and M. Müller, 2015: The M_2 internal tide simulated by a 1/10° OGCM. *J. Phys. Oceanogr.*, **45**, 3119-3135.

[2] Li, Z., J.-S. von Storch, and M. Müller, 2016: The K_1 internal tide simulated by a 1/10° OGCM. *in Prep.*

In **Chapter 2** we introduce the methods how to derive baroclinic tidal velocities from the model output and how we perform the two-dimensional wavenumber spectral analysis in space. Then we present the results on the spatial distributions of the wavelengths of the M_2 internal tide for the first two modes, and compare them with those by solving the Sturm-Liouville eigenvalue problem to investigate which kind of waves are simulated in the STORMTIDE model. The importance of the details of the vertical variations of stratification in determining the wavelengths is also studied by comparing results of the standard and the WKB-simplified Sturm-Liouville eigenvalue problems. Further, the relative roles of the Coriolis frequency f and the buoyancy frequency N in determining the wavelength distributions are diagnosed.

In **Chapter 3** we employ the same methods as used in Chapter 2, which provide us the spatial distributions of the wavelengths for the low-mode K_1 internal tide. These wavelengths are further compared with those of linear wave theory, and the relative roles of f and N are diagnosed, as done in Chapter 2. Furthermore, due to the low latitude of the K_1 critical latitude, it is important to study waves both equatorward and poleward of the critical latitude. Hence, the vertical sections of the K_1 kinetic energy are presented to investigate the role of the critical latitude, and the vertical distributions of the kinetic energy in various water depths are also analyzed in order to understand how the trapping process is simulated in supercritical latitudes in the STORMTIDE model.

This thesis is closed with a summary of our main findings and the outlook in **Chapter 4**.

Chapter 2

The M_2 internal tide simulated by a 1/10° OGCM

Using a concurrent simulation of the ocean general circulation and tides with the 1/10° Max Planck Institute Ocean Model (MPI-OM), known as the STORMTIDE model, this study provides a near-global quantification of the low-mode M_2 internal tides. The quantification is based on wavelengths and their near-global distributions obtained by applying spectral analysis to STORMTIDE velocities and on comparisons of the distributions with those derived by solving the Sturm-Liouville eigenvalue problem.

The simulated wavelengths, with respect to both their magnitudes and their geographical distributions, compare well with those obtained by solving the eigenvalue problem, suggesting that the STORMTIDE internal waves are, to a first approximation, linear internal waves satisfying local dispersion relations. The simulated wavelengths of modes 1 and 2 range within 100-160 km and 45-80 km, respectively. Their distributions reveal, to different degrees for both modes, a zonal asymmetry and a tendency of poleward increase with stratification N and the Coriolis parameter f being responsible for these two features, respectively. Distributions of mode 1 wavelengths are found to be determined by both N and f, but those of mode 2 are mainly controlled by variations in N. Larger differences between the STORMTIDE wavelengths and those of the eigenvalue problem occur, particularly for mode 2, primarily in high-latitude oceans and the Kuroshio and Gulf Stream and their extensions.

2.1 Introduction

Internal tides are internal waves at tidal frequencies that are generated by barotropic tides flowing over rough topographic features in the stratified ocean. Although some uncertainty still exists in the exact amount of the power available for the mixing in the ocean's interior from internal tides, theoretical and numerical models give estimates for the deep ocean in the range of 0.5-0.8 TW for the M_2 internal tide and of 0.9-1.4 TW when considering the largest tidal constituents (Egbert and Ray 2000; Simmons et al. 2004a; Müller 2013; Green and Nycander 2013). The state-of-the-art parameterization of mixing as a result of internal tides (e.g., St. Laurent et al. 2002; Simmons et al. 2004b; Saenko and Merryfield 2005; Montenegro et al. 2007; Exarchou et al. 2012) considers only 30% of this power, the part related to high-mode internal tides that dissipate locally at the generation sites, whereby leaving the remaining 70%, the part related to low-mode internal tides, unspecified. The dissipation of the low-mode internal tides can provide a substantial amount of mixing energy, in which not only does the energy input matter, but also where the dissipations occur in the vertical (Melet et al. 2013), and is important for maintaining the meridional overturning circulation (Munk and Wunsch 1998). So far, our knowledge about the fate of these waves is still limited. Particularly limited is our knowledge about their spatial distributions and to what extent they are affected by the realistic stratification and eddying ocean circulation. This limitation is partly caused by the sparse direct observations in the ocean's interior (e.g., Polzin and Lvov 2011). Satellite altimeters are now frequently used to study internal tides on the global scale, but they provide only integrated wave properties in which modes are superposed (Ray and Mitchum 1997). To advance our understanding, concurrent simulation of the ocean circulation and tides is crucial for studying these low-mode internal tides.

Until recently, tidal and non-tidal motions in the global ocean have been studied separately. Predicting ocean tides is largely based on two-dimensional shallow water equations forced by the tidal forcing only, while simulating the ocean circulation is based on three-dimensional primitive equations forced by momentum and buoyancy fluxes at the sea surface without including the tidal forcing. The first attempts to jointly simulate tides and circulations were made with coarse-resolution ocean-only or climate models (Thomas et al. 2001; Schiller and Fiedler 2007; Müller et al. 2010). Hence, these studies emphasized the effects of barotropic tides on the ocean circulation without resolving mesoscale eddies and internal tides. With increasing computer power, eddy-permitting and eddy-resolving simulations have advanced (Masumoto et al. 2004; Maltrud and McClean 2005; von Storch et al. 2012). The HYCOM group (Arbic et al. 2010, 2012) was the first to report on global concurrent simulations of the eddying general circulation and tides. Soon after another concurrent simulation was carried out using the 1/10° Max Planck Institute Ocean Model (MPI-OM), known as the STORMTIDE model (Müller et al. 2012). In both the HYCOM and STORMTIDE models, barotropic tides are reasonably well simulated (Arbic et al. 2010; Shriver et al. 2012; Müller et al. 2012, 2014). The simulated internal tides' signatures in the sea surface height compare well with those obtained from the altimetry data (Arbic et al. 2010, 2012; Müller et al. 2012), suggesting that both the HYCOM and STORMTIDE models have skill in simulating the low-mode internal tides.

In the present study, we aim to gain more understanding of the M_2 internal tide simulated by the 1/10° STORMTIDE model using the signatures of the low-mode internal tides in baroclinic velocities. The wavelengths are used as a diagnostic tool to quantify the waves and to answer the following questions:

1. Which modes of the M_2 internal tide are simulated in the STORMTIDE model and how consistent are they with the dispersion relation of linear internal waves? What are the properties of the simulated internal tides, for instance, their wavelengths and the respective geographical distributions?
2. What are the relative roles of local stratification N and the Coriolis parameter f in determining these geographical distributions?

3. How important are the details of the vertical variations of stratification in determining the wavelengths of internal tides when taking into account the WKB approximation?

To answer the first question, we use the wavenumber spectra to diagnose the wavelengths from baroclinic velocities simulated by the STORMTIDE simulation and compare the result with wavelengths obtained by solving the Sturm-Liouville eigenvalue problem. To answer the second question, we compare the simulated wavelengths with those obtained by keeping either N or f fixed in the eigenvalue problem. Finally, we derive the wavelengths from WKB-simplified Sturm-Liouville eigenvalue problem and compare them with those of the standard Sturm-Liouville eigenvalue problem to answer the third question concerning the applicability of the WKB approximation. Note that both eigenvalue problems use the same simulated stratification and do not take into account eddying flows.

In section 2.2, the STORMTIDE model is introduced, including a further evaluation of the simulated M_2 internal tide using sea surface height. Section 2.3 describes methods used to diagnose the wavelengths of the M_2 internal tide, including a discussion of the significances and limits of these methods. Results are discussed in section 2.4-2.7: The kinetic energy of the internal tides simulated by the STORMTIDE model is briefly discussed in section 2.4. In section 2.5, we describe the characteristics of the two-dimensional wavenumber spectra and the geographical distributions of the wavelengths deduced from these spectra and compare the result with those obtained by solving the Sturm-Liouville eigenvalue problem. The relative roles of stratification and the Coriolis parameter are examined in section 2.6. Section 2.7 discusses the applicability of the WKB approximation, and section 2.8 presents the concluding remarks.

2.2 The STORMTIDE model

The STORMTIDE model (Müller et al. 2012) is based on the high-resolution MPI-OM formulated on a tripolar grid and concurrently resolves the ocean circulation and tides.

It was developed in the framework of the German consortium project STORM, with an aim towards a coupled high-resolution climate model simulation (von Storch et al. 2012), in which a multidecadal simulation with the NCEP atmospheric forcing has been obtained. Our branch with tides implemented is hence named the STORMTIDE model.

The tripolar MPI-OM uses basically the same physics as its bipolar predecessor (Marsland et al. 2003; Jungclaus et al. 2006). The horizontal resolution is around 1/10°, about 10 km near the equator and about 5 km and less south of 60°S. In the vertical, it uses the ”*z* coordinate” system; 40 unevenly spaced vertical layers are used with nine concentrating in the first 100 m. The layer thickness varies gradually from 10 m in the upper ocean to 500 m in the deep ocean.

In our study, the STORMTIDE model is forced by the complete lunisolar tidal potential, as calculated from the instantaneous positions of the sun and moon (Müller et al. 2012). This forcing takes implicitly hundreds of tidal constituents into consideration (Thomas et al. 2001). The self-attraction and loading (SAL) effect is parameterized in the same way as in Thomas et al. (2001). The model is forced at the sea surface by daily climatological wind stresses with a 365-day cycle and a SST and SSS restoration toward the monthly climatological values (Steele et al. 2001), and is integrated over 10 years.

The ability of the STORMTIDE model to simulate realistic barotropic and internal tides was evaluated in Müller et al. (2012). Comparing the simulated barotropic tides with 102 pelagic tidal observations, the STORMTIDE model was able to capture 92.8% of the variance of the barotropic-tide-induced sea surface height for the eight dominant constituents (Müller et al. 2012). In addition, in a model intercomparison (Stammer et al. 2014), the model-simulated barotropic tidal currents of the STORMTIDE model were evaluated. No internal wave drag is implemented in our model approach and instead about 1.1 TW of tidal energy is converted from barotropic to internal tides (Müller 2013), consistent with observational estimates (e.g., Egbert and Ray 2000).

In the following, we further extend the evaluation of the sea surface signatures of the M_2 internal tide in Müller et al. (2012) by incorporating an observational product obtained from 19-yr along-track satellite altimetry [TOPEX, Poseiden, Jason-1, and Jason-2 (TPJ)] data (Cherniawsky et al. 2001; Foreman et al. 2009). Both the M_2 along-track tidal signals obtained from the TPJ data and the model-simulated sea surface height are obtained using a high-pass filter, with a cutoff wavelength of about 350 km, for a removal of the long-wave barotropic tidal signals. The signals are binned, where ocean depths are larger than 1000 m, into $1^\circ \times 1^\circ$ boxes and their root-mean-squared (RMS) amplitudes are computed (Fig. 2.1). Note that since we considered the hourly model-simulated output (January 1^{st} to February 1^{st} of the ninth simulation year; for details see section 2.3.1) , no tidal aliasing (e.g., Zhao et al. 2012) is involved in the simulated data processing which occurs only in the altimetry data as a result of their poor temporal resolutions. To evaluate the RMS amplitudes in specific hot spots, we choose regions as in Shriver et al. (2012) and indicate them in Fig. 2.1b. The RMS amplitudes of the model and observations are given in Table 2.1, along with the RMS ratios of the observations to model results. A large model underestimation is presented in the Hawaii region. The internal tide beam from the Aleutians is also significantly reduced in the model. In the other regions, the mismatch is less than 20% and reflects a similar quality in simulating the magnitude of internal tides in hot spots regions as in Shriver et al. (2012). Because of the mesoscale contamination (e.g., Shriver et al. 2012) induced by the tidal aliasing in the altimetry data, we can observe large spurious signals in the Gulf Stream, Kuroshio extensions and the Southern ocean in the altimetry data. In general, we conclude that the STORMTIDE model gives us a reasonably good model simulation of internal tides, in regard to what is currently possible in a global model approach.

(a) Satellite altimetry

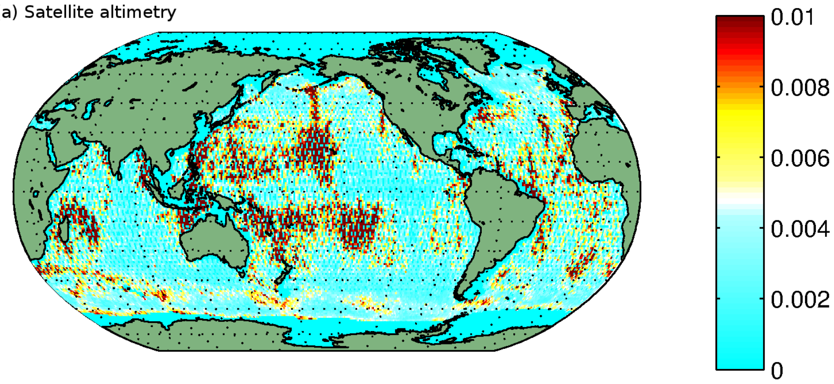
0.01
0.008
0.006
0.004
0.002
0

(b) Model

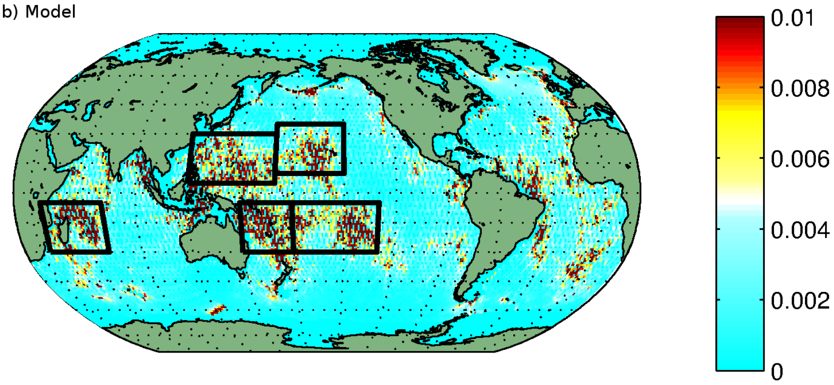
0.01
0.008
0.006
0.004
0.002
0

Figure 2.1: RMS amplitudes (m) of the M_2 internal tide obtained from (a) the 19-yr satellite altimetry data and (b) the 2-yr hourly sea surface height simulated by the STORMTIDE model. The M_2 tidal signals are high-pass filtered and then binned into $1^\circ \times 1^\circ$ boxes. The black boxes mark the regions of hot spots used in Table 2.1.

Table 2.1: The surface signals (cm) of the M_2 internal tide averaged as quantities by RMS over various hot spots regions indicated in Fig. 2.1. TPJ and STORMTIDE refer to the observations and model simulation, respectively. The last column shows the RMS ratios of observations to model results.

Region	TPJ	STORMTIDE	ratio
East of Philippines	0.79	0.74	1.06
Hawaii	0.87	0.60	1.44
Tropical South Pacific	0.97	1.10	0.88
Tropical SW Pacific	0.86	0.72	1.19
Madagascar	0.85	0.91	0.94

2.3 Methods

2.3.1 Details in deriving the baroclinic M_2 tidal velocities

For the quantification of the kinetic energy and also for the wavelength analysis of the STORMTIDE data throughout this paper, we use the three-dimensional horizontal M_2 tidal velocities [see Müller et al. (2012) for a detailed description]. They are publicly available (Müller 2012). Because of the huge amount of three-dimensional hourly data that are used, we limit the data length to be 32 days, which is the minimum requirement for the spectral analysis in order to resolve certain tidal constituents. Using the 32-day model-simulated full zonal and meridional velocities from January 1^{st} to February 1^{st} of the ninth simulation year, we perform the harmonic analysis to derive the amplitudes A_{M_2} and phases ϕ_{M_2} of the full M_2 tidal velocities. Taking the zonal velocities as an example, we describe the full M_2 tidal velocities as

$$u_{M_2}(i,j,k,t) = A_{M_2}(i,j,k)e^{i[2\pi\omega t - \phi_{M_2}(i,j,k)]}, \tag{2.1}$$

in which i, j and k are the grid indices in the zonal, meridional and vertical directions, ω is the M_2 tidal frequency and t is time. The vertical integration of Eq. (2.1) gives the barotropic M$_2$ tidal velocities

$$u_{bt}(i,j,t) = \left[\frac{1}{H} \sum_k A_{M_2}(i,j,k) e^{-i\phi_{M_2}(i,j,k)} \triangle H_k \right] e^{i2\pi\omega t}, \tag{2.2}$$

in which H is the water depth and $\triangle H_k$ is the thickness of the k-th layer. The complex baroclinic M$_2$ velocities are obtained by subtracting the complex barotropic velocities in Eq. (2.2) from the full velocities in Eq. (2.1). Denoting the amplitudes and phases of the resulting baroclinic M$_2$ velocities by $A_{u_{bc}}(i,j,k)$ and $\phi_{u_{bc}}(i,j,k)$, the baroclinic M$_2$ tidal velocities are given by

$$\begin{aligned} u_{bc}(i,j,k,t) &= u_{M_2}(i,j,k,t) - u_{bt}(i,j,t) \\ &= A_{u_{bc}}(i,j,k) e^{i[2\pi\omega t - \phi_{u_{bc}}(i,j,k)]}. \end{aligned} \tag{2.3}$$

The amplitudes ($A_{u_{bc}}$ and $A_{v_{bc}}$) and phases ($\phi_{u_{bc}}$ and $\phi_{v_{bc}}$) of the zonal and meridional baroclinic M$_2$ tidal velocities are all interpolated onto 0.1° × 0.1° regular longitude-latitude grids. The interpolated amplitudes $A_{u_{bc}}$ and $A_{v_{bc}}$ are used to estimate the kinetic energy of the M$_2$ internal tide in section 2.4, since this energy is related to wave motions satisfying the dispersion relation of internal tides, as will be shown in section 2.5.

2.3.2 Two-dimensional wavenumber spectral analysis

A two-dimensional wavenumber spectral analysis is used to diagnose the wavelengths of the M$_2$ internal tide. The analysis is based on the standard two-dimensional complex discrete Fourier transform. We reconstruct the complex velocities with the in-phase and quadrature baroclinic velocities being the real and imaginary components, respectively. The in-phase and quadrature velocities are a quarter of a period apart, and are expressed, taking u_{bc} as an example, as $A_{u_{bc}} cos\phi_{u_{bc}}$ and $A_{u_{bc}} sin\phi_{u_{bc}}$. The spectral analysis is applied to these complex velocities in boxes of the size $15°/cos\varphi$ (in longitude) $\times 15°$ (in latitude) with φ being the latitude. For each $15°/cos\varphi \times 15°$ box, they are further converted to velocities on an equidistant grid (with an approximate 11 km resolution). Prior to the spectral analysis, a Tukey window is used to reduce spectral leakage, which tapers the signal at the endpoints, thereby emphasizing the data in the center of a box. For a given level, u_{bc} and v_{bc} inside a $15°/cos\varphi \times 15°$ box are decomposed into two-dimensional plane waves with Fourier coefficients $U(k,l)$ and $V(k,l)$ as wave amplitudes, where k and l are the zonal and meridional wavenumbers, respectively. In order to obtain a near-global map, overlapping boxes are analysed each shifted by 5°. Wavenumber spectra $S_{u_{bc}}(k,l)$ and $S_{v_{bc}}(k,l)$ are then given by

$$S_{u_{bc}}(k,l) = |U(k,l)|^2 \text{ and} \tag{2.4a}$$

$$S_{v_{bc}}(k,l) = |V(k,l)|^2. \tag{2.4b}$$

The average of $S_{u_{bc}}(k,l)$ and $S_{v_{bc}}(k,l)$ results in the spectrum of the kinetic energy, denoted by $S_{KE}(k,l)$, in which velocities in both horizontal directions are taken into account for a robust result. The corresponding wavenumber spectra in the $(k$,$l)$ wavenumber plane are then converted into $S_{KE}(K)$, which are functions of the horizontal wavenumber $K = \sqrt{k^2+l^2}$. By moving the box horizontally, wavenumber spectra at different locations can be obtained. The horizontal wavelength is identified from the wavenumber where $S_{KE}(K)$ has a local maximum. Obviously, this diagnostic will work well when there is a distinct spectral peak, but it will produce an ambiguous result when the spectrum is flat. Note that we make no interpolations for land points inside a box. Instead, $U(k,l)$ and $V(k,l)$ are calculated from available water points in a box. Only boxes in which land points are less than 15% are considered.

Generally, stratification and the bathymetry (and consequently the water depth) vary from grid point to grid point so that different wavelengths are expected from the dispersion relation. The wavelength derived from the spectral analysis cannot capture such variations and has to be considered as an averaged wavelength within the considered box. Here, ”average” does not refer to an ”arithmetic mean”, but rather the fact that the spectral analysis provides only one estimate of the wavelength corresponding to each local maximum from $S_{KE}(K)$ in a given box. This has to be kept in mind when comparing the wavelengths derived from wavenumber spectra of the STORMTIDE products with those obtained from the linear internal wave theory using a prescribed stratification and water depth. Wavelengths derived from the STORMTIDE model simulation will be denoted by L_{ST}.

In the present paper the goal is to estimate the wavelengths of internal tides simulated by an ocean circulation model and compare them with the wavelengths derived from the linear wave theory. Thus, a (vertical) modal decomposition of the baroclinic tidal velocities, as usually performed for point observation, is not adequate, since it would implicitly constrain the results by assumptions given by the mode computations. Thus, the horizontal spectral analysis seems to be beneficial to derive the quantity of simulated internal tide wavelengths and further, with the windowing of the velocities prior to the spectral analysis and the shifting of the boxes by 5°, a near-global map with a resolution of 5° can be obtained. To divide into mode 1 and mode 2 internal tides, we will analyse the three-dimensional fields of baroclinic tidal velocities on different model levels, as further detailed in section 2.5.1.

It is noted that the size of the box is a compromise between the demand to obtain a more reliable estimate of the spectral peaks on the one hand and a more detailed map of the geographical variations of the wave environment on the other hand. The former requires a larger box size, but the latter a smaller box size. We found a $15°/cos\varphi \times 15°$ box size to be a reasonable compromise.

2.3.3 The Sturm-Liouville eigenvalue problem

To confirm that the dominant length scales identified using wavenumber spectra represent the wavelengths of the low-mode M_2 internal tides, the local dispersion relation of internal waves is derived by solving the Sturm-Liouville eigenvalue problem (e.g., Olbers et al. 2012) for stratification profiles that are simulated by the STORMTIDE model. We assume a flat bottom inside a $15°/cos\varphi \times 15°$ box and no background current in this eigenvalue problem. The water depth inside a box corresponds to the box-averaged depth. Topographic features and background currents are only considered in the STORMTIDE simulation. The Sturm-Liouville eigenvalue problem is defined by

$$\frac{1}{N^2(z)}\frac{d^2}{dz^2}w_m(z) = -\nu_m w_m(z),\ m = 1, 2, ... \tag{2.5}$$

together with boundary conditions of the flat bottom and rigid lid, in which z refers to the vertical axis, $N(z)$ is the buoyancy frequency, $w(z)$ is the vertical structure of the waves. The vertical mode number m refers to the mth eigenvector $w_m(z)$ with the corresponding eigenvalue ν_m. The eigenvalue ν_m defines the dispersion relation

$$\nu_m = \frac{K_m^2}{\omega^2 - f^2}, \tag{2.6}$$

in which ω and f are the M_2 tidal frequency and the Coriolis parameter, respectively. Given a box-averaged stratification profile, and $w_m(z)$ and ν_m are obtained by numerically solving the Sturm-Liouville eigenvalue problem. The horizontal wavelength, denoted by $L_{SL,m}$ and defined as

$$L_{SL,m} = \frac{1}{K_m} = \frac{1}{\sqrt{\nu_m(\omega^2 - f^2)}}, \tag{2.7}$$

corresponds to the mth vertical mode. Thus, $L_{SL,m}$ is determined solely by the local stratification profile and the Coriolis parameter.

To be consistent with the wavenumber spectral analysis, we solve the Sturm-Liouville eigenvalue problem for the same $15°/cos\varphi \times 15°$ boxes using the box-averaged stratification and water depth. The box-averaged monthly mean temperature and salinity are used to calculate the corresponding box-averaged N. The resulting N is always well-defined (i.e., real). When $N < 10^{-10}$ s^{-1}, it is interpolated with the neighboring points in solving the eigenvalue problem. Note that the horizontal variations of stratification within each box are neglected, whereas box-averaged vertical variations are taken into account. The stratification available on the model levels is then interpolated onto a vertical grid with a resolution of 10 m that is used to numerically solve the eigenvalue problem.

Since the Sturm-Liouville eigenvalue problem is derived from the linear internal wave theory, the question of whether the STORMTIDE model is capable of simulating internal tides is answered by a comparison of the wavelengths obtained from the Sturm-Liouville eigenvalue problem with those obtained by applying spectral analysis to the STORMTIDE simulation.

2.3.4 The WKB-simplified eigenvalue problem

For each stratification profile, one needs to solve the respective Sturm-Liouville eigenvalue problem to obtain $L_{SL,m}$. The WKB approximation assumes that the rate of the vertical change in stratification is slower than the vertical variation of internal tides and leads to a further simplification of the Sturm-Liouville eigenvalue problem. This WKB-simplified eigenvalue problem (e.g., Chelton et al. 1998; Olbers et al. 2012) provides the following relation between eigenvalues and stratification

$$\nu_{WKB,m} = \frac{m^2\pi^2}{\widehat{N}^2}, \tag{2.8}$$

where $\widehat{N} = \int_{-H}^{0} N(z')dz'$ is the vertical integral of stratification. Substituting Eq. (2.8) into (2.7), the wavelength of the WKB-simplified eigenvalue problem, denoted by $L_{WKB,m}$, is expressed as

$$L_{WKB,m} = \frac{\widehat{N}}{m\pi\sqrt{\omega^2 - f^2}}, \tag{2.9}$$

where $\widehat{N}$ is derived from the same box-averaged stratification and water depth as used for $L_{SL,m}$.

The wavelengths $L_{WKB,m}$ now can be obtained without solving the Sturm-Liouville eigenvalue problem. By comparing $L_{WKB,m}$ with $L_{SL,m}$, we can assess the importance of details of the vertical structures of $N(z)$ that are not described by $\widehat{N}$ in determining $L_{WKB,m}$, whereby addressing the third question raised in the introduction (section 2.1).

2.4 Kinetic energy of the M_2 internal tide

Since it is difficult to diagnose the kinetic energy related to internal tides from the observations, we present here a quantification of this energy based on the STORMTIDE simulation. Fig. 2.2a and 2.2b show the horizontal distributions of the kinetic energy of the M_2 internal tide at 100 m and 1085 m, respectively. As will be discussed in section 2.5.1, 100 m and 1085 m are depths, at which two different modes dominate, respectively. The kinetic energy at 100 m is much stronger than that at 1085 m. The overall structures resemble those of the satellite-observed internal tide surface signatures, and are characterized by hot spots at both depths, for instance, near Madagascar, Hawaii, east of the Philippines, and the tropical South and Southwest Pacific. The maxima of the kinetic energy correspond to a current speed of about 5-6.5 cm s^{-1} at 100 m and 1.5-2 cm s^{-1} at 1085 m for the M_2 internal tide. For comparison, the typical speed of maximum transient eddying currents is about 30 cm s^{-1} at 100 m (von Storch et al. 2012). The globally integrated kinetic energy of the M_2 internal tide is about 0.08 EJ (1 EJ = 10^{18} J). This is about 20% of the internal wave energy (von Storch et al. 2012) that results presumably from wind-induced near-inertial waves.

Fig. 2.2c shows the vertical integral of the kinetic energy with a spatial pattern comparable to those at 100 m and 1085 m. The amplitude and the structure compare also well with the M_2 internal tide energy obtained by solving two coupled equations describing integrated versions of the radiative transfer equations for the M_2 internal tide and a wave continuum (Eden and Olbers 2014, their Fig. 5b). One of the main difference is the beam-like structures which are absent in the figure by Eden and Olbers (2014). This difference results from the fact that Eden and Olbers (2014) assumed for simplicity a uniform distribution of the wave propagation angle in the forcing term. Consequently, the equations considered do not distinguish waves with different wavevector angles. If the wave sources are not homogeneously distributed, waves propagating from the individual generation sites, characterized by beam-like structures, would stand out more clearly, as in case of Fig. 2.2c.

(a) Kinetic energy, 100 m

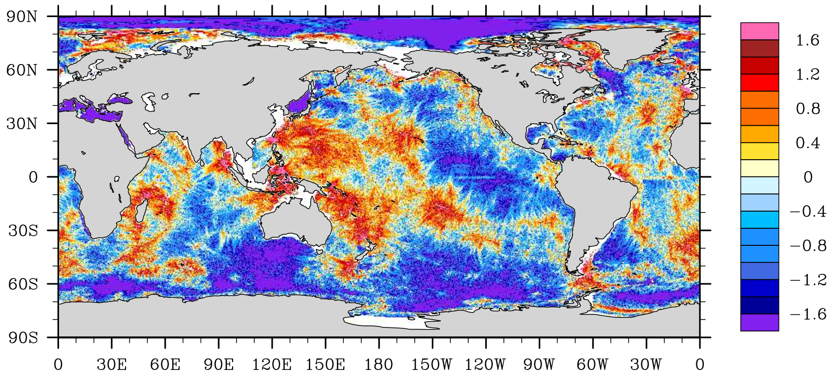
90N
60N
30N
0
30S
60S
90S
0
30E
60E
90E
120E
150E
180
150W
120W
90W
60W
30W
0
1.6
1.2
0.8
0.4
0
−0.4
−0.8
−1.2
−1.6

(b) Kinetic energy, 1085 m

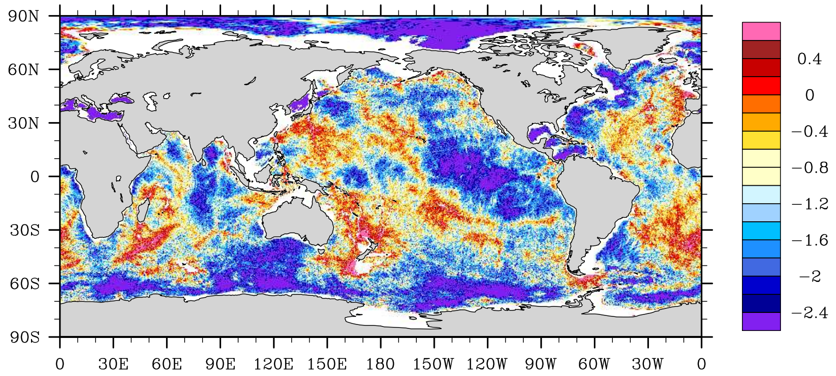
90N
60N
30N
0
30S
60S
90S
0
30E
60E
90E
120E
150E
180
150W
120W
90W
60W
30W
0
0.4
0
−0.4
−0.8
−1.2
−1.6
−2
−2.4

(c) Vertical integral of the kinetic energy

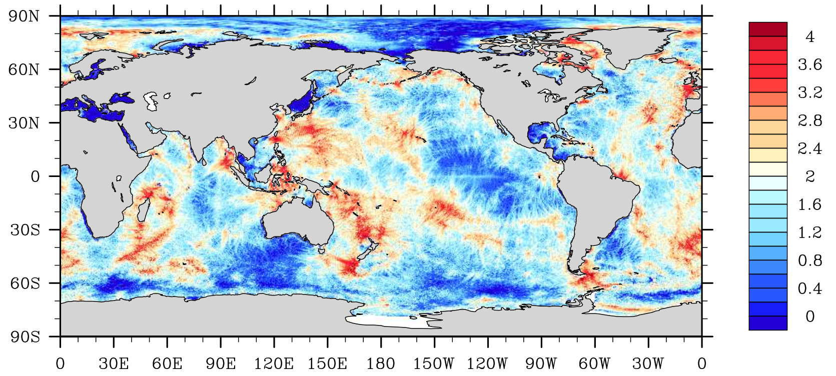
90N
60N
30N
0
30S
60S
90S
0
30E
60E
90E
120E
150E
180
150W
120W
90W
60W
30W
0
4
3.6
3.2
2.8
2.4
2
1.6
1.2
0.8
0.4
0

Figure 2.2: Kinetic energy (cm^2 s^{-2}) of the M_2 internal tide in logarithmic scales at (a) 100 m and (b) 1085 m. (c) The vertical integral of the kinetic energy (J m^{-2}) in logarithmic scales, which is prepared in the same scales as used in Eden and Olbers (2014, their Fig. 5b). The kinetic energy at single depth is derived using $(A^2_{u_{bc}} + A^2_{v_{bc}})/2$, with $A_{u_{bc}}$ and $A_{v_{bc}}$ being amplitudes of the M_2 baroclinic zonal and meridional velocities, respectively. The vertical integral is then derived by $\int_{-H}^{0} \rho_w (A^2_{u_{bc}} + A^2_{v_{bc}})/2dz$ with ρ_w being the density of seawater.

2.5 Wavelengths of the model-simulated M$_2$ internal tide

2.5.1 Characteristics of wavenumber spectra

Before considering the wavelengths, we first study characteristics of the two-dimensional wavenumber spectra. Fig. 2.3 shows spectra $S_{KE}(k,l)$ in the left column, with both positive and negative wavenumbers (Fig. 2.3a and 2.3c), at both 100 m and 1085 m in the $15°/cos\varphi \times 15°$ box centered at (170°W, 22.55°N). At 100 m (Fig. 2.3a), a distinct spectral peak of $S_{KE}(k,l)$ is shown in the form of a near-circle band on the (k,l) plane. This most energetic band is located within the range of K of about 0.005-0.01 km^{-1}, corresponding to a horizontal wavelength of 100-200 km. A less pronounced band is located at relatively larger wavenumbers, with K being around 0.015 km^{-1}, corresponding to a wavelength of about 65 km. In the ocean's interior at 1085 m, two spectral peaks are also located at the same wavenumber bands. In contrast to the spectrum at 100 m, the high-wavenumber peak, with a broader bandwidth, is stronger than the low-wavenumber peak. Some spectral energy much weaker than the two spectral peaks is also found at still higher wavenumbers at both depths.

The two spectral peaks remain well defined when converting $S_{KE}(k,l)$ into $S_{KE}(K)$ in Fig. 2.3b and 2.3d. The blue dots show $S_{KE}(K)$ obtained from each wavenumber vector (k,l). The red lines represent the bin averages of $S_{KE}(K)$ that are averaged over all values of $S_{KE}(K)$ with K inside the respective intervals. For each wavenumber, the variability indicated by the blue dots results from variations of $S_{KE}(k,l)$ along a circle centered at the origin of the (k,l) plane. These variations indicate properties of wave propagation. For waves generated at a few selected source sites, maxima of the respective two-dimensional wavenumber spectra will not have the same strength in all directions. For instance, in Fig. 2.3a, the low-wavenumber peak has the largest values in the southwest and northeast direction. Thus, waves associated with the low-wavenumber peak in the box considered in Fig. 2.3 propagate preferably along a line orientated in the southwest-northeast direction.

We now consider the vertical dependence of $S_{KE}(K)$ in terms of the example shown

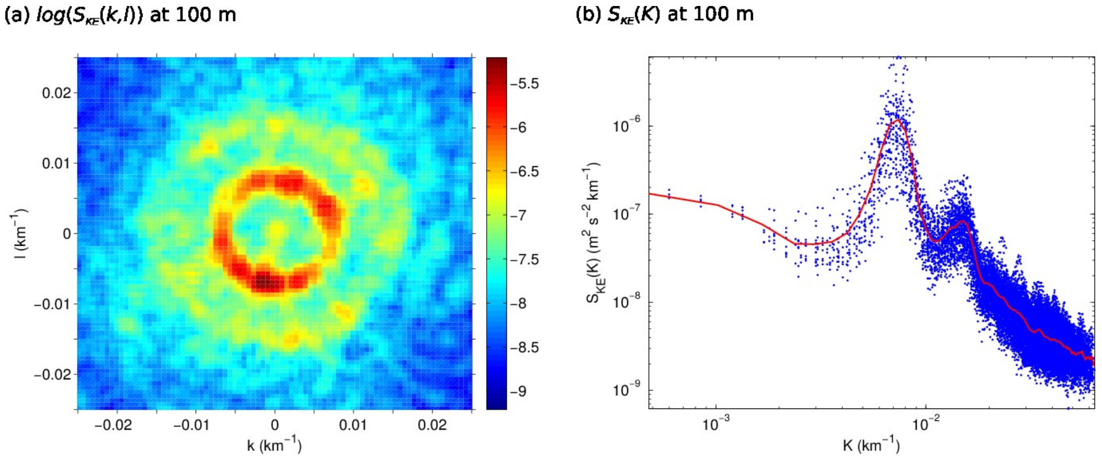

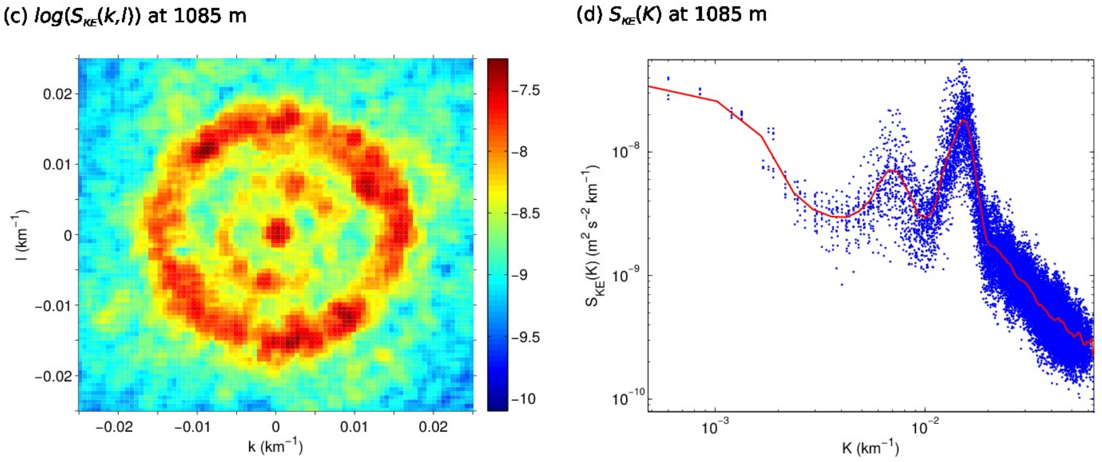

Figure 2.3: Wavenumber spectra $S_{KE}(k, l)$ of the kinetic energy of the M_2 internal tide at (a) 100 m and (c) 1085 m in logarithmic scales in the $15°/cos\varphi \times 15°$ box centered at (170°W, 22.55°N). The resolved range of the zonal and meridional wavenumbers is within -0.045-0.044 km^{-1}. To enhance the readability, we only show the range of -0.025-0.025 km^{-1} that involves the most energetic motions and leave out wavenumber regions with very weak energy. In the right column, wavenumber spectra $S_{KE}(K)$ of the M_2 internal tide are shown at (b) 100 m and (d) 1085 m, converted from $S_{KE}(k, l)$ using $K = \sqrt{k^2 + l^2}$ in the same box. The scattered blue dots are converted directly from each value of $S_{KE}(k, l)$. The red lines represent the bin averages of $S_{KE}(K)$, in which $S_{KE}(K_i)$ at the i^{th} interval is obtained by averaging all values of $S_{KE}(K)$ with K inside the interval (K_i,K_i+ $\triangle$). We consider a total of 100 consecutive intervals. Term $\triangle$ is obtained by dividing the total resolved wavenumber range by 100.

in Fig. 2.4. Overall, the spectral energy decreases with increasing depth. The low-wavenumber peak is strongest in the upper ocean, followed by a reduction until the energy drops to a minimum at 1220 m (red dotted line). The spectral peak reemerges further downward. The high-wavenumber spectral energy undergoes more complicated variations. The spectral peak is detectable in the top 100 m and diminishes downwards, disappears to different degrees in the depth range 122-485 m. It becomes evident again farther below and clearly stands out in the depth range 560-1700 m. Below 1700 m, it is strongly weakened.

To understand the depth-dependence of the low- and high-wavenumber peaks of $S_{KE}(K)$, we introduce the vertical modal structures of the kinetic energy of modes 1 and 2 (the right panel of Fig. 2.4b), respectively. These vertical structures are derived by solving the Sturm-Liouville eigenvalue problem [see Eq. (2.5), for m =1 and 2] using the box-averaged stratification profile shown in the left panel of Fig. 2.4b. They show a zero crossing at around 1220 m for mode 1 and an interior maximum at about 750 m between two zero crossings at about 350 m and 2200 m for mode 2. The variations with depth of both low- and high-wavenumber spectral peaks shown in Fig. 2.4a correspond, in general, to the vertical structures of the first two modes of the Sturm-Liouville eigenvalue problem. In particular, we observe a loss of the low-wavenumber peak and find only the high-wavenumber peak at 1220 m. This is consistent with the fact that the amplitude of mode 1 undergoes its zero crossing at this depth, while the amplitude of mode 2 remains strong. Hence, the low- and high-wavenumber peaks are proved to be actually mode 1 and 2, respectively.

As for the box considered in Fig. 2.4a, both mode 1 and mode 2 have the same wavenumber throughout the water column in all considered boxes. This result reflects the fact that the horizontal wavelength of a mode is independent of depth, indicating that certain layers with energetic internal tides can be selected to efficiently identify the wavenumbers of each mode. For this purpose, we have examined the zero-crossing depths of modes 1 and 2. The mode 1 zero crossings, in regions with less than 15% land points, - that is, in the open ocean - are located at depths deeper than 700 m.

(a) $S_{KE}(K)$

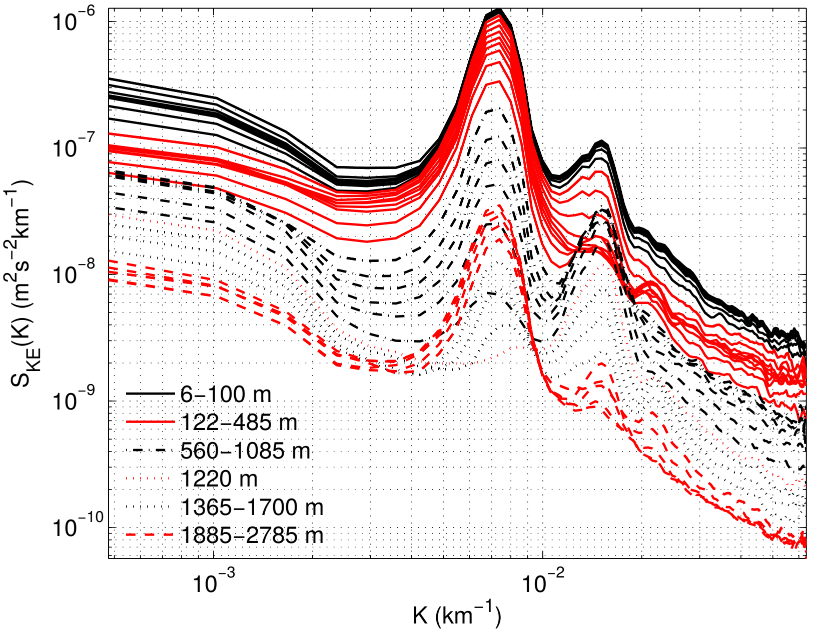

(b) $N(z)$ and modal structures

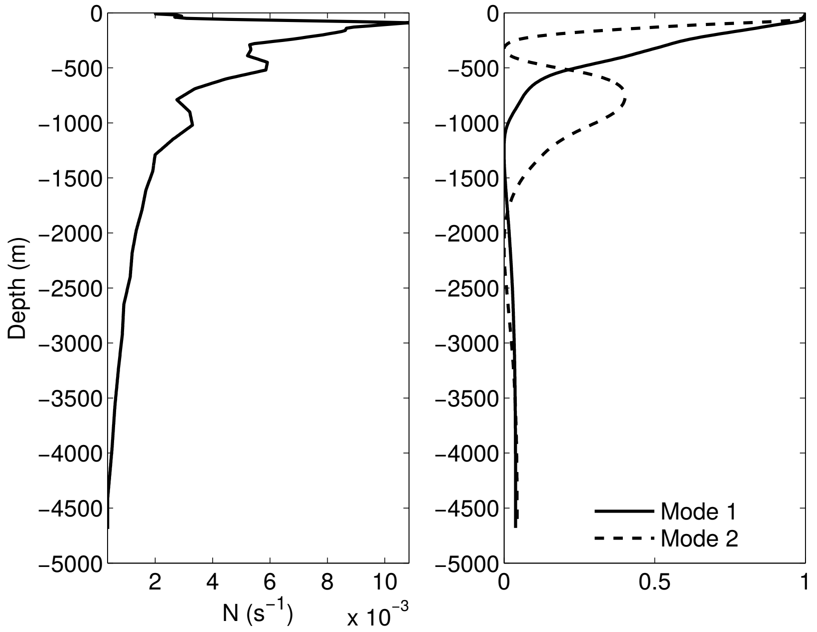

Figure 2.4: (a) Bin-averaged spectra $S_{KE}(K)$ of the horizontal kinetic energy of the M$_2$ internal tide derived for the $15°/cos\varphi \times 15°$ box centered at (170°W, 22.55°N). (b) shown are (right) the vertical modal structures of mode 1 (solid) and mode 2 (dashed) of the kinetic energy in the considered box, which are proportional to $[dw_m(z)/dz]^2$ with $w_m(z)$ being the eigenfunction of Eq. (2.5). These structures are derived by solving the Sturm-Liouville eigenvalue problem with (left) the box-averaged stratification profile simulated by the STORMTIDE model.

Mode 2 undergoes its first zero crossing at levels shallower than 900 m, whilst its second zero crossing is located at depths deeper than 1400 m, both in the open ocean. Thus performing spectral analysis on velocities at 100 m and around 1000 m, which depart from the depths of zero crossings of modes 1 and 2, respectively, one should be able to identify the wavelengths of modes 1 and 2. In the following, the near-global map of the mode 1 wavelengths $L_{ST,1}$ is hence derived from $S_{KE}(K)$ at 100 m in section 2.5.2. In the deeper ocean (e.g., around 1000 m), mode 2 is energetic, while mode 1 possesses normally only weak energy. Hence, the near-global map of the mode 2 wavelengths $L_{ST,2}$ is derived from $S_{KE}(K)$ at 1085 m.

In the process of performing spectral analysis for the kinetic energy of internal tides in boxes covering the near-global ocean, we realize that the spectral peaks are difficult to detect in regions with strong mesoscale eddies. The normalized spectral width of mode 1 is shown in Fig. 2.5. We can see that larger spectral widths mainly occur in strong current regions, for instance, the Kuroshio and the Gulf Stream as well as their extensions, and the Antarctic Circumpolar Current regions in the southern high latitudes. In these regions, the peaks are broadened. When the peaks get too broad or even turn to flat spectra, an identification of the associated wavenumber will be hardly possible. Thus,we neglect the regions poleward of 52.45°S/52.55°N in the following near-global analysis.

2.5.2 Geographical distribution of wavelengths

The near-global map of $L_{ST,1}$ (Fig. 2.6a) shows that the scales of mode 1 are around 100-160 km in most regions, with the wavelengths shorter than 100 km existing only in the very eastern equatorial region in the Pacific, in the southern Indian Ocean and in the eastern equatorial Atlantic. The wavelengths longer than 170 km emerge mainly in mid- and high latitudes, for instance, east of Japan and and in the southwestern Pacific and south of Australia. This distribution reflects both a general poleward increase in $L_{ST,1}$, and a zonal asymmetry that is more pronounced in the Pacific than in the other two ocean basins.

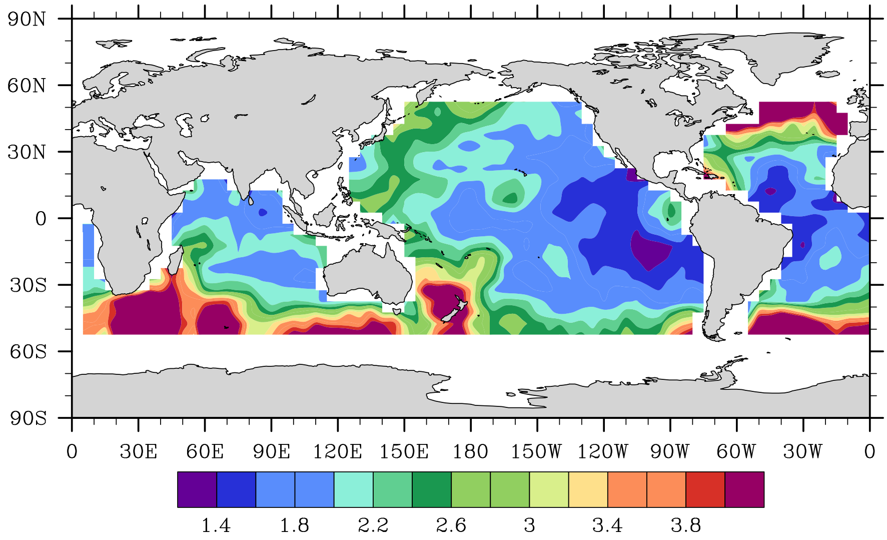

Figure 2.5: Normalized spectral width (×10) derived from the mode 1 wavenumber spectra. The width is defined by the wavenumber interval between half of the peak energy, and is then normalized by the wavenumber related to the spectral peak. Nine-point smoothing has been performed after deriving the raw near-global map.

The mode 2 wavelengths (Fig. 2.7a) are around 45-80 km. The $L_{ST,2}$ in the Atlantic are generally in the range of 45-65 km and have the lowest values among the three ocean basins. The length scales of mode 2 in the Indian Ocean are around 50-80 km, with the longest wavelengths appearing in the northeastern part. Waves in the Pacific show a clear zonal asymmetry with wavelengths longer than 75 km mainly in the northwestern Pacific and in the western tropical Pacific, and with wavelengths shorter than 60 km in the southeastern South Pacific. The mode 2 wavelengths reveal a strong zonal asymmetry that outweighs the meridional variation and is much more pronounced than the zonal asymmetry of $L_{ST,1}$.

2.5.3 Comparison with the distribution obtained by solving the eigenvalue problem

The geographical distribution of $L_{ST,1}$ is comparable with that of $L_{SL,1}$. Figure 2.8a shows that the relative differences are primarily under 10% of the local wavelengths in

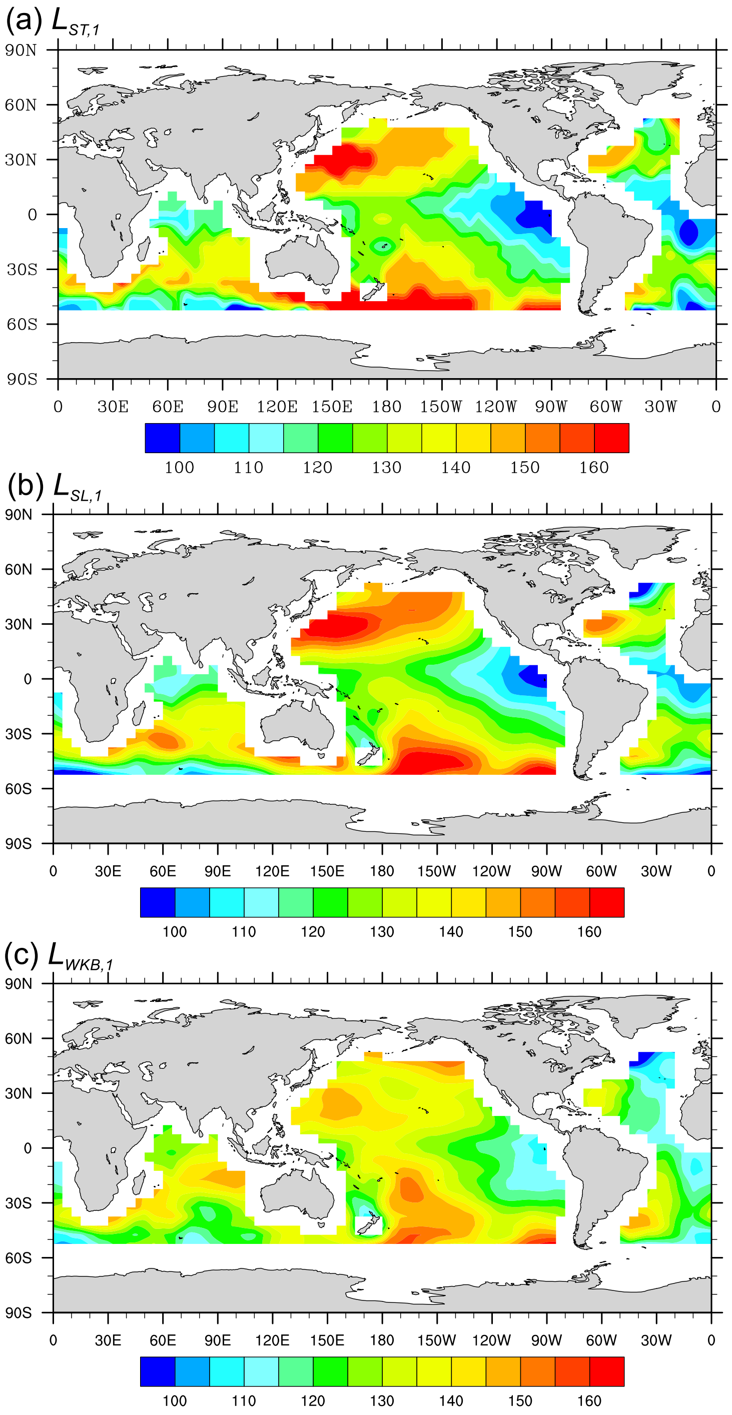
(a) $L_{ST,1}$
(b) $L_{SL,1}$
(c) $L_{WKB,1}$
90N
60N
30N
0
30S
60S
90S
0
30E
60E
90E
120E
150E
180
150W
120W
90W
60W
30W
0
100
110
120
130
140
150
160

Figure 2.6: Distributions of the mode 1 wavelengths (km) for the M_2 internal tide as derived (a) by applying two-dimensional wavenumber spectral analysis to the M_2 baroclinic velocities at 100 m simulated by the STORMTIDE model for overlapping $15°/cos\varphi \times 15°$ boxes, (b) by numerically solving the Sturm-Liouville eigenvalue problem, and (c) by analytically solving the WKB-simplified eigenvalue problem. Both eigenvalue problems use the same stratification profiles averaged over the same boxes as used in the spectral analysis.

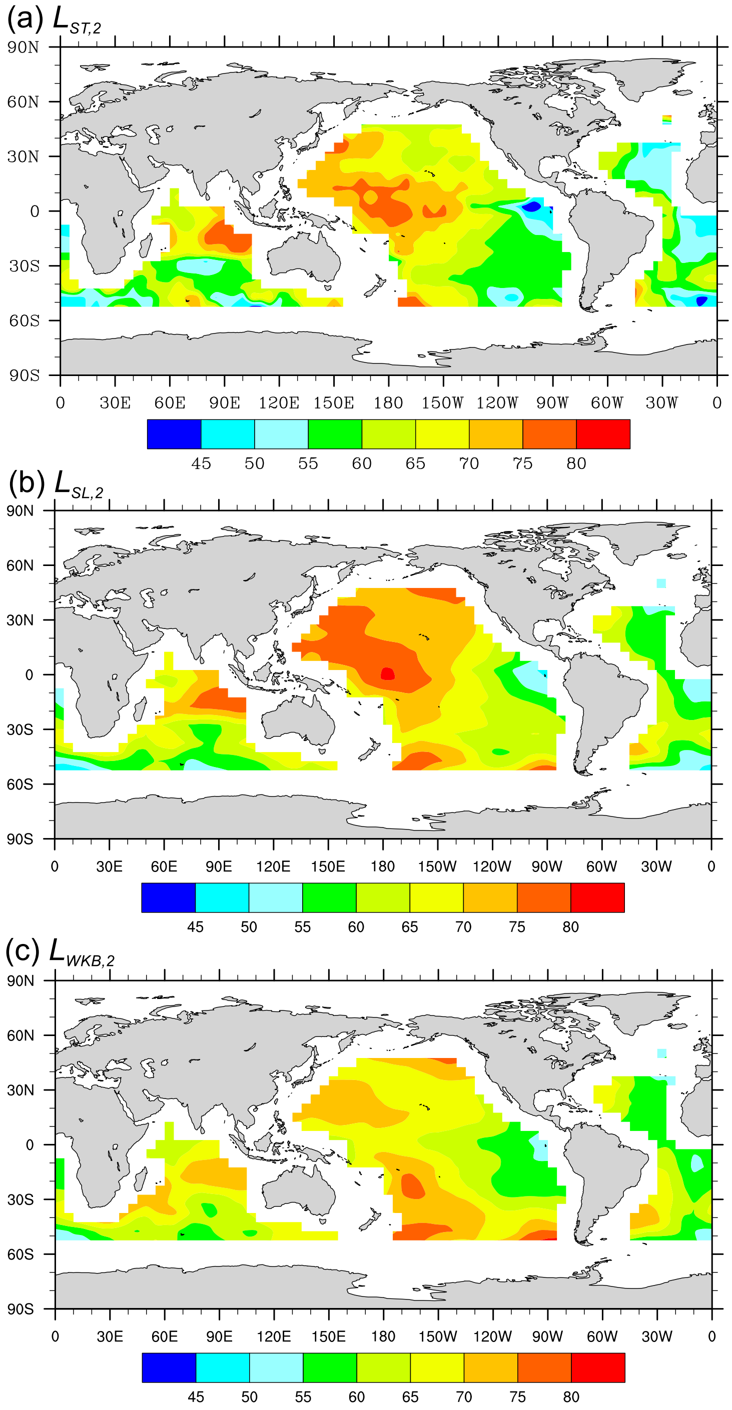
(a) $L_{ST,2}$
(b) $L_{SL,2}$
(c) $L_{WKB,2}$
90N
60N
30N
0
30S
60S
90S
0
30E
60E
90E
120E
150E
180
150W
120W
90W
60W
30W
0
45
50
55
60
65
70
75
80

Figure 2.7: Distributions of the mode 2 wavelengths (km) for the M$_2$ internal tide. The same methods are used as described in Fig. 2.6, except that the spectral analysis is performed for the STORMTIDE M$_2$ baroclinic velocities at 1085 m for deriving $L_{ST,2}$.

around 90.6% of the global ocean considered, and under 5% of the local wavelengths in two-thirds of the global ocean. The small differences lead to a good agreement between the zonal-mean $L_{ST,1}$ and $L_{SL,1}$ in Fig. 2.9a. In high latitudes, mainly in the Indian Ocean and Atlantic, larger discrepancies also arise, but with only 3% of the global ocean considered having a relative difference larger than 15%. The result indicates that in most of the global ocean, particularly in the Pacific, the mode 1 M$_2$ internal tide simulated by the STORMTIDE model is well explained by linear waves that satisfy the local dispersion relation, diagnosed locally, with other effects accounting for less than 10% in terms of relative differences.

Figure 2.8b shows mainly negative relative discrepancies of mode 2, indicating that the simulated mode 2 wavelengths are in general shorter than those predicted by the Sturm-Liouville eigenvalue problem. The relative differences are under 10% in about 73% of the global ocean considered. Larger discrepancies occur mainly in high latitudes. With respect to zonal means, the meridional profile of $L_{ST,2}$ is comparable with that of $L_{SL,2}$ (Fig. 2.9b). Overall, mode 2 shows a larger relative discrepancies than mode 1, which makes sense since shorter waves are more easily affected by the varying oceanic medium, introducing stronger nonlinear effect.

2.6 Relative roles of N and f in determining the wavelengths

The mode 1 wavelengths simulated by the STORMTIDE model (Fig. 2.6a) reveal a zonal asymmetry and a general poleward increase. The same features are observed in results of the standard (Fig. 2.6b) and the WKB-simplified (Fig. 2.6c) Sturm-Liouville eigenvalue problems whose solutions solely depend on the local stratification N and on the Coriolis parameter f. We now explore the relative roles of N and f in determining the distribution of the wavelengths. Along a latitude circle, since f is constant, the zonal asymmetry must result from the effect of N.

To further separate the roles of N and f in determining the wavelengths, we design another two near-global maps of the mode-1 wavelengths using the linear theory. One

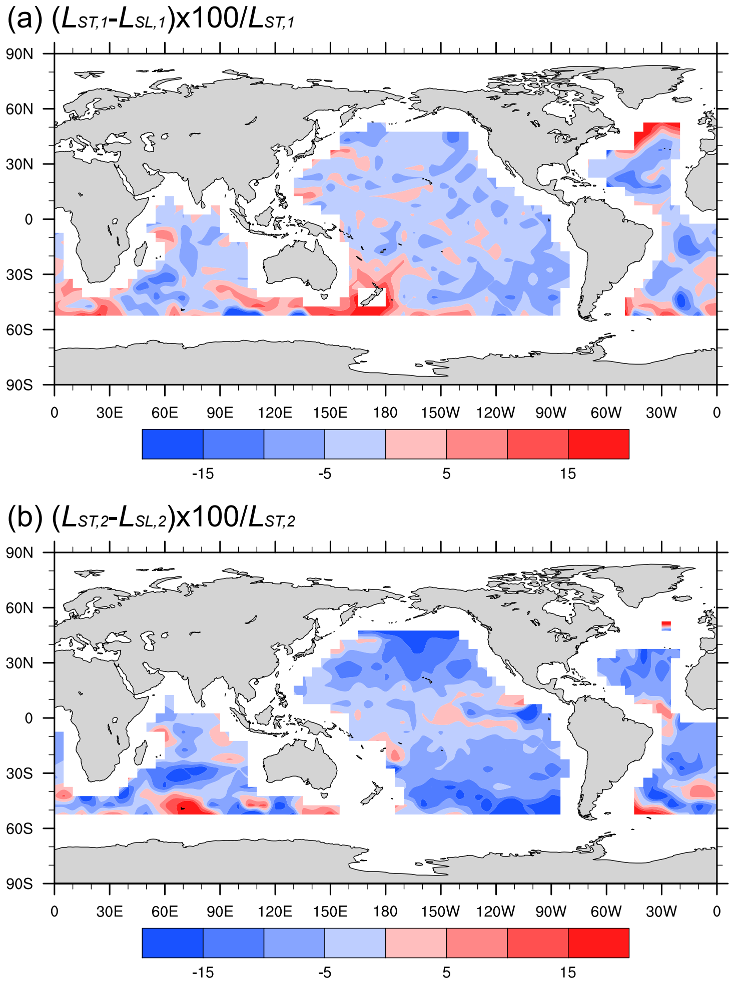
(a) ($L_{ST,1}$-$L_{SL,1}$)x100/$L_{ST,1}$
90N
60N
30N
0
30S
60S
90S
0
30E
60E
90E
120E
150E
180
150W
120W
90W
60W
30W
0
-15
-5
5
15
(b) ($L_{ST,2}$-$L_{SL,2}$)x100/$L_{ST,2}$

Figure 2.8: Differences (%) between $L_{ST,m}$ and $L_{SL,m}$ ($m = 1, 2$) for (a) mode 1 and (b) mode 2 normalized by values of $L_{ST,m}$. Red shading indicates that the values of $L_{ST,m}$ are larger than those of $L_{SL,m}$, whereas blue shading suggests the opposite.

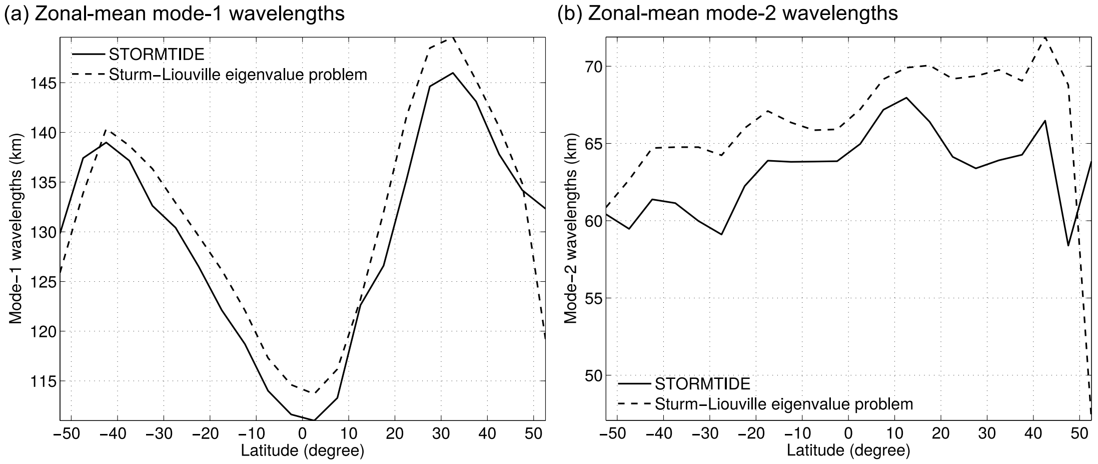

Figure 2.9: Zonal-mean wavelengths of (a) mode 1 and (b) mode 2. The solid line represents $L_{ST,m}$, which is obtained from the STORMTIDE simulation, and the dashed line represents $L_{SL,m}$, which is derived by solving the Sturm-Liouville eigenvalue problem.

is derived by using constant f in Eq. (2.7) with the eigenvalues directly from the eigen solutions [Eq. (2.5)], whereas the other is acquired by setting constant stratification, hence constant ν_m in Eq. (2.7), in the near-global ocean in which f varies realistically with latitudes. Their normalized zonal-mean values, shown in Fig. 2.10a, are independent of the values of N and f that have been chosen. We find a poleward increase of the wavelengths with constant stratification (blue line), a tendency introduced by the dependence of f on latitudes. The wavelengths will further proceed infinity at the critical latitude of about 74.5°N/S, where f approaches the M$_2$ tidal frequency. The wavelengths determined by N only (black line) decrease equatorward in the low latitudes between 28°N and 18°S, and decrease poleward beyond this latitude range, a feature introduced by the variations of ν_m with latitudes.

The normalized zonal-mean $L_{ST,1}$ is also displayed in Fig. 2.10a (red line). Between 28°N and 18°S (region A in Fig. 2.10a), the $L_{ST,1}$ goes up sharper than both theoretical wavelengths, indicating the combined positive contributions from both N and f in determining the wavelengths. In the latitudes between 28° and 33°N and 18° and 42°S (region B), the $L_{ST,1}$ continues rising although N imposes here a negative contribution

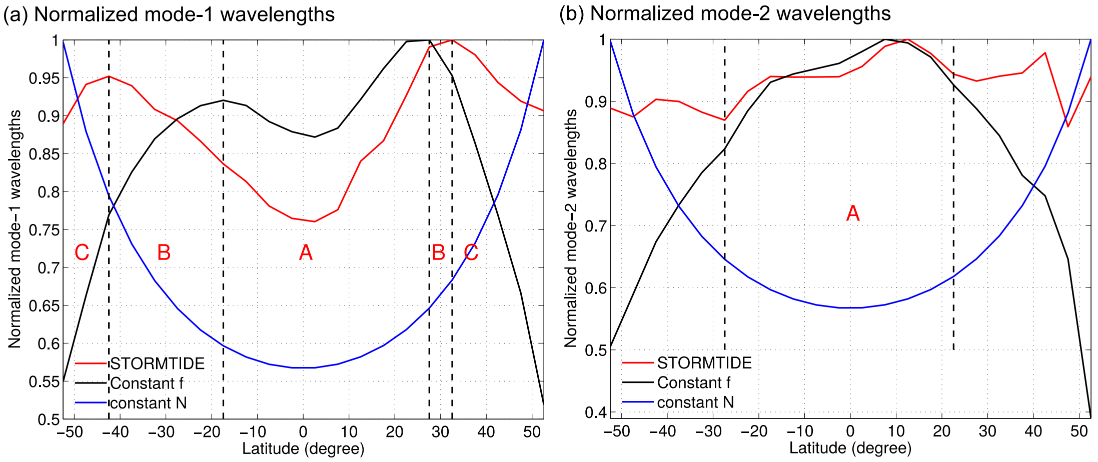

Figure 2.10: Zonal-mean wavelengths of (a) mode 1 and (b) mode 2 derived by the spectral analysis with the simulated M_2 baroclinic velocities (red), by setting constant N, hence constant ν_m in Eq. (2.7) (blue), by setting constant f in Eq. (2.7) with ν_m directly from solving the eigenvalue problem Eq. (2.5) (black). These wavelengths are normalized by their respective maximum. The latitude space is further divided into characteristic regions, denoted by A-C for mode 1 and denoted by A for mode 2, which are further described in the text.

to the wavelengths. Hence, in these two regions, the role of f dominates over that of N. However, poleward beyond 42°S/33°N (region C), the role of N outweighs that of f due to the poleward decrease of $L_{ST,1}$. This explains the differences of our results, specifically for high latitudes, to that of a two-layer model with a horizontally uniform stratification but a latitudinal dependence of f in Simmons et al. (2004a, their Fig. 11). Hence, we conclude that N and f play a combined role in determining the geographical distribution of $L_{ST,1}$.

For the mode 2 wavelengths (Fig. 2.7a), we find that the tendency of a poleward increase in wavelengths almost no longer exists and even reverses in the southern Atlantic and part of the Indian Ocean. Hence, the role of f is significantly weakened in determining $L_{ST,2}$ compared to its role in determining $L_{ST,1}$, consistent with the fact derived from Eq. (2.7) that the same amount of changes in f will lead to smaller changes in mode 2 than in mode 1 as a result of the larger eigenvalues of mode 2. The zonal asymmetry on the other hand is more pronounced for $L_{ST,2}$ than for $L_{ST,1}$, in particular in the Pacific. This feature is also captured in $L_{SL,2}$ (Fig. 2.7b) and in $L_{WKB,2}$ (Fig. 2.7c). It seems that stratification has a stronger influence on $L_{ST,2}$ than on $L_{ST,1}$, consistent with the description that higher modes are more sensitive to the ocean environment (Ray and Zaron 2011), and thus controls the global characteristics of $L_{ST,2}$.

The normalized zonal mean of the simulated mode 2 wavelengths are shown in Fig. 2.10b in comparison with those derived with either N or f fixed. The simulated mode 2 wavelengths (red line) are generally well captured by those derived with constant f (black line) between about 28°S and 23°N (region A in Fig. 2.10b), and they depart outside this latitude range. There is only a slight increasing tendency of $L_{ST,2}$ with increasing latitudes. Hence, f seems not to play a significant role in determining mode 2 wavelengths. In conclusion, the effect of N outweighs that of f in determining the simulated mode 2 wavelengths.

2.7 Applicability of the WKB-simplified eigenvalue problem

As shown in Fig. 2.6c and 2.7c, the WKB-simplified eigenvalue problem [Eq. (2.9)] is able to capture the basic patterns of $L_{SL,1}$ and $L_{SL,2}$. Specifically, the zonal asymmetry, the general poleward increase of the wavelengths and the stronger zonal asymmetry for mode 2 than for mode 1, as identified from the solutions of the STORMTIDE model and the Sturm-Liouville eigenvalue problem, are reproduced. The relative differences between the wavelengths obtained from the Sturm-Liouville and WKB-simplified eigenvalue problems are given by $\frac{L_{SL,m} - L_{WKB,m}}{L_{SL,m}} \times 100\%$ and shown in Fig. 2.11. The global mean relative differences are 6.4% and 5.2% for mode 1 and 2, respectively. Therefore, in a qualitative sense of large-scale variations, the WKB-simplified eigenvalue problem could provide a useful interpretation of the numerical solutions of $L_{SL,m}$, consistent with Chelton et al. (1998).

We now consider the geographical distributions of deviations between these two eigenvalue problems (Fig. 2.11). For mode 1, the WKB-simplified eigenvalue problem overestimates the wavelengths in the tropical oceans and underestimates them in the subtropical oceans (Fig. 2.11a). The differences are smaller than 10% within 77% of the global ocean. Differences larger than 10% are found in the northern Atlantic, the northern and the eastern equatorial Pacific, the Indian Ocean and regions west of Australia. For mode 2, the WKB-simplified eigenvalue problem underestimates the wavelengths in most of the Pacific and Indian Ocean and overestimates them in southern part of the ocean (Fig. 2.11b). In around 90% of the global ocean the relative differences are smaller than 10%. This includes all of the Atlantic and the Indian Ocean, and some of the Pacific. Differences are larger in the equatorial Pacific and in some parts of the South Pacific. Apparently, differences for mode 1 reveal a spatial structure which is different from that for mode 2 (Fig. 2.11). This might be caused by the different sensitivities of the wavelengths of different modes to details of stratification.

Around 10% bias has been described by Chelton et al. (1998) to be too large for many quantitative uses of the WKB approximation. Comparing $L_{WKB,m}$ with $L_{SL,m}$

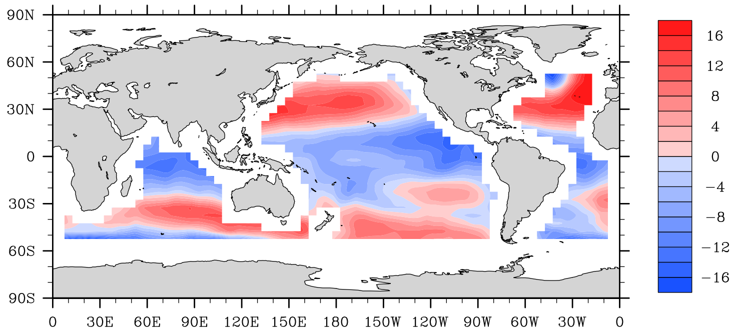
(a) $(L_{SL,1}-L_{WKB,1}) \times 100/L_{SL,1}$
90N
60N
30N
0
30S
60S
90S
0
30E
60E
90E
120E
150E
180
150W
120W
90W
60W
30W
0
16
12
8
4
0
−4
−8
−12
−16

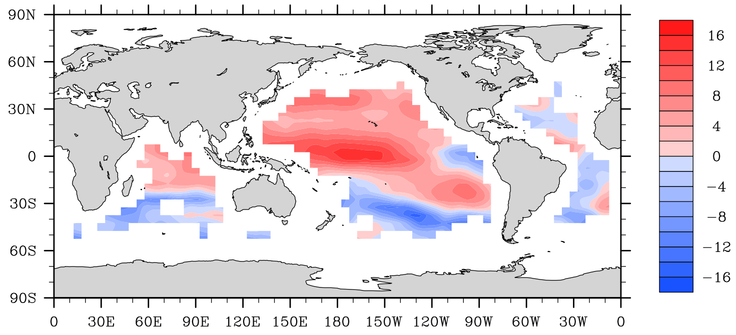
(b) $(L_{SL,2}-L_{WKB,2}) \times 100/L_{SL,2}$
90N
60N
30N
0
30S
60S
90S
0
30E
60E
90E
120E
150E
180
150W
120W
90W
60W
30W
0
16
12
8
4
0
−4
−8
−12
−16

Figure 2.11: Differences (%) between $L_{SL,m}$ and $L_{WKB,m}$ $(m = 1, 2)$ for (a) mode 1 and (b) mode 2 normalized by the values of $L_{SL,m}$. Red shading indicates that values of $L_{SL,m}$ are larger than those of $L_{WKB,m}$, whereas blue shading suggests the opposite.

shows differences up to about 15%, suggesting that the WKB approximation is also problematic in deriving the wavelengths of the M_2 internal tide globally.

2.8 Concluding remarks

With a spectral analysis of the near-global three-dimensional field of model simulated baroclinic tidal velocities, we examined the horizontal wavelength properties of mode 1 and mode 2 M_2 internal tides. The model is a 1/10° primitive equation model that concurrently simulates the ocean circulation and tides. The near-global distributions of the simulated internal tide wavelengths are compared to those obtained by solving the Sturm-Liouville eigenvalue problem. The analysis aims not only to identify the wavelengths of the low-mode M_2 internal tides and their large-scale characteristics, but also to quantify various factors that affect the wavelengths and hence the M_2 internal tide. The following conclusions are drawn.

1. Two modes of the M_2 internal tide are captured by the STORMTIDE model. The mode 1 wavelengths ($L_{ST,1}$) are in the range of 100-160 km. The largest values are above 170 km and exist in strong current regions, for instance, in the Kuroshio and Antarctic Circumpolar Current regions. The geographical distribution reveals a zonal asymmetry and a general tendency of increasing $L_{ST,1}$ with increasing latitude. The model-simulated internal tide mode 2 wavelengths ($L_{ST,2}$) are primarily in the range of 45-80 km. Values larger than 75 km are mainly concentrated in the equatorial regions of the Pacific and in the northeast of the Indian Ocean. The dominant feature of $L_{ST,2}$ is the zonal asymmetry, whereas the latitudinal variations are not as pronounced as that of $L_{ST,1}$. This characteristics is explained by the dispersion relation derived directly from the Sturm-Liouville eigenvalue problem, which depends primarily on the local stratification N and the Coriolis parameter f. Obviously, the zonal asymmetry of the wavelengths is a result of variation in N only, whereas the meridional variations are caused by a combination of changes in N and f. Our analysis shows that for the mode 1 internal tide, the wavelengths are controlled by both N and f. Instead, for the

mode 2 internal tide, the variations of N dominate their spatial characteristics.

2. The STORMTIDE model simulates, to a first approximation, mainly linear internal waves that satisfy the local dispersion relation. The small differences between $L_{ST,1}$ and $L_{SL,1}$ are systematic, with $L_{ST,1}$ being smaller than $L_{SL,1}$ over most of the near-global regions. In high latitudes, larger differences between $L_{ST,m}$ and $L_{SL,m}$ are observed, suggesting important role of nonlinear wave-current interactions there.

3. The WKB-simplified eigenvalue problem is shown to be able to capture the main features of the wavelengths of the low-mode M_2 internal tides. Neglecting details of vertical variations in N that is not captured by the vertical integral of N leads to relative errors up to about 15%.

In general, we find that the spectral peaks are broadened considerably in eddy-active regions, for instance, within the Antarctic Circumpolar Current region. Interactions between mean flows, mesoscale eddies, and internal waves might play a role in determining the wavelengths in these regions. The broadening of the peaks could be a sign of current-induced frequency shifts (Kunze 1985), and thus it implies that frequencies of internal waves are shifted towards or away from the M_2 tidal frequency. With strong frequency shifts, the center of the peaks could also be shifted towards different wavenumbers.

We conclude from this study that the characteristics of internal tides are well described by the global model approach and are consistent with linear waves obtained by solving the local Sturm-Liouville eigenvalue problem. Deviations from linear waves lead to wavelength differences of about 5%-10%. Since these interactions are non-stationary processes, it will be important to further understand these complex mechanisms in order to accurately map the time-dependent characteristics for an advanced processing of future high-resolution satellite altimeter data.

Chapter 3

The K_1 internal tide simulated by a 1/10° OGCM

Using the 1/10° STORMTIDE concurrent simulation of the eddying general ocean circulation and tides, we quantify the characteristics of the low-mode K_1 internal tides by diagnosing the wavelengths from the two-dimensional wavenumber spectral analysis with the simulated baroclinic tidal velocities, whose interpretation is guided by linear wave theory. We further investigate the role of the critical latitude and how the trapping process is simulated in the STORMTIDE model by diagnosing the vertical distributions of the STORMTIDE model-simulated K_1 kinetic energy.

Three to four modes are resolved in the STORMTIDE model for the freely propagating K_1 internal tide. The wavelengths of the first three modes range within 200-400 km, 100-200 km and 60-120 km, respectively. The simulated K_1 internal tides are, to the first approximation, linear waves, exhibiting a zonal asymmetry and a poleward increase, attributed to the role of stratification N and the Coriolis frequency f, respectively. The f-effect is predominant in determining the low-mode wavelengths, although a visible, but much weaker role of N is also observed.

The presence of the critical latitude φ_c separates the characteristics of the freely propagating and trapped K_1 internal tides, with a surface concentration and a bottom amplification of the kinetic energy in the vertical in sub- and supercritical latitudes, respectively, features captured by the STORMTIDE model simulation. The stronger kinetic energy is observed in shallower than deeper regions both equatorward and poleward of φ_c, with a stronger decreasing rate above the bottom and a further upward intensification above the level of the energy minimum in shallower regions in supercritical latitudes.

3.1 Introduction

The barotropic K_1 tides are the dominant diurnal tidal constituent with a period of around 23.935 hours, and are generated by the tidal forcing from the sun and moon on the whole water body. Their interaction with rough topography in the stratified ocean produces internal waves at the K_1 tidal frequency, named the K_1 internal tide. So far, most studies with respect to internal tides have been dedicated to the largest tidal constituent at the M_2 tidal frequency, with specific focuses on the generation, energetics and evolution (e.g., Munk and Wunsch 1998; Niwa and Hibiya 2001; Simmons et al. 2004a; Rainville and Pinkel 2006; Garrett and Kunze 2007; Müller et al. 2012). The M_2 and K_1 internal tides are, however, differing in some important aspects, and the special pattern of the internal tide generation is also very different for the M_2 and K_1 constituents. In the Luson Strait, for instance, the conversion rates from barotropic to internal tides are much larger for the K_1 internal tide (Jan et al. 2007). Furthermore, diurnal tides are strongly modulated on bidecadal time scales and thus the variations of tidal mixing might have important implications for decadal climate variability (Ray 2007). Special effort is thus required to understand the characteristic behaviors of the K_1 internal tide.

Internal tides are generated at topographic features and are either propagating away from, or are trapped to, bottom topography. To separate both features, we define the critical latitude φ_c, where the tidal frequency ω matches the Coriolis frequency f, with $\varphi_c = 30°$ for the K_1 internal tide. Freely propagating internal tides can only be sustained equatorward of φ_c when $f < \omega < N$ is satisfied with N being the buoyancy frequency. Low modes radiate away from the generation sites, carrying most of the energy and leaving about 30% of internal tide energy dissipated locally (St. Laurent et al. 2002). The remote breaking of these low modes away from the original sources contributes to the background diffusivity (normally assumed to be 10^{-5} m^2 s^{-1}) (e.g., Munk and Wunsch 1998; Exarchou et al. 2012). Poleward of the critical latitude, internal tides are still generated due to the ubiquitous presence of barotropic tides, but become subinertial since $\omega < f$; thus they are trapped to topography instead of freely propagating into the ocean's interior (Falahat and Nycander 2015). These waves are called bottom-trapped internal tides, which break and dissipate locally in the vicinity of their generation sites, serving as an efficient driver for vertical mixing over the topography. Hence, a higher dissipation efficiency than 30% is expected for trapped waves, which is, for instance, 80%-100% for the trapped K_1 internal tide at the Kuril Straits (Tanaka et al. 2010).

Internal tides serve as a major component in the energy cascade from barotropic tides to diapycnal mixing through the turbulent processes. These waves, however, cannot be resolved in the coarse-resolution climate or ocean general circulation (OGCMs) models; their effect on extracting energy from barotropic tides in shallow water equations and further on inducing mixing should be parameterized. In the state-of-the-art parameterization of the tidal mixing effect in numerical models, the required internal tide energy flux is parameterized by the simulated barotropic tidal velocities (Jayne and St. Laurent 2001; St. Laurent et al. 2002; Egbert et al. 2004; Jayne 2009; Green and Nycander 2013; Falahat and Nycander 2015). The dissipation efficiency q is an important quantity, which accounts for how much internal tide energy is locally fed into turbulence, and thus needs to be considered. Because numerical models are mostly integrated in time domain, the ω-dependent term (in frequency domain) is traditionally not taken into account in the coarse-resolution OGCMs or climate models. Hence, a constant value of $q \simeq 0.3$ (e.g., St. Laurent et al. 2002, their Eq. (2)) is widely used for all tidal frequencies, globally. This application is obviously problematic in regions with high local dissipation efficiencies, for instance, for trapped waves in supercritical latitudes. An improved parameterization is proposed by Schmittner and Egbert (2014) by separating diurnal and semidiurnal tidal constituents. A complete dissipation ($q = 1$) is assigned to diurnal tides poleward of 30°; the incomplete dissipation ($q = 0.33$) is, however, sustained for semidiurnal tides. This modification improves the diapycnal diffusivity and circulation indices. It indicates that better knowledge of the trapped K_1 internal tide aids in a better parameterization in the OGCMs or climate models.

Since φ_c is located at a low latitude for the K_1 tides, the bottom-trapped K_1 internal tide is present over a considerably large area. Thus, a better understanding of these trapped waves is necessary. It is indicated by Müller (2013) that about 30% of the diurnal internal tide energy is generated poleward of 30°. This estimate is based on a high-resolution OGCM (STORMTIDE; Müller et al. 2012), in which low-frequency motions and tides are simultaneously resolved. On a basis of linear wave theory and the modal decomposition approach, Falahat and Nycander (2015) present the spatial distribution of diurnal tidal energy density and the corresponding energy flux for both K_1 and O_1 internal tides in supercritical latitudes. The important role of bottom-trapped diurnal internal tides in mixing is also recognized in some regional studies (e.g., Nakamura et al. 2000; Fer et al. 2015). However, a detailed global study is not existing on propagation and characteristics of the K_1 internal tide and will be pursued in this study.

In this study, we aim for a better understanding of the characteristics of the K_1 internal tide, quantified by the distributions of the low-mode K_1 internal tide wavelengths. The wavelengths are diagnosed from the baroclinic tidal velocities simulated by the 1/10° STORMTIDE model (Müller et al. 2012) and are compared with those of the Sturm-Liouville eigenvalue problem. We will also investigate the vertical distributions of the K_1 kinetic energy both equatorward and poleward of the critical latitude, involving the propagation of internal tides in a realistic ocean environment. The following questions will be addressed in our study:

1. Which modes of the K_1 internal tide are simulated in the STORMTIDE model and what are their properties, for instance, their wavenumber characteristics,

their wavelengths and the respective geographical distributions?

2. Are these waves consistent with the dispersion relation of linear internal waves? What are the relative roles of N and f in determining these geographical distributions?
3. How is the applicability of the WKB approximation to the K_1 internal tide?
4. What is the role of the critical latitude in determining characteristics of the K_1 internal tide? How is the trapping process simulated in the model?

To answer the first two questions, we perform the two-dimensional wavenumber spectral analysis by using the baroclinic tidal velocities simulated by the 1/10° STORMTIDE model, and compare the resulting wavelengths and their distributions with those derived by solving the Sturm-Liouville eigenvalue problem in which the box-averaged stratification from the STORMTIDE simulation is used. The same methods as described in section 2.3 are used. By comparing the wavelength distributions derived by solving the standard and WKB-simplified eigenvalue problems, the third question will be addressed. To answer the last question, we will analyze the vertical distributions of the K_1 kinetic energy above the topography in different water depth regions, with a particular focus on the distributions poleward of the critical latitude.

In section 3.2, we present the horizontal distributions of the model simulated kinetic energy in both the upper and deep oceans. Section 3.3 describes the characteristics of the wavenumber spectra and the distributions of the resulting wavelengths of the K_1 internal tide along with a comparison with those of linear wave theory. The investigation of the relative roles of N and f is also presented here. The applicability of the WKB approximation to the K_1 internal tide is addressed in section 3.4, while detailed investigation of the role of the critical latitude, including characteristics of the bottom-trapped internal tides, is described in section 3.5. The concluding remarks are given in section 3.6.

3.2 Kinetic energy of the K_1 internal tide

To get an overview of the baroclinic tidal velocities of the 1/10° STORMTIDE model simulation, we show the model-simulated kinetic energy of the K_1 internal tide in the upper (at 100 m) and deep (at 1085 m) oceans in Fig. 3.1a and 3.1b, respectively. Both maps clearly show that most of the kinetic energy is confined within 30°N to 30°S, indicating the presence of the critical latitude in the 1/10° model simulation. Note that with the same model set up, this critical latitude effect is absent in the 0.4° MPI-OM simulation (Fig. C.2 in the Appendix), revealing the significance of the high resolution in internal tide studies.

In subcritical latitudes ($\varphi < \varphi_c$ with φ being the latitude), the energy is most prominent in the Pacific at both 100 m and 1085 m (Fig. 3.1a and 3.1b), especially in the western Pacific, with the Luson Strait as the dominant generating obstacle of the K_1 internal tide. There is, however, solely weak internal tide energy in the eastern Pacific, in large part due to the relatively smooth topography compared to the western Pacific. A high energy level shows up also in the Hawaiian Ridge and the Tuamotus in the Pacific as a result of the rough topography, and in low latitudes in the Indian Ocean, attributed to the intense interaction of significant barotropic tidal flows with rough topography there. The kinetic energy in the Atlantic is, however, evidently much weaker than those in the other two basins, which would be accounted for, at least in part, by the weaker K_1 barotropic tidal currents throughout most of the Atlantic (Egbert and Ray 2003).

The K_1 energy level is much lower in supercritical ($\varphi > \varphi_c$) than subcritical latitudes (Fig. 3.1a and 3.1b). The K_1 internal tide is subinertial ($\omega < f$) poleward of 30° and cannot freely radiate away from the generation site. Hence, the strong kinetic energy is located primarily only directly over rough topography in the northern Pacific, such as along the Kuril Islands, the Aleutian Islands and the Emperor Seamounts expanding northwest of the Hawaiian Ridge. Relatively energetic motions are also produced in the Southern Ocean around the Antarctic, involving in particular the southeast of New

(a) Kinetic energy, 100 m

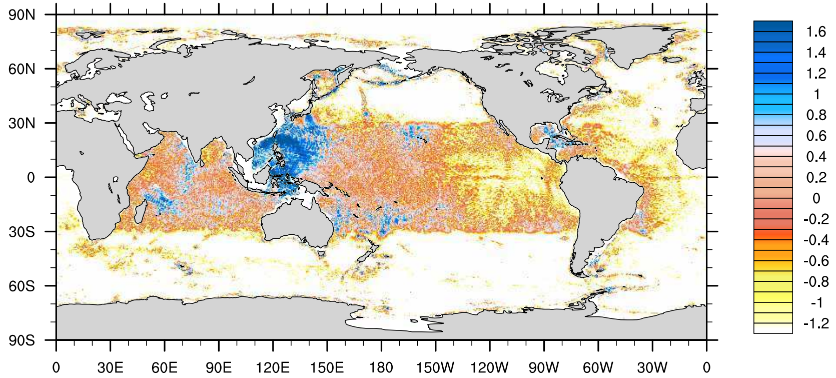
90N
60N
30N
0
30S
60S
90S
0
30E
60E
90E
120E
150E
180
150W
120W
90W
60W
30W
0
1.6
1.4
1.2
1
0.8
0.6
0.4
0.2
0
-0.2
-0.4
-0.6
-0.8
-1
-1.2

(b) Kinetic energy, 1085 m

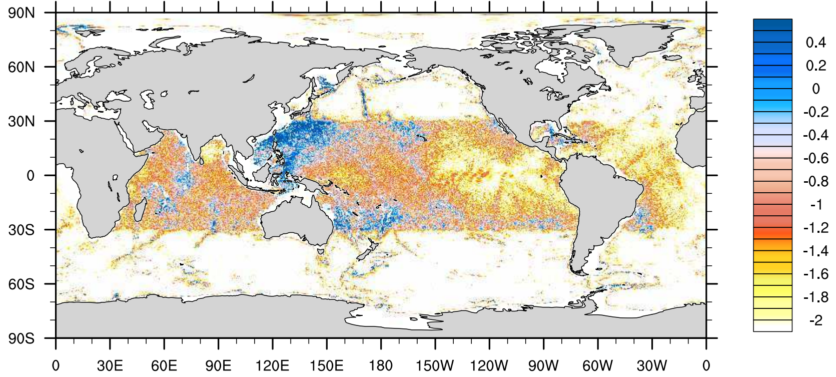
90N
60N
30N
0
30S
60S
90S
0
30E
60E
90E
120E
150E
180
150W
120W
90W
60W
30W
0
0.4
0.2
0
-0.2
-0.4
-0.6
-0.8
-1
-1.2
-1.4
-1.6
-1.8
-2

(c) Vertical integral of the kinetic energy

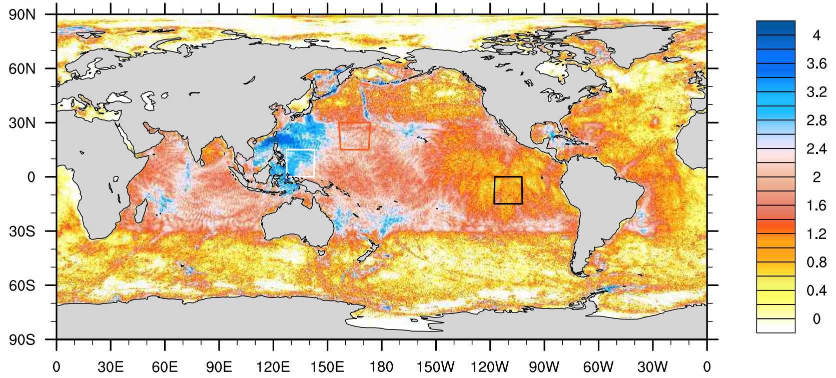
90N
60N
30N
0
30S
60S
90S
0
30E
60E
90E
120E
150E
180
150W
120W
90W
60W
30W
0
4
3.6
3.2
2.8
2.4
2
1.6
1.2
0.8
0.4
0

Figure 3.1: Kinetic energy ($\mathrm{cm}^2\ \mathrm{s}^{-2}$) of the K_1 internal tide in logarithmic scales at (a) 100 m and (b) 1085 m, which are simulated by the 1/10° STORMTIDE model. They are derived by $(A_{u_{bc}}^2 + A_{v_{bc}}^2)/2$, with $A_{u_{bc}}$ and $A_{v_{bc}}$ being amplitudes of the K_1 baroclinic zonal and meridional velocities, respectively. (c) The vertical integral of the K_1 kinetic energy ($\mathrm{J\ m}^{-2}$) in logarithmic scales derived by $\int_{-H}^{0} \rho_w (A_{u_{bc}}^2 + A_{v_{bc}}^2)/2dz$, with ρ_w being the density of seawater and H water depth. Boxes denote the regions in which the wavenumber spectra will be be introduced later.

Zealand and the Pacific-Antarctic Ridge. All these hot spots indicate strong generation of the bottom-trapped K$_1$ internal tide in supercritical latitudes.

The vertical integral of the K$_1$ kinetic energy is displayed in Fig. 3.1c, representing again the existence of the critical latitude and hot spots of the kinetic energy both poleward and equatorward of φ_c, resembling the distributions described above. The beam-like structures are more evident in the vertical integral (Fig. 3.1c) than at a single depth (Fig. 3.1a and 3.1b), indicating the propagation directions of the free K$_1$ internal tide in subcritical latitudes.

3.3 Wavelengths of the model-simulated K$_1$ internal tide

In general, we adopt the same methods for the K$_1$ internal tide as used in the M$_2$ analysis of the STORMTIDE simulation (section 2.3). Note that both tidal constituents are derived from the same model simulation.

3.3.1 Characteristics of the wavenumber spectra

The two-dimensional wavenumber spectra indicate not only the magnitudes of the wavenumber vectors, but also the directions of wave propagation. In this study, the spectra are obtained in boxes of the size $15°/cos\varphi$ (in longitude) $\times 15°$ (in latitude), with φ being the latitude, for the K$_1$ internal tide. Spectra in a few selected boxes will be discussed in the following.

The two-dimensional spectra of the kinetic energy are shown in Fig. 3.2 (left column), denoted by $S_{KE}(k, l)$ with k and l being the zonal and meridional wavenumbers, respectively, in the box centered at (135°E, 7.55°N); this box is highlighted in white in Fig. 3.1c, exhibiting strong K$_1$ internal tide energy. The spectrum in Fig. 3.2a is derived at 100 m. We can clearly see an almost closed energetic circle with the wavenumber centered at around 0.004-0.005 km^{-1}, corresponding to a wavelength of about 200-250 km. This energetic circle further reveals an evident zonal asymmetry in the energy distribution, indicating a preferably eastward propagation of the waves with more concentrated energy in the eastern half circle, in particular along lines that are 45° to the zonal direction. This characteristic propagation direction is closely related to the local geographic features. Located at the Philippine Sea, we can see in Fig. 3.1c that there are two principal sources for the K_1 internal tide injected into this box. On the one hand, internal tides radiate away after their generation over the Philippine Trench, and partially propagate northeastward into the Philippine Sea. These waves are revealed in the wavenumber spectrum $S_{KE}(k,l)$ along the 45° line, directing to the northeast. On the other hand, there is an evident southeastward injection of waves into this box from the northern boundary, originating apparently from the Luson Strait. This southeastward propagation is revealed in Fig. 3.2a as well, along the line 45° southward to the zonal direction.

The one-dimensional wavenumber spectrum $S_{KE}(K)$ at 100 m, converted from $S_{KE}(k,l)$ with $K = \sqrt{k^2 + l^2}$ being the horizontal wavenumber, is displayed in Fig. 3.2b. The scatters correspond to each individual points in $S_{KE}(k,l)$. Variations of the scatters at a specific wavenumber are caused by the inhomogeneity of the energy distribution in the (k,l) plane along each wavenumber circle that indicates the anisotropy of wave propagations. Detailed information of wave propagations is, however, lost through this transformation. The energetic circle in Fig. 3.2a is further represented as a prominent peak in the one-dimensional spectrum obtained by the bin averages of all values of $S_{KE}(K)$ inside the respective intervals (Fig. 3.2b). This peak is named the low-wavenumber peak.

Closely beyond this low-wavenumber circle to the east, we observe another less energetic half circle in Fig. 3.2a, which is found to be more evident at 560 m (Fig. 3.2c) where the vertical modal structure of mode 2 experiences its interior maximum in this given box. This circle, named the mid-wavenumber circle, presents almost the same energy level as the low-wavenumber circle at 560 m; both energetic circles are reflected by prominent spectral peaks in $S_{KE}(K)$ (Fig. 3.2d), reflecting a similar amount of the kinetic energy. The mid-wavenumber circle is located at around 0.007-0.008 km^{-1} (Fig. 3.2c), corresponding to a wavelength of about 125-140 km, with relatively weak energy

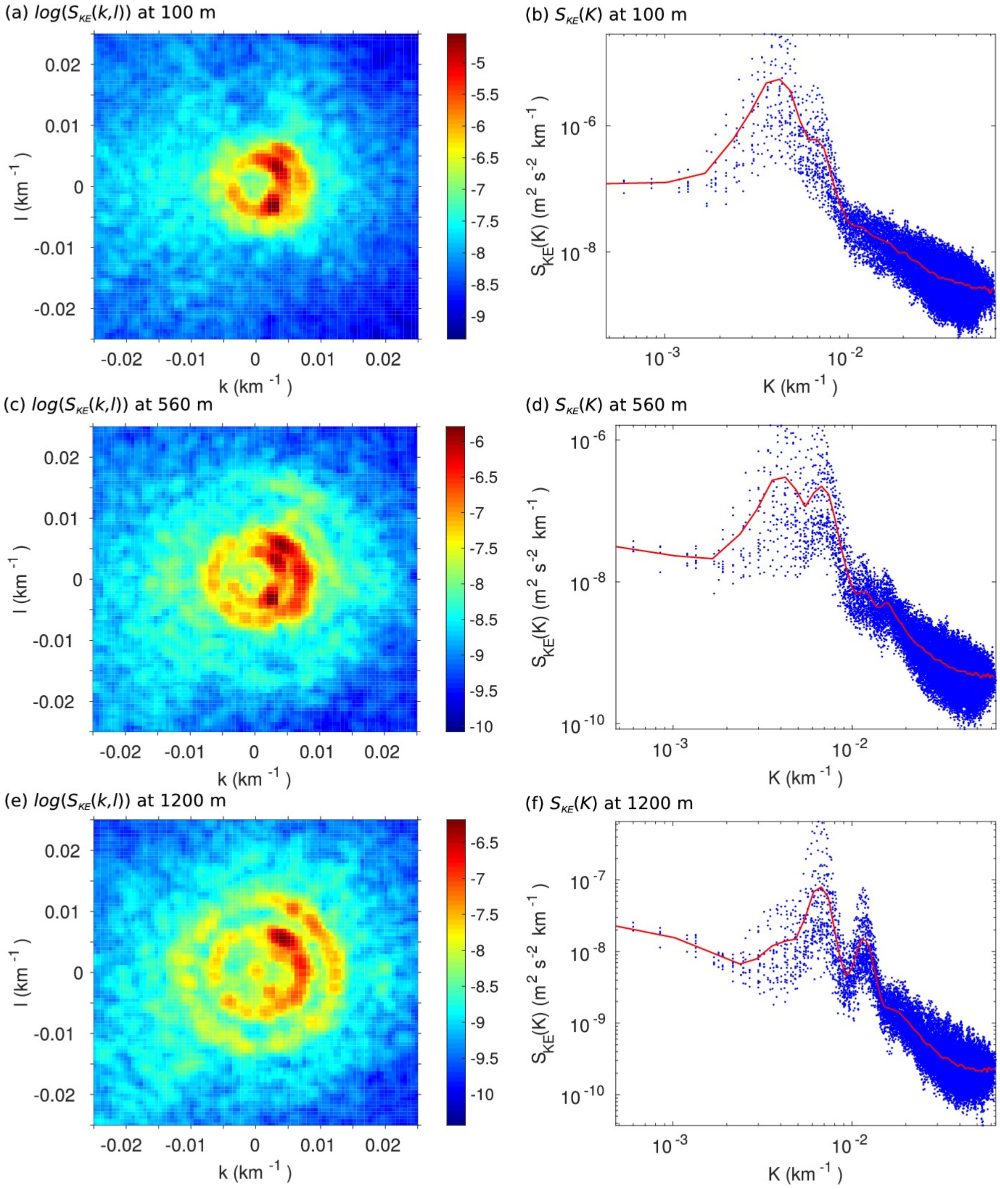

Figure 3.2: Wavenumber spectra $S_{KE}(k, l)$ (m^2 s^{-2} km^{-1}, in logarithmic scales) of the kinetic energy of the K$_1$ internal tide in the $15°/cos\varphi \times 15°$ box centered at (135°E, 7.55°N) at (a) 100 m, (c) 560 m, and (e) 1220 m. The resolved ranges of k and l are within -0.045-0.044 km^{-1}, but we show only the energetic range of -0.025-0.025 km^{-1} to enhance the readability. In the right column, wavenumber spectra $S_{KE}(K)$ are converted from the respective $S_{KE}(k, l)$ using $K = \sqrt{k^2 + l^2}$. The scatters are converted directly from each value of $S_{KE}(k, l)$. The red lines represent the bin averages of $S_{KE}(K)$, in which $S_{KE}(K_i)$ at the i^{th} interval is obtained by averaging all values of $S_{KE}(K)$ with K inside the interval (K_i,K_i+ $\triangle$). We consider a total of 100 consecutive intervals. Term $\triangle$ is obtained by dividing the total resolved wavenumber range by 100.

emerging at even higher wavenumbers. Waves associated with the mid-wavenumbers are strongly directed to the east. In particular, the high energy level in the northeast indicates a larger injection of the K_1 internal tide from the Philippine Trench than from the Luson Strait at this depth.

Down to the deeper ocean, the spectrum in Fig. 3.2e is derived at 1220 m where mode 3 undergoes its second (deeper) interior maximum in the vertical distribution. Here we still capture the strong mid-wavenumber circle, whereas the one related to the low wavenumber is rather weak and emerges only partially. There is another circle appearing at even higher wavenumber of around 0.012-0.013 km^{-1} with a wavelength of about 80 km. It is thus referred to as the high-wavenumber circle. Its lower energy level than the mid-wavenumber circle is consistent with the distribution of $S_{KE}(K)$ (Fig. 3.2f), where the energy level is almost one order of magnitude lower for the high- than mid-wavenumber peaks, while the low-wavenumber peak is almost unrecognizable. Similar as the mid-wavenumber circle, waves associated with the high-wavenumbers (Fig. 3.2e) prefer to propagate eastward, in particular to the northeast, revealing the predominance of the K_1 internal tide from the Philippine Trench. In general, due to the relatively long distance from the Luson Strait to the considered region, the significance of the K_1 internal tide originating from the Luson Strait is only observed for the low-wavenumber motions, but not for the mid- and high-wavenumber motions owing to their slow propagation speed.

To get a more general overview of the characteristics of the K_1 wavenumber spectra, results in the box centered at (110°W, 7.45°S) (the box highlighted in black in Fig. 3.1c) are displayed in Fig. 3.3. The spectra are derived at 100 m, 740 m and 1365 m, depths with the same definition as used in Fig. 3.2, representing the diagnosis of the low-, mid- and high-wavenumber peaks, respectively. The energy distributions of $S_{KE}(k, l)$ (left column of Fig. 3.3) reveal strong asymmetries, much more pronounced in the meridional than zonal directions. Hence, the K_1 internal tide in this given box mainly propagates in the northward direction. Furthermore, the meridional asymmetry is found to be most evident for the mid-wavenumber waves, but least evident for the low-wavenumber waves. The three peaks (right column of Fig. 3.3) present at the wavenumbers of about 0.005 km^{-1}, 0.01 km^{-1} and 0.015 km^{-1}, respectively, corresponding to the wavelengths of about 200 km, 100 km, 67 km, independent of depth. Interestingly though, a fourth circle with relatively weak energy is found to emerge at even higher wavenumbers in Fig. 3.3c and 3.3e, whose existence and consistency at both depths are also reflected by $S_{KE}(K)$ (Fig. 3.3d and 3.3f). Hence, differing from the results described in Fig. 3.5, four energetic peaks, instead of three, in $S_{KE}(K)$ are captured by the spectral analysis at the three selected depths.

We further show an example for a box close to the critical latitude. In Fig. 3.4, we show the spectra in the box centered at (165°E, 22.55°N) (the box highlighted in red in Fig. 3.1c), where the K_1 tide approaches its critical latitude at 30°N in the poleward boundary of the considered region. The spectra are derived at 100 m, 845 m and 1365 m, respectively. The energy circles are not easily distinguishable in $S_{KE}(k,l)$ at 100 m (Fig. 3.4a); three isolated peaks are, however, still revealed in the corresponding $S_{KE}(K)$ (Fig. 3.4b). Hence, we can still diagnose the low wavenumber to be located at roughly 0.0025 km^{-1}, related to the wavelength of about 400 km, albeit a broader low-wavenumber peak of $S_{KE}(K)$ at 100 m (Fig. 3.4b) than the previous ones (Fig. 3.2b and 3.3b). The energy circles at 845 m (Fig. 3.4c and 3.4d) are better split, showing a wavenumber of about 0.005 km^{-1} and a related wavelength of about 200 km. Further downward to 1365 m, two obvious circles, associated with the mid- and high-wavenumber waves, are presented in $S_{KE}(k,l)$ (Fig. 3.4e). The mid-wavenumber circle is again located at the wavenumber of around 0.005 km^{-1} (Fig. 3.4f), while the high-wavenumber circle is presented at the wavenumber of about 0.01 km^{-1} corresponding to a wavelength of 100 km. Fig. 3.4 generally presents the common features of the spectral circles that are not well split in regions near the critical latitude as a result of the larger length scales of the K_1 internal tide there. However, we are still able to capture the wavenumbers (hence the wavelengths) of the isolated peaks through the conversion from $S_{KE}(k,l)$ to $S_{KE}(K)$. In general, the K_1 internal tidal peaks diagnosed from the wavenumber spectral analysis are more isolated from each other in lower- than

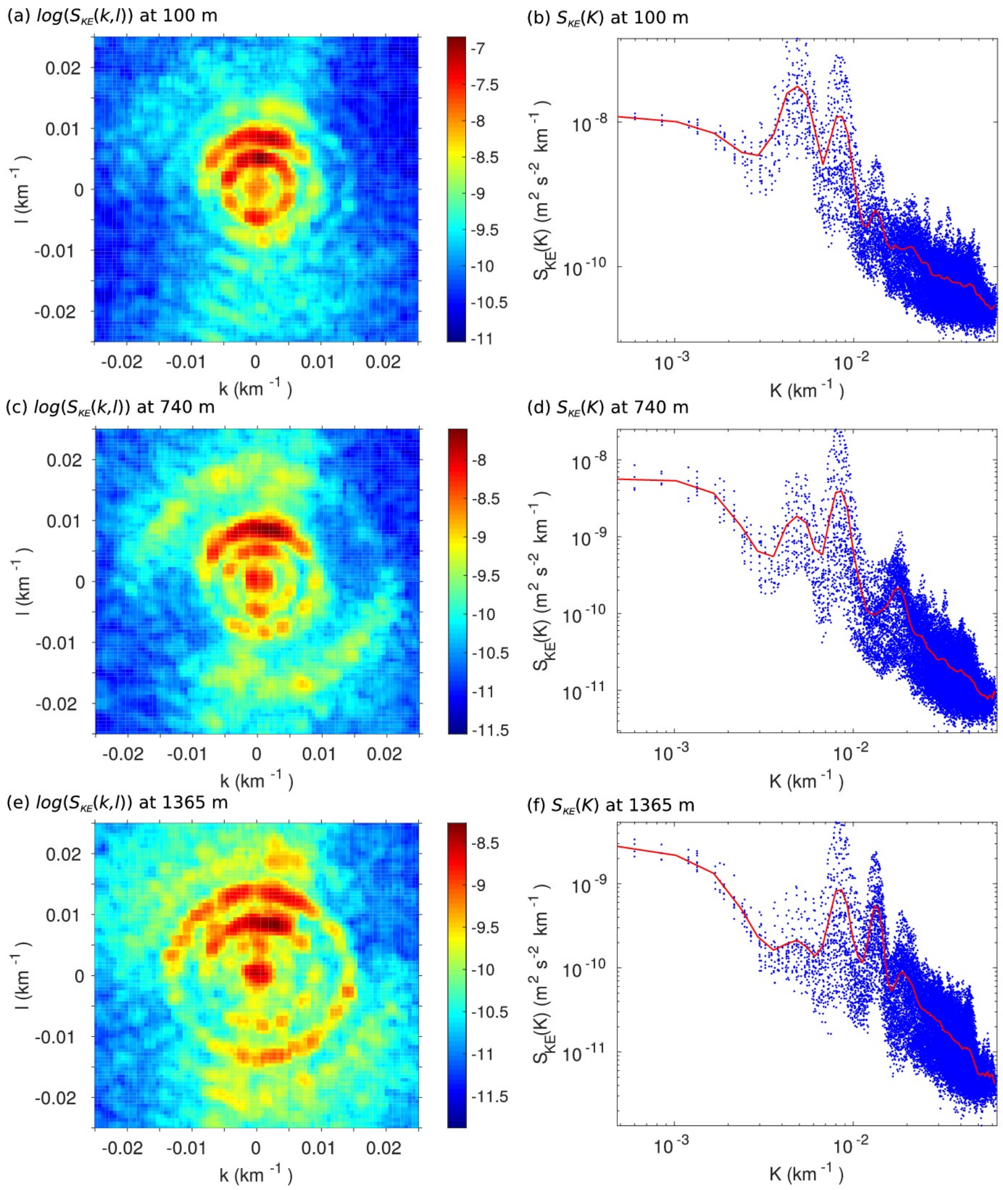

Figure 3.3: Wavenumber spectra $S_{KE}(k,l)$ (m^2 s^{-2} km^{-1}, in logarithmic scales) of the STORMTIDE-simulated kinetic energy of the K$_1$ internal tide in the $15°/cos\varphi \times 15°$ box centered at (110°W, 7.45°S) at (a) 100 m, (c) 740 m, and (e) 1365 m. In the right column, wavenumber spectra $S_{KE}(K)$ converted from the respective $S_{KE}(k,l)$ using $K = \sqrt{k^2+l^2}$, with K, k and l being the horizontal, zonal and meridional wavenumbers, respectively. Other details are the same as described in Fig. 3.2.

in higher-latitude oceans.

To obtain an overview of the entire vertical distributions of the wavenumber spectra, we show the spectral distributions over all depths from the surface to ocean bottom derived in the box centered at (135°E, 7.55°N) in Fig. 3.5, the same box as used in Fig. 3.2. We observe three groups of peaks that are denoted by I, II and III in Fig. 3.5a. The low-wavenumber peak (group I) undergoes an energy reduction from the surface to about 1220 m, where the peak vanishes, and then a slight energy rise downward until the bottom. The energy of the mid-wavenumber peak (group II) reduces gradually from the surface to 220 m where the peak disappears. Afterwards the energy increases firstly with depth and then decreases until dying out again at 1885 m. The energy reemerges further downward. There is a more complicated structure of the energy variations of the high-wavenumber peak (group III). The strongest energy shows up at the surface. Observing closely, we find three depths, 122 m, 645 m and 2290 m, at which the high-wavenumber peak cannot be detected.

In order to understand the spectral distributions in Fig. 3.5a, we consider here the vertical modal structures of the low-mode K_1 kinetic energy that are derived by solving the Sturm-Liouville eigenvalue problem. Results are shown for the first three modes of the K_1 internal tide in the box centered at (135°E, 7.55°N) in Fig. 3.5c, derived by solving the standard eigenvalue problem with the box-averaged N in Fig. 3.5b. We can see that mode 1 has its minimum where the energy becomes zero at 1260 m, while there are two minima for mode 2 at 200 m and 1870 m, and three minima for mode 3 at about 120 m, 650 m and 2360 m, respectively. Variations of these modal structures from linear theory are consistent with the vertical energy distributions of the wavenumber spectra in Fig. 3.5a, which proves that the three groups of peaks (I, II and III) represent mode 1 to 3, respectively, in the considered box.

We further provide the vertical energy distributions of the wavenumber spectra in the other two boxes (Fig. 3.6a and 3.7a) as used in Fig. 3.3 and 3.4. It is found that four groups of peaks are observed for the K_1 internal tide in Fig. 3.6a, which correspond to mode 1 to 4, respectively, diagnosed from the same comparison between the vertical

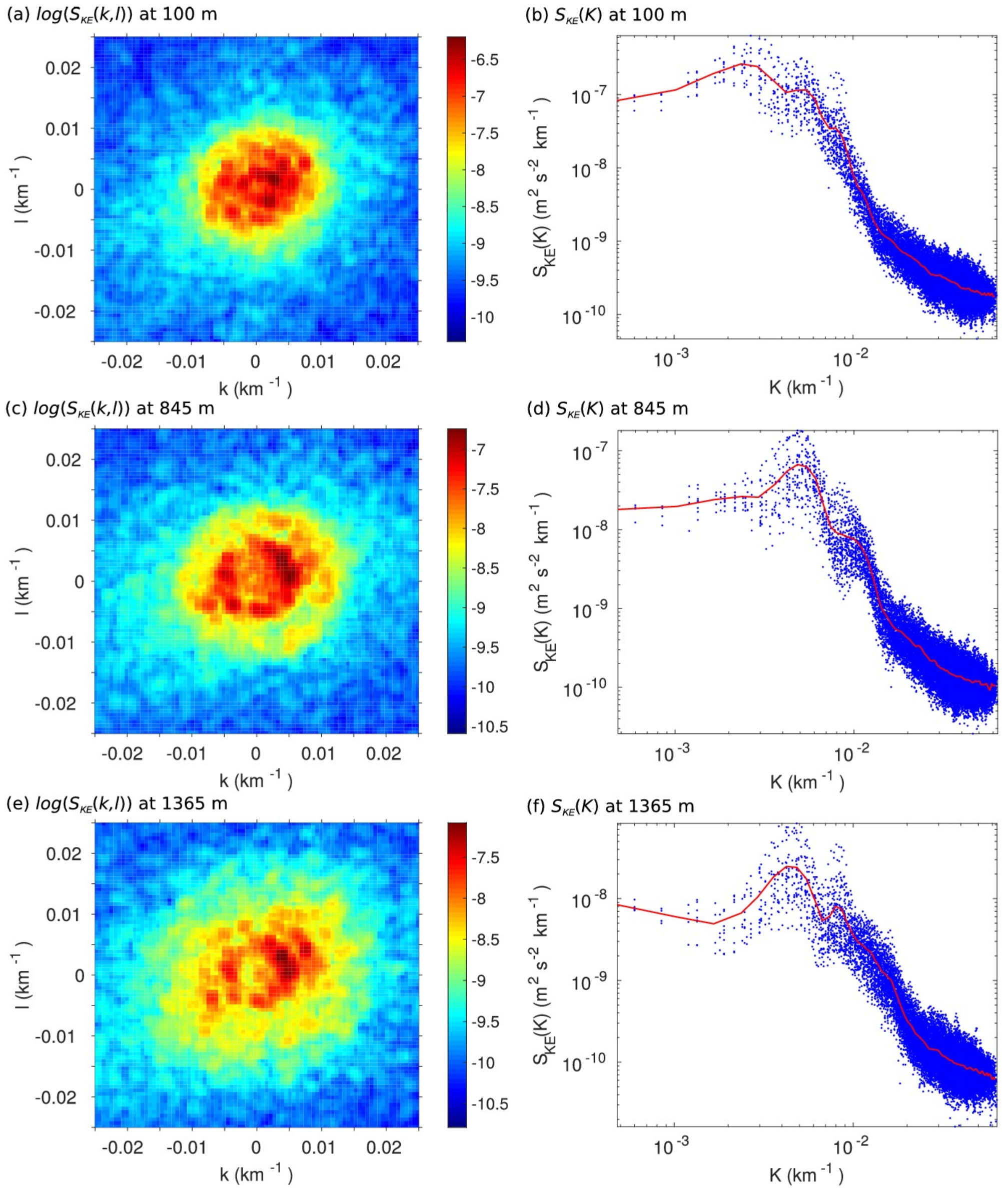

Figure 3.4: Wavenumber spectra $S_{KE}(k,l)$ (m^2 s^{-2} km^{-1}, in logarithmic scales) of the STORMTIDE-simulated kinetic energy of the K$_1$ internal tide in the $15°/cos\varphi \times 15°$ box centered at (165°E, 22.55°N) at (a) 100 m, (c) 845 m, and (e) 1365 m. In the right column, wavenumber spectra $S_{KE}(K)$ are converted from the respective $S_{KE}(k,l)$. Other details are the same as described in Fig. 3.2.

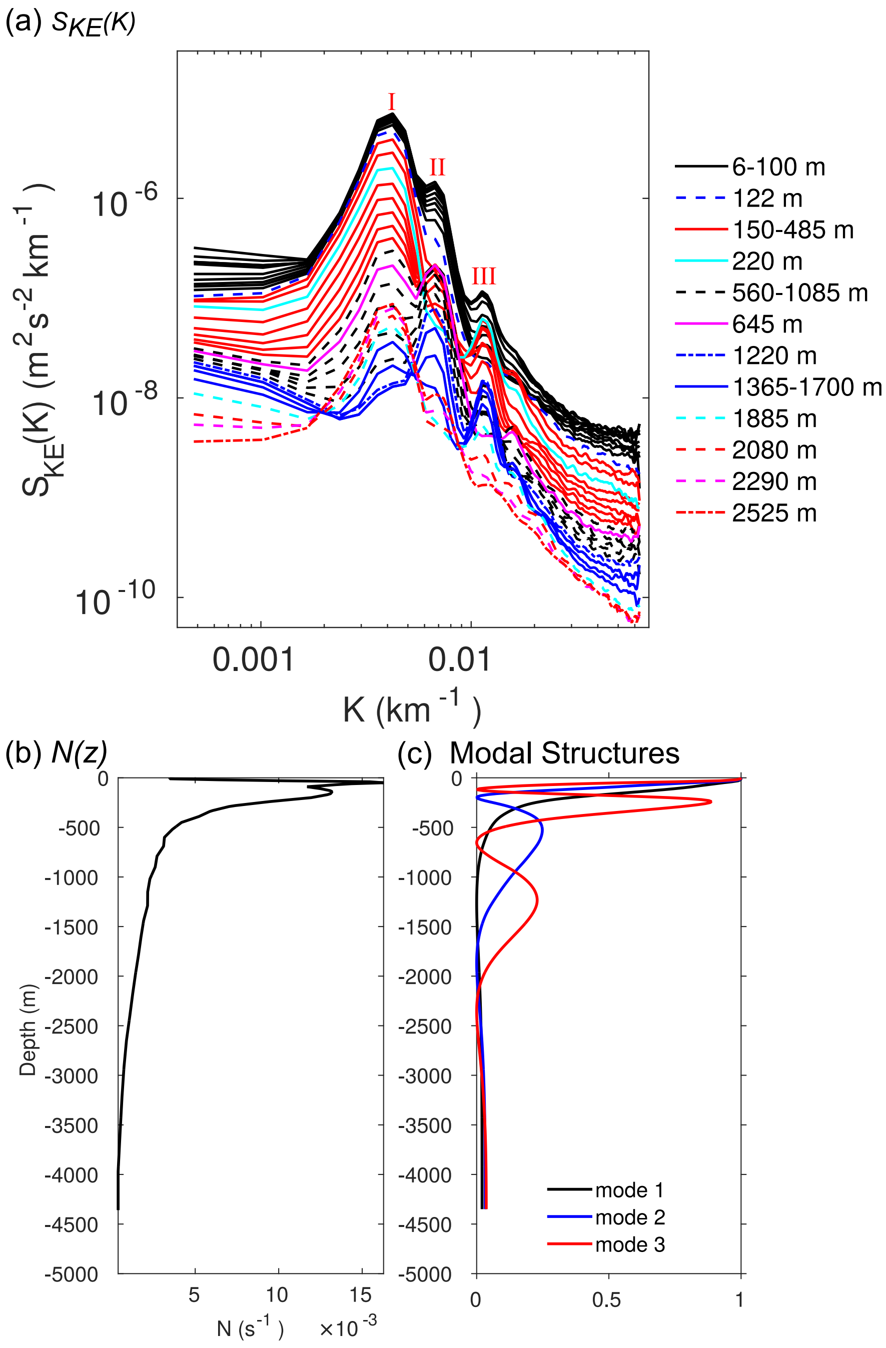

Figure 3.5: (a) Bin-averaged spectra $S_{KE}(K)$ of the kinetic energy of the K$_1$ internal tide for the box centered at (135°E, 7.55°N). (c) The vertical modal structures of the first three modes of the kinetic energy in the considered box, which are proportional to $[dw_m(z)/dz]^2$ with $w_m(z)$ being the eigenfunction. These structures are derived by solving the Sturm-Liouville eigenvalue problem with (b) the box-averaged stratification profile simulated by the STORMTIDE model. The zero crossings of mode 1 to 3 diagnosed from the modal structures are at (1260 m), at (200 m, 1870 m), and at (120 m, 650 m, 2360 m), respectively.

energy distributions of the wavenumber spectra and the modal structures derived by solving the Sturm-Liouville eigenvalue problem as mentioned above (details not given). Furthermore, three groups of peaks are observed in Fig. 3.7a which are proved to be related to the first three modes of the K_1 internal tide, respectively. Although the detailed diagnosis is not described here, the information required to do the diagnosis is provided as a reference in Fig. 3.6a and 3.7a for the respective vertical distributions of the spectral energy, in Fig. 3.6c and 3.7c for their respective modal structures, and in Fig. 3.6b and 3.7b for the box-averaged stratification that is used in solving the standard Sturm-Liouville eigenvalue problem. Since a fourth mode is not universally captured by the spectral analysis at selected depths with the STORMTIDE simulation, we diagnose only the wavelengths of the first three modes.

3.3.2 Geographical distributions of the K_1 wavelengths

The wavenumber spectral analysis at selected depths in section 3.3.1 ensures the presence of each modal peak in the one-dimensional spectra $S_{EK}(K)$. Hence, the mode-1 K_1 wavelengths are all derived at 100 m in the considered oceans for different boxes with 5° movement away from each other in the horizontal. The spectral analysis is, however, performed at varying depths for the wavelengths of modes 2 and 3, rather than at a constant depth of 1085 m as done for the mode-2 M_2 internal tide in Chapter 2.

Furthermore, it is difficult to obtain the geographical distributions of the wavelengths in supercritical latitudes because of the highly inhomogeneous distributions and the strong local dissipation (rather than free propagation) of the K_1 internal tide there. We thus perform the spectral analysis solely in subcritical latitudes where internal tides are freely propagating after their generation. That means we consider only from the equator to the most northern/southern boxes that are centered at 22.5°N/S and expand over 15° in the meridional direction until 30°N/S, where the critical latitude is present for the K_1 internal tide.

The simulated mode-1 wavelengths $L_{ST,1}$ of the K_1 internal tide are shown in Fig.

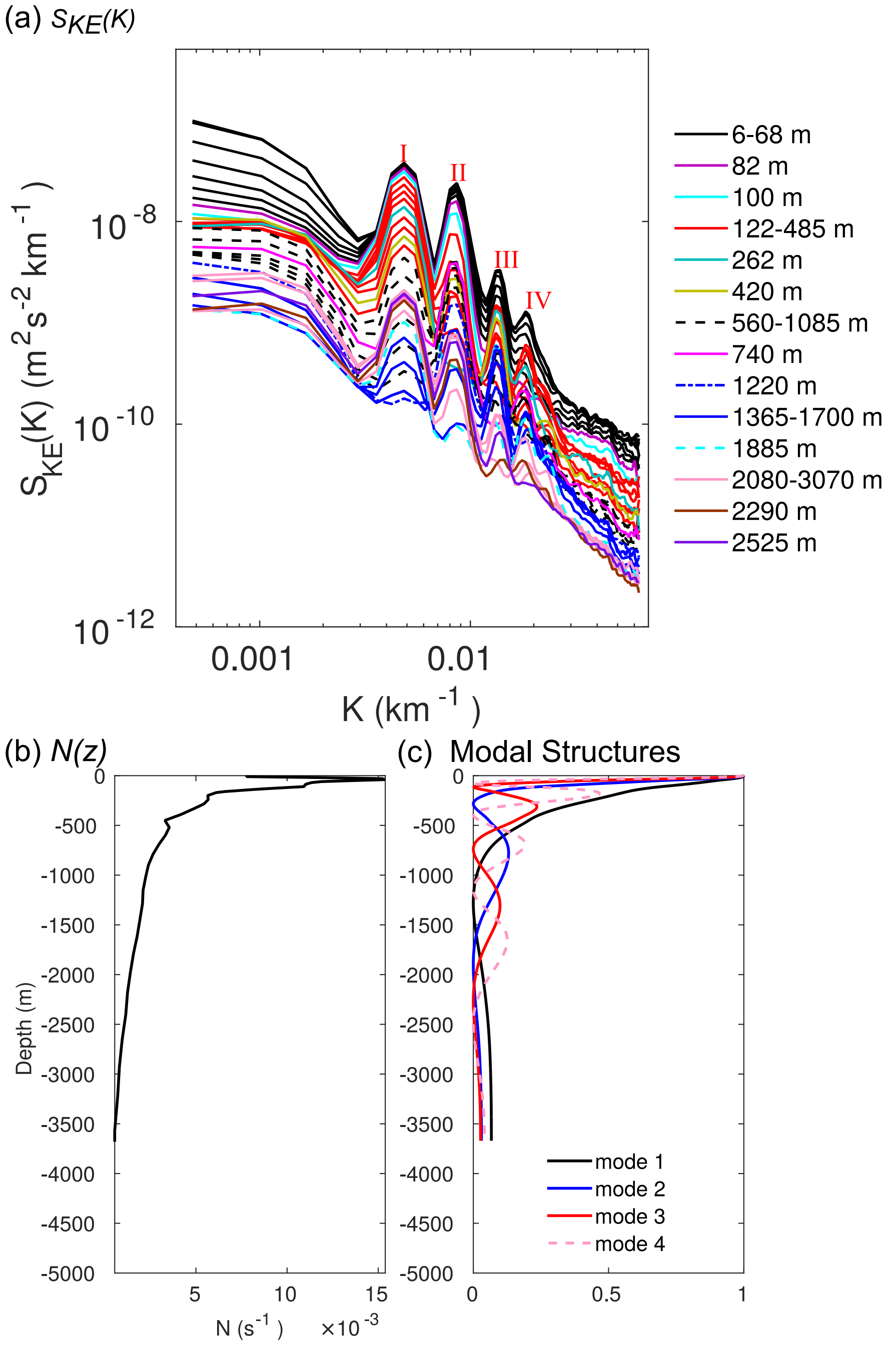

Figure 3.6: The same as Fig. 3.5, but for the box centered at (110°W, 7.45°S). The zero crossings of mode 1 to 3 diagnosed from the modal structures are at (1280 m), at (280 m, 1900 m), and at (110 m, 740 m, 2270 m), respectively.

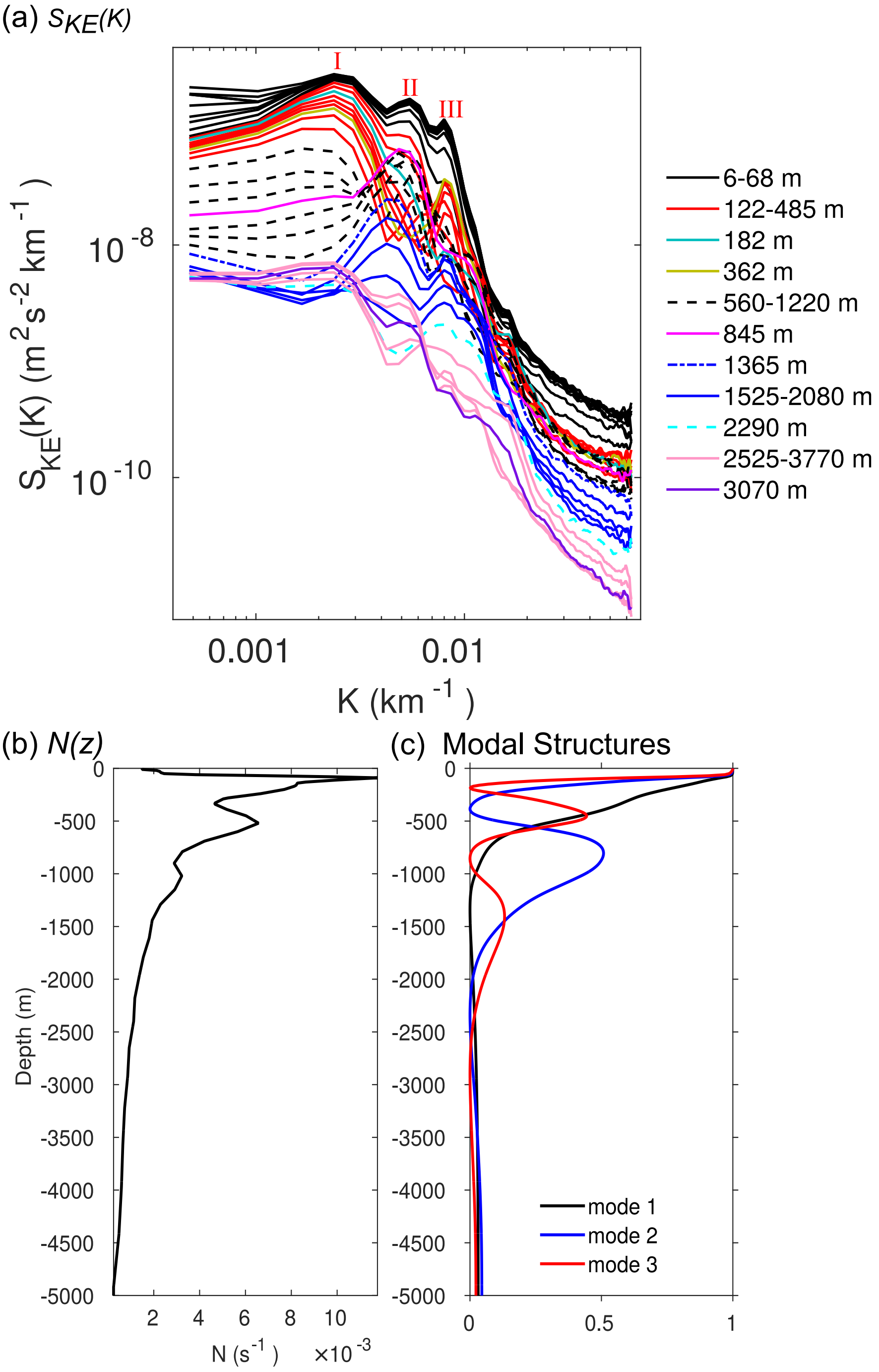

Figure 3.7: The same as Fig. 3.5, but for the box centered at (165°E, 22.55°N). The zero crossings of mode 1 to 3 diagnosed from the modal structures are at (1340 m), at (390 m, 2340 m), and at (190 m, 860 m, 2910 m), respectively.

3.8a, within a range of 200-400 km. The most prominent feature is a poleward increase in all three ocean basins, particularly strong in the Pacific. The wavelengths rise in the Pacific from about 200 km in the equator to over 400 km near the critical latitude. Compared to this poleward increase, a zonal asymmetry is less pronounced, but exists in all three ocean basins. We observe the strongest zonal asymmetry in the Pacific, with larger values in the western than in the eastern Pacific in low latitudes.

(a) STORMTIDE ($L_{ST,1}$)

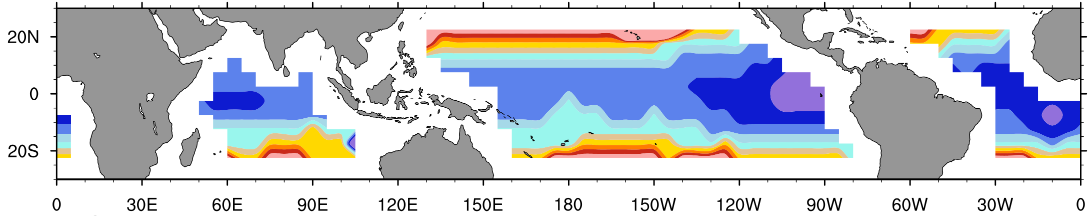
20N
0
20S
0
30E
60E
90E
120E
150E
180
150W
120W
90W
60W
30W
0

(b) Sturm-Liouville eigenvalue probelm ($L_{SL,1}$)

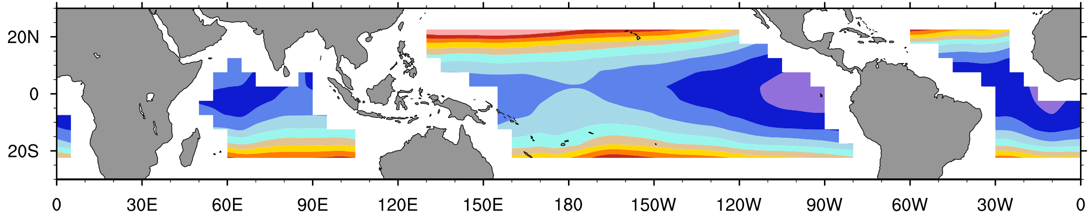
20N
0
20S
0
30E
60E
90E
120E
150E
180
150W
120W
90W
60W
30W
0

(c) WKB-simplified eigenvalue problem ($L_{WKB,1}$)

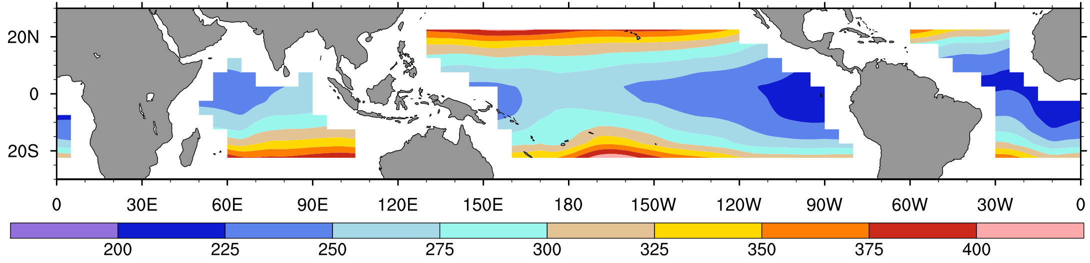
20N
0
20S
0
30E
60E
90E
120E
150E
180
150W
120W
90W
60W
30W
0
200
225
250
275
300
325
350
375
400

Figure 3.8: Mode-1 wavelengths (km) of the K_1 internal tide, derived (a) by applying the spectral analysis to the STORMTIDE-simulated baroclinic tidal velocities at 100 m, (b) by solving the Sturm-Liouville eigenvalue problem with the box-averaged stratification that are simulated by the STORMTIDE, and (c) by solving the WKB-simplified Sturm-Liouville eigenvalue problem. The same box-averaged stratification has been used for both eigenvalue problems.

The simulated K_1 wavelengths range within 100-200 km for mode 2 ($L_{ST,2}$ in Fig. 3.9a) and within 70-120 km for mode 3 ($L_{ST,3}$ in Fig. 3.10a), showing a relatively small range in the Indian Ocean. These wavelength distributions capture a zonal asymmetry and a poleward increase in all three basins as observed in $L_{ST,1}$. The largest variations of the wavelengths occur in the Pacific with the smallest values in the eastern equatorial Pacific and the largest values near the critical latitude, which reveal simultaneously the zonal asymmetry and the poleward increase. In conclusion, both general features captured in the wavelengths of the first three modes indicate the presence of common factors that control the behaviors of the lowest three modes in a similar way, which will be investigated later.

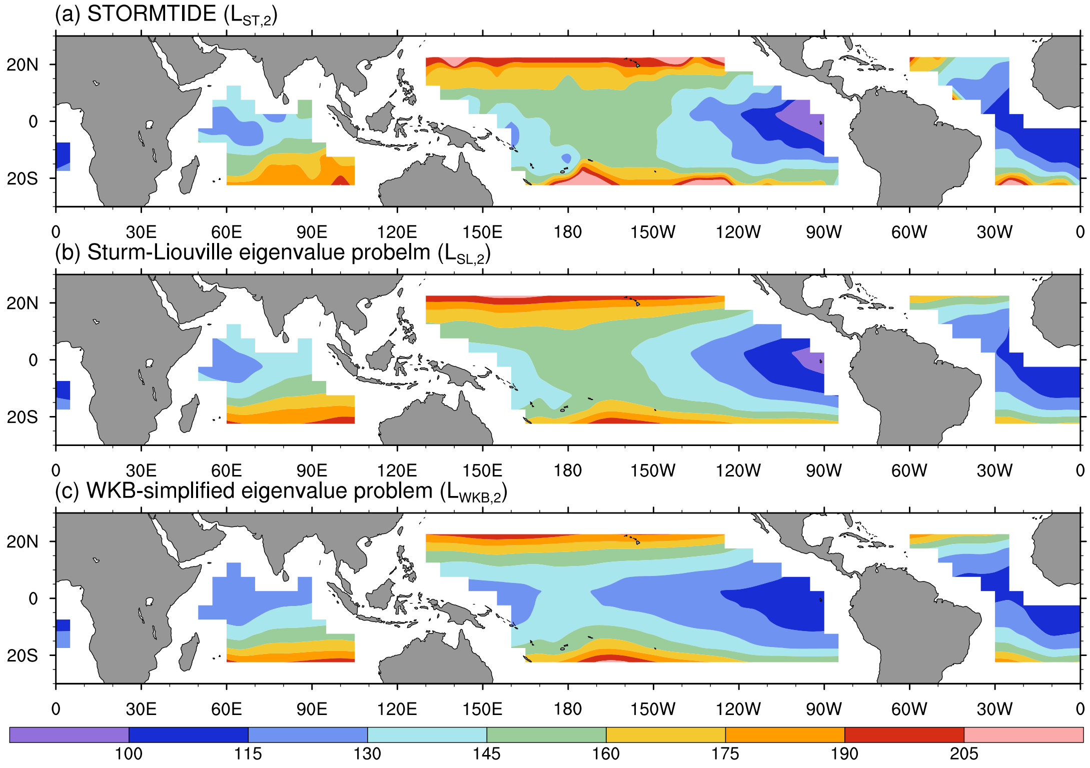
(a) STORMTIDE (L_{ST,2})
(b) Sturm-Liouville eigenvalue probelm (L_{SL,2})
(c) WKB-simplified eigenvalue problem (L_{WKB,2})
20N
0
20S
0
30E
60E
90E
120E
150E
180
150W
120W
90W
60W
30W
0
100
115
130
145
160
175
190
205

Figure 3.9: Mode-2 wavelengths (km) of the K_1 internal tide, derived by the same methods as described in Fig. 3.8. Instead of 100 m used for the simulated mode-1 wavelengths, (a) the simulated mode-2 wavelengths are derived at depths where the vertical modal structures of mode 2 undergo their respective interior maxima.

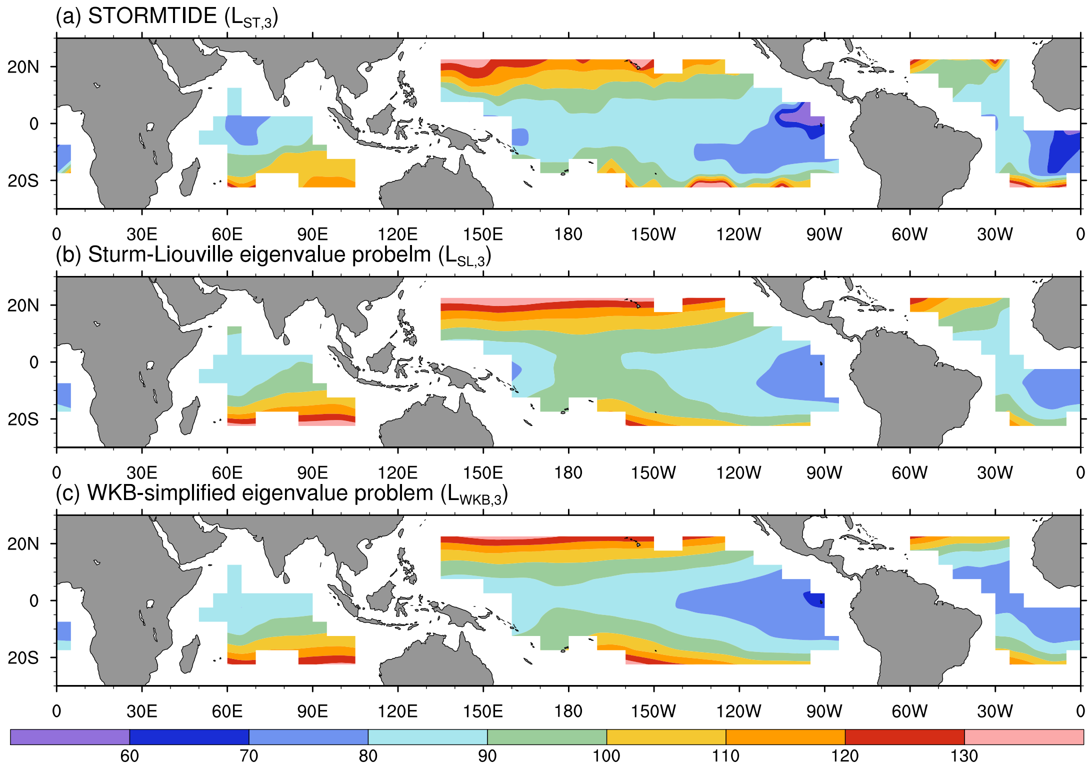
(a) STORMTIDE ($L_{ST,3}$)
(b) Sturm-Liouville eigenvalue probelm ($L_{SL,3}$)
(c) WKB-simplified eigenvalue problem ($L_{WKB,3}$)
20N
0
20S
0
30E
60E
90E
120E
150E
180
150W
120W
90W
60W
30W
0
60
70
80
90
100
110
120
130

Figure 3.10: Mode-3 wavelengths (km) of the K_1 internal tide, derived by the same methods as described in Fig. 3.8. Instead of 100 m used for the simulated mode-1 wavelengths, (a) the simulated mode-3 wavelengths are derived at depths where the vertical modal structures of mode 3 undergo their respective second (deeper) interior maxima.

3.3.3 Comparison with the distributions obtained by solving the eigenvalue problem

The spatial distributions of the simulated wavelengths $L_{ST,m}$ $(m = 1, 2, 3)$ show similar geographic patterns as those derived by solving the Sturm-Liouville eigenvalue problem $L_{SL,m}$, as can be seen by comparing Fig. 3.8a with 3.8b, 3.9a with 3.9b, 3.10a with 3.10b, respectively. The relative differences between $L_{ST,m}$ and $L_{SL,m}$ are shown in Fig. 3.11. In general, a small discrepancy, under 5%, is observed in about half of the considered regions or even more (specifically 54%, 67.5% and 48% for mode 1 to 3, respectively). The small discrepancy indicates a good agreement between the simulation and the eigenvalue problem, meaning that the simulated waves in these regions highly satisfy the dispersion relation diagnosed locally from linear wave theory. This good agreement is also reflected in the zonal-mean comparisons of $L_{ST,m}$ and $L_{SL,m}$ (left column of Fig. 3.12).

Furthermore, a discrepancy between 5%-15% covers certain considered regions. Discrepancies larger than 15% can also be observed, but show up only in very limited area (covering 4.6%, 6% and 12% of the considered region for mode 1 to 3, respectively), primarily in higher-latitude oceans. Large discrepancies ($>$ 15%) appear also in the eastern equatorial Pacific for mode 3. Differing from the first two modes though, the discrepancies between the $L_{ST,3}$ and $L_{SL,3}$ in Fig. 3.11c primarily show negative values, indicating shorter length scales of the simulated mode-3 K_1 internal tides compared to those derived from the eigenvalue problem. This feature is clearly reflected in the zonal-mean comparison in Fig. 3.12e.

To summarize, the simulated K_1 internal tides are, to the first approximation, linear internal waves that satisfy the local dispersion relation, with other effects accounting for less than 10% (5.9%, 5% and 7.5% for the global average of mode 1 to 3, respectively) of the relative discrepancies between $L_{ST,m}$ and $L_{SL,m}$.

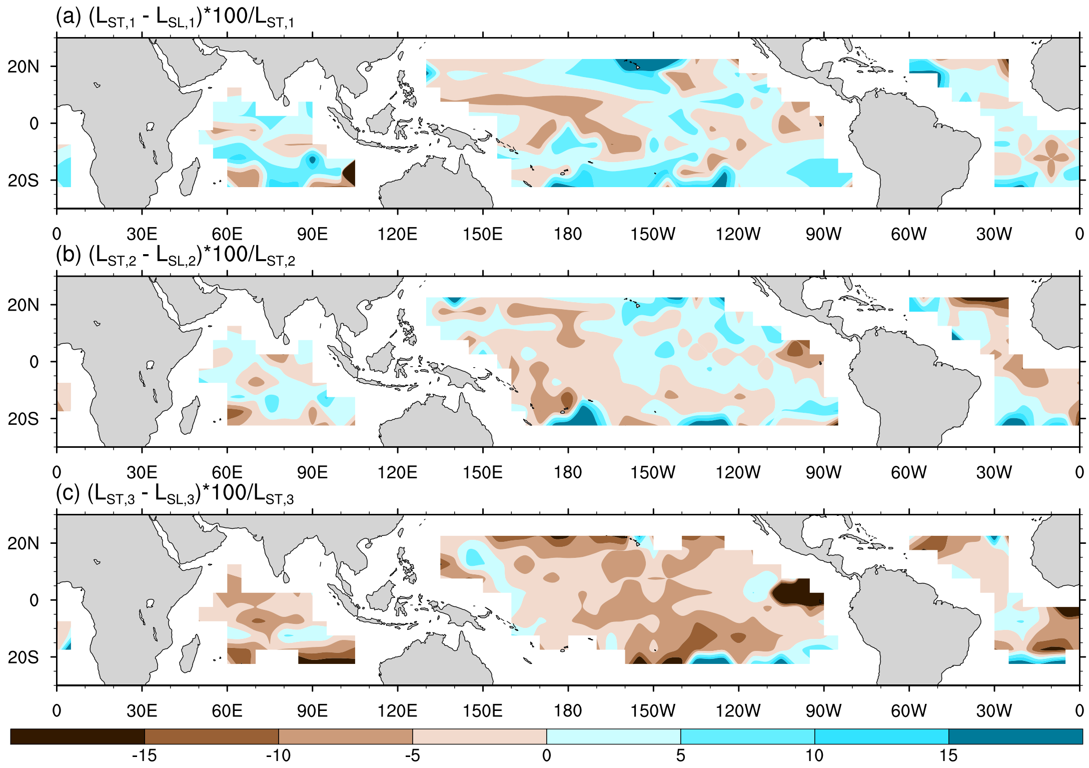
(a) (L$_{ST,1}$ - L$_{SL,1}$)*100/L$_{ST,1}$
(b) (L$_{ST,2}$ - L$_{SL,2}$)*100/L$_{ST,2}$
(c) (L$_{ST,3}$ - L$_{SL,3}$)*100/L$_{ST,3}$
20N
0
20S
0
30E
60E
90E
120E
150E
180
150W
120W
90W
60W
30W
0
-15
-10
-5
0
5
10
15

Figure 3.11: Relative discrepancies (%) between the simulated and theoretical wavelengths for (a) mode 1, (b) mode 2, and (c) mode 3, that is, $(L_{ST,m} - L_{SL,m}) \times 100/L_{ST,m}$, $m = 1, 2, 3$. Blue shading indicates that the values of $L_{ST,m}$ are larger than those of $L_{SL,m}$, whereas brown shading suggests the opposite.

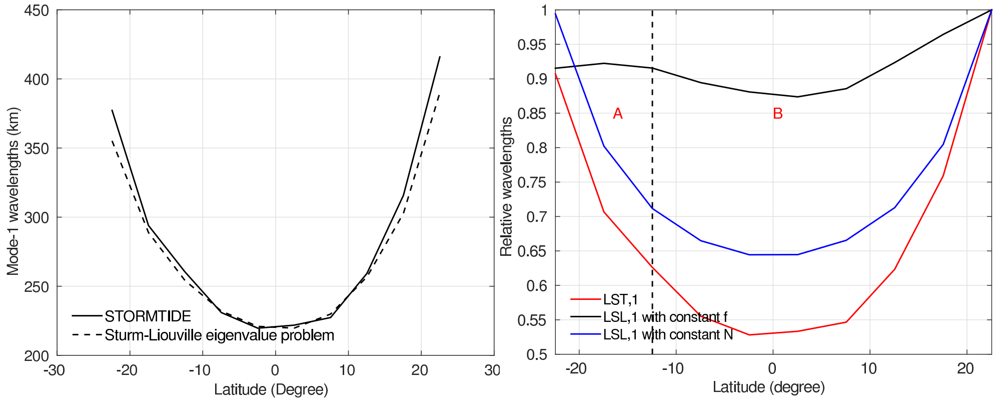
(a) Zonal-mean mode-1 wavelengths (b) Normalized mode-1 wavelengths

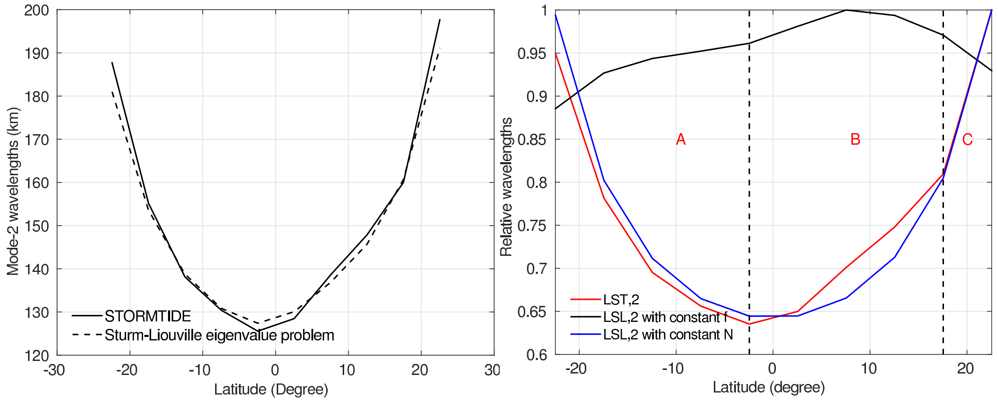
(c) Zonal-mean mode-2 wavelengths (d) Normalized mode-2 wavelengths

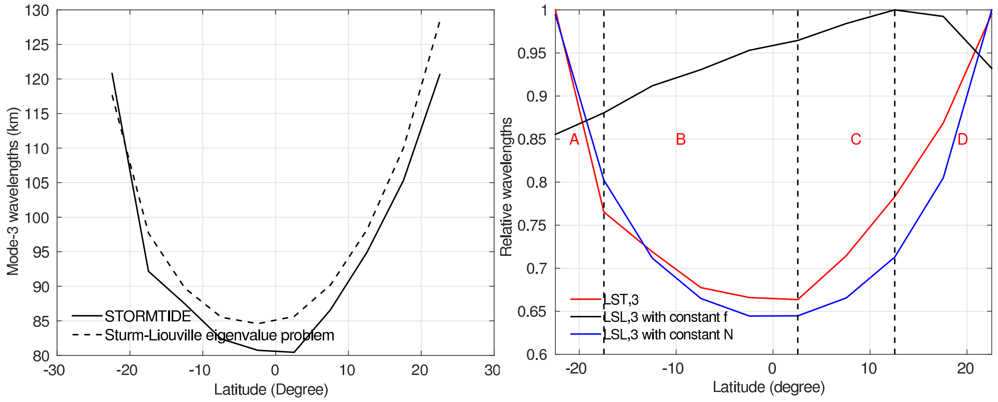
(e) Zonal-mean mode-3 wavelengths (f) Normalized mode-3 wavelengths

Figure 3.12: Zonal-mean wavelengths (km) of (a) mode 1, (c) mode 2, and (e) mode 3, derived from the model simulation (solid lines) and by solving the standard Sturm-Liouville eigenvalue problem (dashed lines). In the right column, comparisons of the normalized zonal-mean wavelengths of the simulation (red lines) with the ideal tests, for mode (b) 1, (d) 2 and (f) 3, by assigning constant N (blue lines) and f (black lines), respectively, when solving the standard Sturm-Liouville eigenvalue problem. These wavelengths are normalized by their respective maxima in order to bring them to a comparable range of 0-1.

3.3.4 Relative roles of N and f in determining the wavelengths

As described above, we find a good agreement between $L_{ST,m}$ and $L_{SL,m}$. Since only N and f are taken into account in the eigenvalue problem, we perform two ideal tests to separate their roles by assigning constant N (hence constant eigenvalues ν_m) and constant f, respectively, when solving the standard Sturm-Liouville eigenvalue problem [Eq. (2.7)]. The resulting wavelengths are then denoted as $L_{SL,m,N}$ (constant N assigned) and $L_{SL,m,f}$ (constant f assigned), respectively.

The normalized zonal-mean values of $L_{ST,m}$ (red lines), $L_{SL,m,N}$ (blue lines) and $L_{SL,m,f}$ (black lines) are shown in Fig. 3.12 (right column). Note that the results are independent of the absolute values of the constant N and f due to the normalization of the resulting wavelengths. The zonal-mean $L_{ST,1}$ in Fig. 3.12b agrees well with the variations of $L_{SL,1,N}$, in which solely the f-effect is taken into account. This agreement occurs not only for the poleward increase tendency, but also for the relative magnitude. The relatively large discrepancy between them appears, however, in the equatorial regions, where the values of f are quite small and N could instead impose a larger effect. The zonal-mean $L_{SL,1,f}$, with N at work only, tends to increase with increasing latitudes as well, but vary in a quite narrow range. The large discrepancies between $L_{SL,1,f}$ and $L_{ST,1}$ reveal the weaker role of N in determining the mode-1 K_1 internal tide wavelengths. The presence of N-effect in $L_{ST,1}$ influences, however, the slopes of $L_{ST,1}$ compared to $L_{SL,1,N}$. Both slopes are comparable between 12.45°S-22.45°S (region A) due to the flatness of $L_{SL,1,f}$. The slopes of $L_{ST,1}$ are, however, sharper than those of $L_{SL,1,N}$ between 12.45°S-22.55°N (region B), a result of the superposition of the effects of both N and f. Hence, it proves that N and f play a combined role in determining the mode-1 simulated K_1 wavelengths, with the f-effect being dominant.

The normalized zonal-mean comparisons are shown for mode 2 in Fig. 3.12d. In general, the agreement between $L_{ST,2}$ and $L_{SL,2,N}$ is much better than mode 1, indicating the predominant role of f in determining the mode-2 wavelengths. To be specific, the relative magnitudes of $L_{ST,2}$ and $L_{SL,2,N}$ are similar in the southern hemisphere (region A), with also a comparable slope during their poleward increase. The magnitudes of $L_{ST,2}$ and $L_{SL,2,N}$ agree well between 17.55°-22.55°N (region C), and depart equatorward of 17.55°N in the northern hemisphere (region B). The N-effect leads to the complicated variations of $L_{SL,2,f}$, namely a poleward decrease in the southern hemisphere, and a poleward increase until 7.55°N followed by a decrease in the northern hemisphere. The variations of $L_{SL,2,f}$ are small in magnitudes, but contribute to the relatively larger discrepancies between the slopes of $L_{ST,2}$ and $L_{SL,2,N}$ in region B, where N and f play the role simultaneously. Outside this region (region A and C), the effect of N is rather weak, and the dominant role of f is evident.

Fig. 3.12f shows the normalized zonal-mean comparisons of mode 3. The relative magnitudes of $L_{ST,3}$ agree well with that of $L_{SL,3,N}$, in particular in the southern hemisphere (region A and B), with a poleward increase of the wavelengths. The slopes of $L_{ST,3}$ and $L_{SL,3,N}$ present, however, slight discrepancies. The wavelengths $L_{SL,3,f}$ vary in a rather small range and show similar latitudinal variations as mode 2. In the southern hemisphere, $L_{SL,3,f}$ reduces monotonously with increasing latitudes, leading to a reduced slope of $L_{ST,3}$ compared to $L_{SL,3,N}$ between 17.45°S-2.55°N (region B), with an exception poleward of 17.45°S (region A). In the northern hemisphere, the poleward increase of $L_{SL,3,f}$ leads to steeper $L_{ST,3}$ between 2.55°-12.55°N (region C) and the poleward reduction of $L_{SL,3,f}$ further leads to milder slopes of $L_{ST,3}$ (region D), compared to those of $L_{SL,3,N}$. Hence, a combined role of N and f, with f being dominant, is observed for the mode-3 wavelengths.

In general, the normalized zonal-mean $L_{ST,m}$ consists with $L_{SL,m,N}$ much better than with $L_{SL,m,f}$, with $L_{SL,m,f}$ varying in a rather narrow range of the relative magnitudes. The poleward increase of $L_{ST,m}$ is determined primarily by the presence of f. Hence, the Coriolis frequency f plays the dominant role in determining the K_1 wavelengths for all three modes that are resolved in the STORMTIDE model. The role of N is less significant in determining $L_{ST,m}$, but its role in the slight adjustment of the slopes and magnitudes of $L_{ST,m}$ is visible.

3.4 Application of the WKB-simplified eigenvalue problem

In this section, the WKB approximation is further applied to the Sturm-Liouville eigenvalue problem, by which we assume a more rapid vertical change of the K$_1$ internal tide than stratification N. Hence, we take into account only the vertical integral of stratification $\widehat{N}$, but neglect its detailed variations [Eq. (2.9)]. As shown in Fig. 3.8-3.10, the wavelength distributions derived from the WKB-simplified eigenvalue problem ($L_{WKB,m}$) reveal not only the same basic geographic patterns.

For a better understanding of the application of the WKB approximation to the freely propagating K$_1$ internal tide, we investigate the relative discrepancies between $L_{SL,m}$ [Eq. (2.7)] and $L_{WKB,m}$ [Eq. (2.9)] in detail, which is derived by

$$\frac{L_{SL,m} - L_{WKB,m}}{L_{SL,m}} = 1 - \frac{\widehat{N}\sqrt{\nu_m}}{m\pi} \ , \tag{3.1}$$

where ν_m is the eigenvalues from the standard Sturm-Liouville eigenvalue problem. It suggests that the relative discrepancies are independent of the tidal frequency ω, and thus present the same distributions for the K$_1$ internal tide as those of the M$_2$ constituent (section 2.7).

The relative discrepancies are shown in Fig. 3.13. The dominant structures that are observed are the dominant negative values for mode 1 and positive values for mode 2 and 3, indicating the general overestimates for mode 1 and underestimates for modes 2 and 3 by applying the WKB approximation. Relative small discrepancies, under 10%, are observed in a large fraction of the considered ocean (80%, 88% and 92% for mode 1 to 3, respectively). There are discrepancies that are even smaller than 5% in the entire ocean basin, in the Atlantic for mode 2 and in the Indian Ocean for mode 3, where the WKB approximation is in general applicable. However, discrepancies larger than 10% also show up in certain regions, mainly in the eastern Pacific and the low-latitude Indian Ocean for mode 1, in the western equatorial Pacific for mode 2, and in the eastern equatorial Pacific and northern Atlantic for mode 3, respectively. In these regions, the WKB approximation would cause large errors in quantitative calculations. To accurately capture the K$_1$ internal tide wavelengths, not only the precise vertical integral, but also the detailed variations of stratification are thus required.

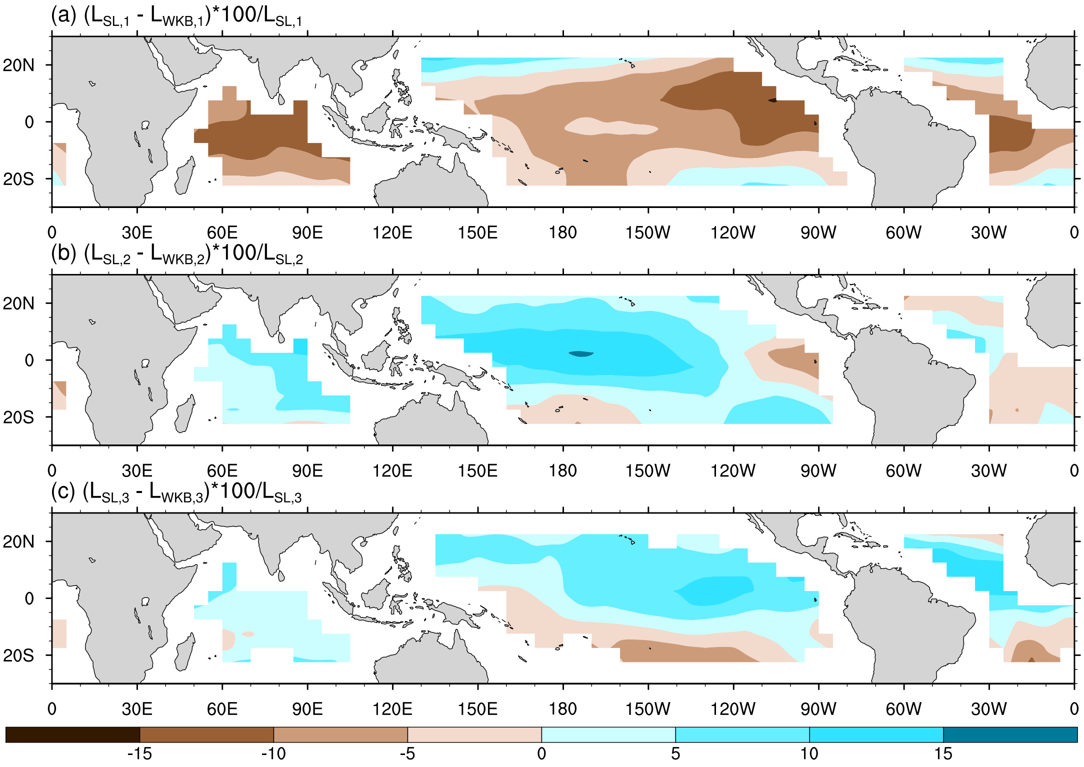
(a) (L_SL,1 - L_WKB,1)*100/L_SL,1
(b) (L_SL,2 - L_WKB,2)*100/L_SL,2
(c) (L_SL,3 - L_WKB,3)*100/L_SL,3
20N
0
20S
0
30E
60E
90E
120E
150E
180
150W
120W
90W
60W
30W
0
-15
-10
-5
0
5
10
15

Figure 3.13: Relative discrepancies (%) between $L_{SL,m}$ and $L_{WKB,m}$ for mode (a) 1, (b) 2, and (c) 3, respectively, that is, $(L_{SL,m} - L_{WKB,m}) \times 100/L_{SL,m}$, $m = 1, 2, 3$. Blue shading indicates that the values of $L_{SL,m}$ are larger than those of $L_{WKB,m}$, whereas brown shading suggests the opposite.

3.5 Role of the critical latitude

3.5.1 Kinetic energy section of the propagating K_1 internal tide

A vertical section of the simulated kinetic energy of the K_1 internal tide is shown in Fig. 3.14a along 20.05°N. The energy is found to be primarily concentrated in the upper ocean, while there is only a low energy level in the deeper ocean, a feature observed also for the simulated M_2 internal tide (Fig. 2.4a).

To understand the surface-concentrated energy, we take into account the propagation of internal tides. Internal tides emitted from a localized source normally propagate as beams (Mowbray and Rarity 1967; Turner 1973) both vertically and horizontally in the continuously stratified ocean. The energy trajectories are typically calculated by the ray theory (e.g., Kunze 1985; Broutman et al. 2004; Rainville and Pinkel 2006; Chavanne et al. 2010), with ray paths emanating from the locations of critical slopes on the ridge flanks (e.g., Pairaud et al. 2010). In our results, the beam-like structures are partially recognizable as highlighted (black lines) in Fig. 3.14a. The beams are found to be bended and steeper in the abyssal than upper ocean, an effect of refraction occurring in a varying medium (e.g., Gerkema and Zimmerman 2008). This is consistent with the results of linear wave theory, which predicts that beams propagate more vertically in the abyssal ocean with weaker N, while they tend to propagate more horizontally with strong N in the upper ocean. Based on linear wave theory, refraction of upward-propagating internal tides would focus the energy (Mathur and Peacock 2009), leading to narrower wave beams in the upper ocean than in the deeper ocean, hence resulting in a surface concentration of energy. However, this single process is not isolated in our result. Furthermore, the upward-propagating beams are partially trapped within the pycnocline, experiencing further reflection within the pycnocline with energy confined in a narrow upper band (Mathur and Peacock 2009). Small-scale variations in N (smaller than a vertical wavelength of the beams) also scatter wave beams, significantly distorting the wave beams, weakening the reflected beams and creating a second site of surface activity (Martin et al. 2006; Mathur and Peacock 2009). All these processes are potential contributors for the surface concentration of the kinetic energy. Further studies would be required to separate their relative importances.

On the other hand, the beams are mainly observed evidently in the immediate vicinity of topographic features (Fig. 3.14a). It is known that the superposition of various vertical modes forms the beams (e.g., Gerkema and Zimmerman 2008). Low modes can radiate long distances from their generation sites (e.g., Ray and Mitchum 1996), while high modes exist primarily near topography features because of their greater shear and slower propagation speeds (e.g., Pickering and Alford 2012). Hence, in the

(a) Kinetic energy

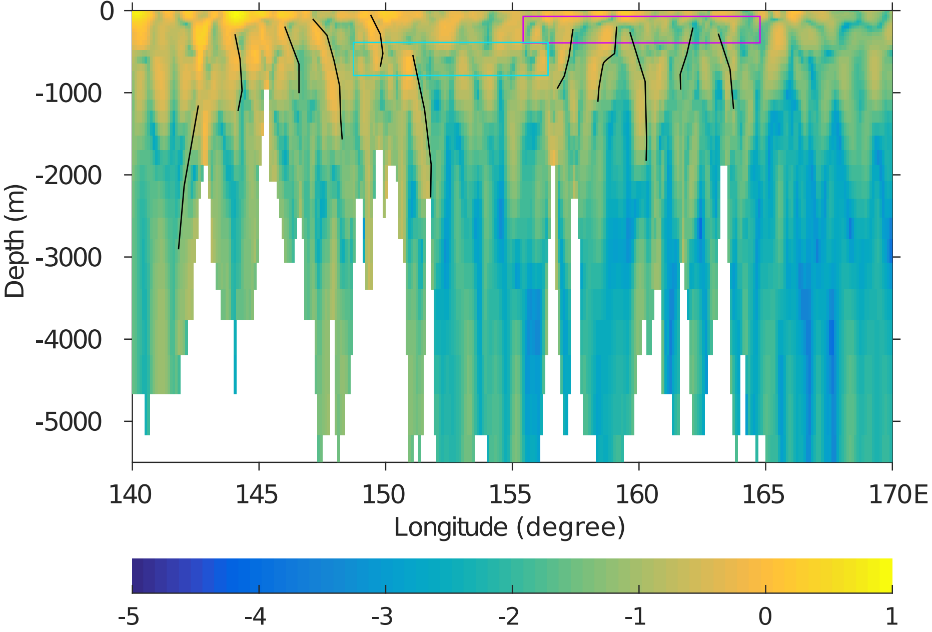

(b) Stratification

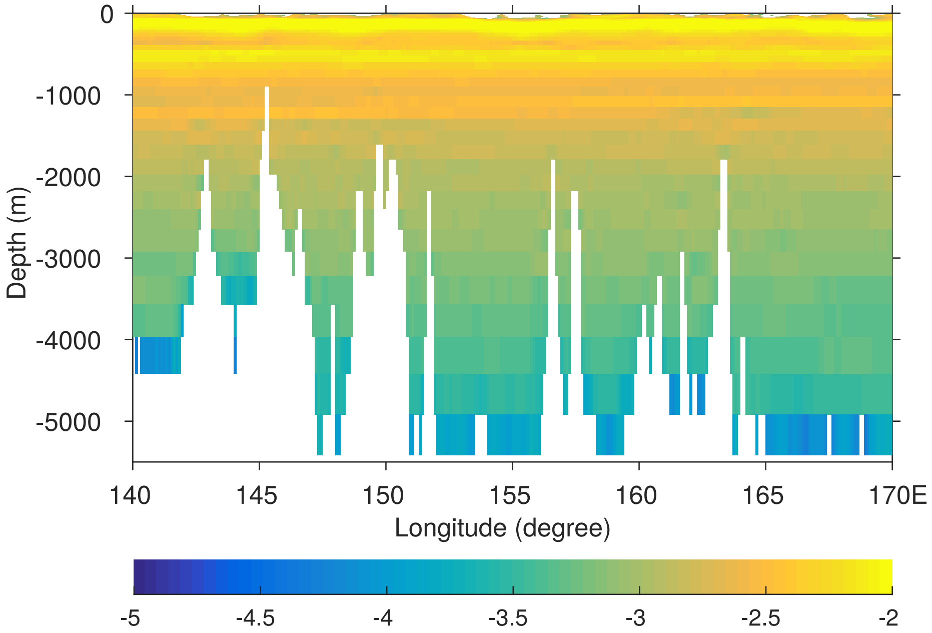

Figure 3.14: Vertical distributions of (a) the K_1 kinetic energy (J m^{-3}) in logarithmic scale, and (b) stratification (s^{-1}) over the section along (140°-170°E, 20.05°N) in the northern Pacific. Both plots are derived at the regular lonlat grid, i.e., 0.1° × 0.1°, which are converted from the non-regular model resolution. In (a), the black lines indicate internal wave beams (manually drawn for demonstration), and the two boxes indicate the regional breakups of wave beams.

far field of the generation site, only low modes are at work, as shown in Fig. 3.15, for the dominant mode 1 (blue line) and a superposition of modes 1 and 2 (red line).

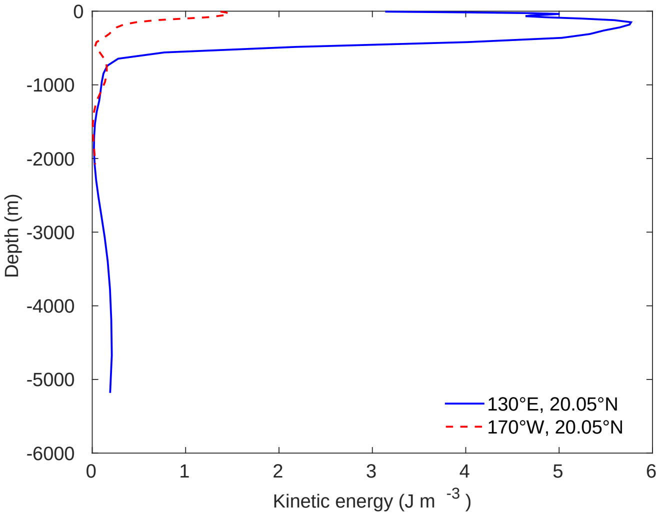

Figure 3.15: Vertical profiles of the K_1 kinetic energy at single points, located at (130°E, 20.05°N) (blue) and at (170°W, 20.05°N) (red), derived at the regular lonlat grid with a resolution of 0.1° × 0.1°.

As has been pointed out by Gerkema and van Haren (2012), introducing vertical variations of N breaks up the well-defined beams in uniform N near the pycnocline. The beams are turned into patches when further taking into account the horizontal variations of N. The observed regional breakups in the upper ocean, for instance, between 150°-165°E (highlighted by the magenta and blue boxes in Fig. 3.14a), can be, at least partially, attributed to the presence of the pycnocline (Fig. 3.14b).

When upward-propagating beams impinge on thermoclines or ocean surface, many processes occur. In the reflection zone at the surface where incident and reflected beams intersect, nonlinear effects are strong and drag energy out of the wave beams, producing a mean flow and higher harmonics (Gerkema et al. 2006; Pairaud et al. 2010). Solitary internal waves can also be excited when the wave beams impinging on the pycnocline (Akylas et al. 2007). The beams can also undergo internal reflection (e.g., Gerkema and van Haren 2012), or lead to trapped waves in the boundary layer due to the reflection (Mathur and Peacock 2009). All these processes contribute to a complicated structure of the kinetic energy distributions, deviating severely from the well-established beams from the generation sites. More investigations are thus required to fully understand the propagation of internal tide beams in the realistic ocean.

3.5.2 Kinetic energy section of the trapped K_1 internal tide

The simulated K_1 kinetic energy poleward of the critical latitude is shown in Fig. 3.16 at (160°E, 52.05°N). The energy level in Fig. 3.16 is significantly lower and reveals a different vertical distribution than those in Fig. 3.15. The kinetic energy is found to be amplified at the bottom, with a rapid upward decrease. Hence, the surface energy is lower, exhibiting relatively weak variations. This bottom amplification of the kinetic energy is associated with bottom-trapped internal tides (Falahat and Nycander 2015), a feature well represented in the vertical section along 52.05°N in Fig. 3.17a. Energetic motions are observed over rough topography, for instance, at around 160°E and 174°E directly over the seamounts, where strong internal tides are created by barotropic tidal currents flowing over sloping topography. Since these internal tides cannot propagate away from the generation site in supercritical latitudes due to the constraint of f, they are locally confined, with strong tidal current velocities of the K_1 internal tide observed in the vicinity of rough topography. The K_1 tidal currents are, however, largely weakened in the ocean's interior. Further, no beams are observed in the neighbouring of the seamounts in the absence of wave propagations.

The Southern Ocean is found to contain strong kinetic energy as described in section 3.2. Fig. 3.18a shows the vertical distributions of the K_1 kinetic energy along 52.02°S in the Southern Ocean. The bottom amplification of the kinetic energy is present, since it is located at the supercritical latitudes. However, a high energy level shows up also in the surface layers, different from our finding shown in Fig. 3.16a. The vertical distributions of N are more complex in this given section in the southern hemisphere (Fig. 3.18b) than in the northern hemisphere (Fig. 3.17b), attributed to the strong currents and rich eddies in this region. Hence, the resulting strong nonlinear interactions with internal tides might be responsible for bringing the bottom energy

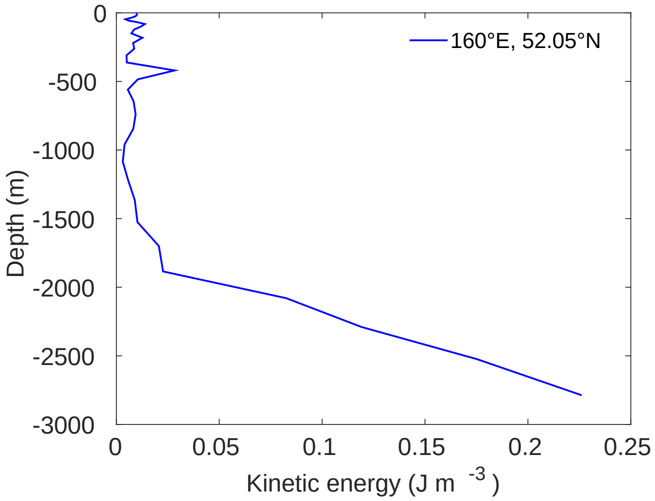

Figure 3.16: Vertical distribution of the K$_1$ kinetic energy (J m^{-3}) at (160°E, 52.05°N).

upward and account for the regional hot spots of surface-concentrated energy.

3.5.3 Bottom energy distributions of the K$_1$ internal tide

To know how the trapping process is simulated by the model, we investigate the vertical energy distributions of the K$_1$ internal tide above the ocean bottom. In this calculation, we interpolate, within the horizontal plane, the amplitudes of the zonal (u_{bc}) and meridional (v_{bc}) K$_1$ baroclinic velocities, defined on the edges of the grid cells, onto the scalar points that are defined on the centers of the grid cells, whose water depths are used as a reference. The vertical resolution is inhomogeneous in the model. The layer thickness is in the range of 10-60 m in the upper 500 m, and ranges within 100-500 m below 700 m, shown in Fig. 3.19 with the y-axis being the averaged depths of every two neighbouring model layers. It is obvious that the resolution is much coarser in the deeper than upper ocean. In order to smoothen the profiles of the energy distribution close to the ocean bottom, the model data have been interpolated to a vertically uniform 100 m resolution grid. The energy is also obtained at 50 m above the bottom at shallow waters in order to take advantage of the higher resolution.

The vertical distributions of the K$_1$ kinetic energy above the bottom for regions

(a) Kinetic energy

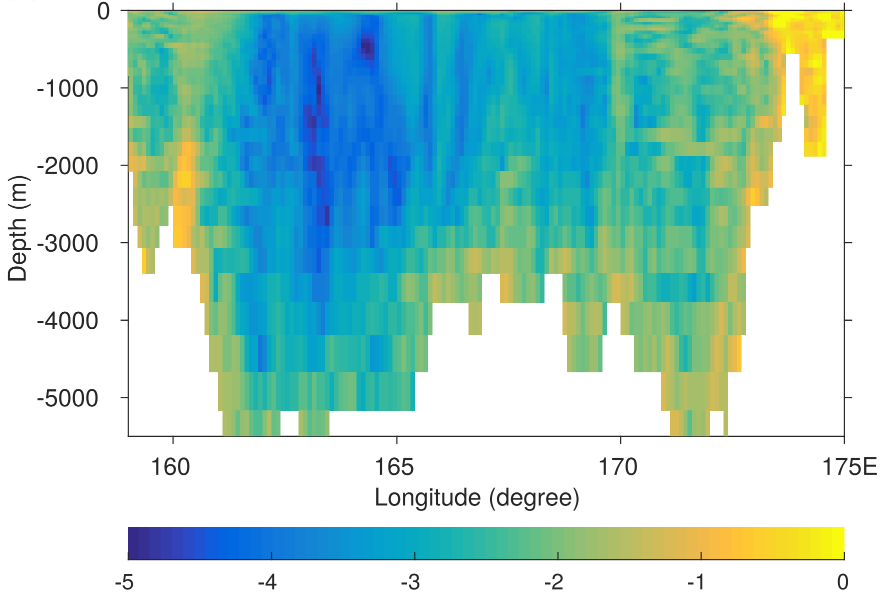

(b) Stratification

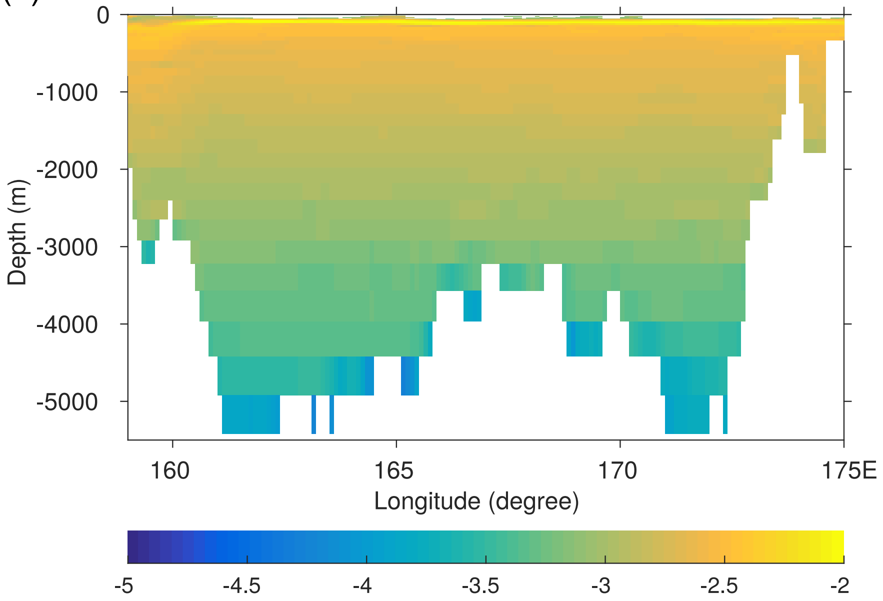

Figure 3.17: Vertical distributions of (a) the K_1 kinetic energy (J m^{-3}) in logarithmic scale and (b) stratification (s^{-1}) for a section between 159°-175°E along 52.05°N in the northern Pacific. This section is located at poleward of the K_1 critical latitude ($\varphi_c = 30°$), and both distributions are derived from the distributions at the regular lonlat grid with a resolution of $0.1° \times 0.1°$.

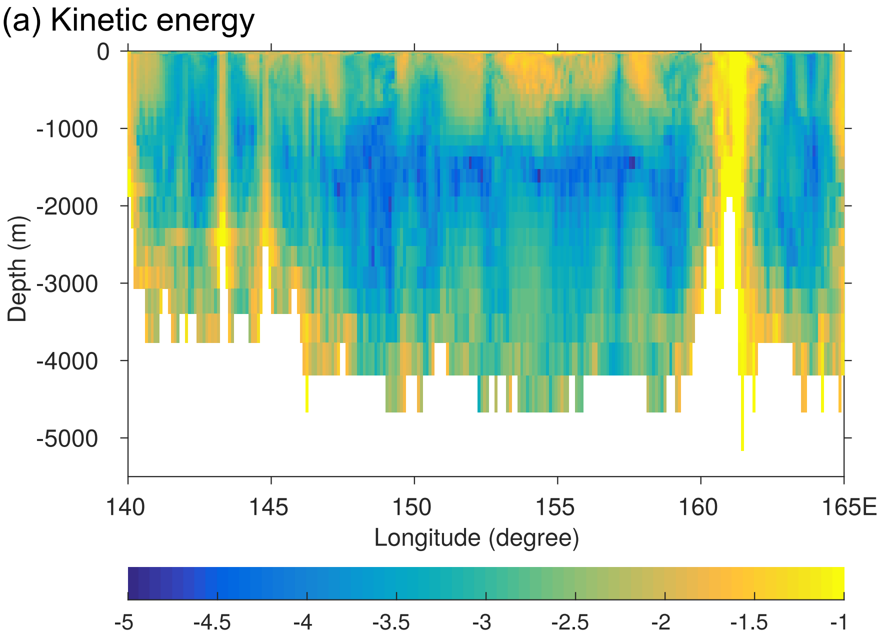

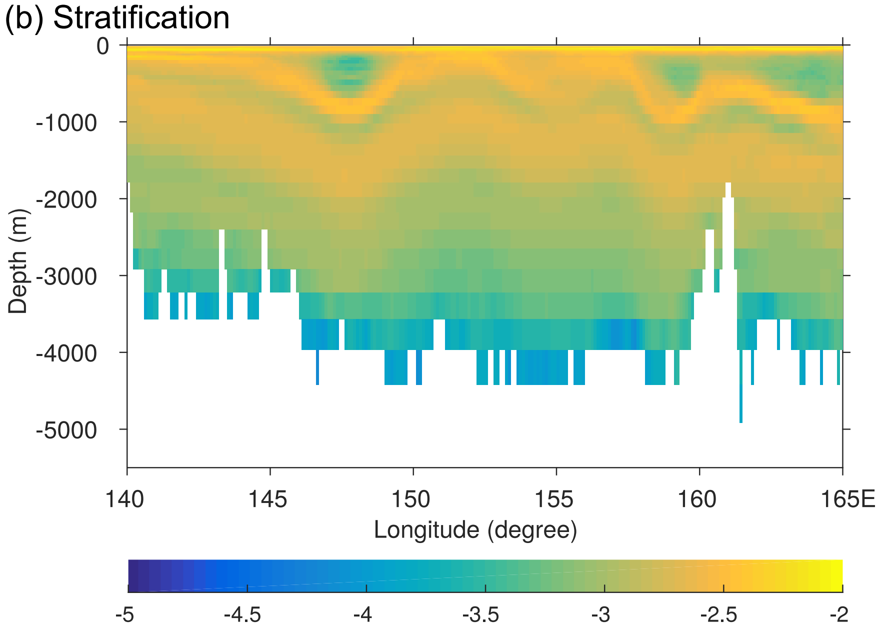

Figure 3.18: Vertical distributions of (a) the kinetic energy (J m^{-3}) in logarithmic scale and (b) stratification (s^{-1}) between 140°-165°E along 52.05°S in the Southern Ocean poleward of the K_1 critical latitude.

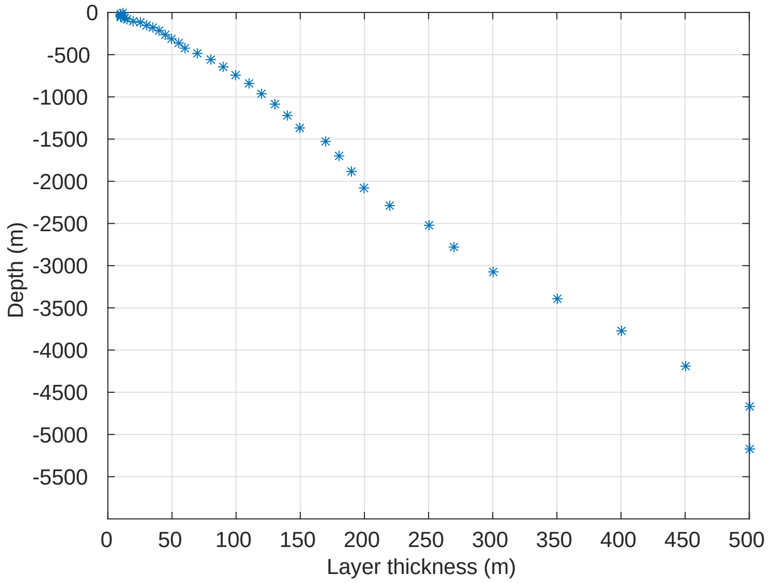

Figure 3.19: Layer thickness (m) of the STORMTDIE model. Y-axis shows the averaged depths of every two neighbouring model layers.

equatorward of 30° are shown in Fig. 3.20a for waters shallower than 2500 m and in Fig. 3.20b for water depths below 2500 m. The energy distributions are shown for different water-depth intervals separated by 500 meters. In general, the baroclinic tidal kinetic energy density is largest in shallow waters (water depth H <550 m). With larger water depths, energy is distributed over a large water column and thus reduces. The energy is found to increase upward from the bottom until a certain depth. This characteristics is more pronounced in shallower than in deeper waters. This upward increase is a feature of freely propagating internal tides with energy concentrated in the upper ocean as described before. Note that due to the coarser resolution in deeper waters, results are most reliable in shallower waters.

Even when the tidal frequency is larger than f, tides can still be trapped at the coastal regions when certain criteria are satisfied (e.g., Rhines 1970). In our results (Fig. 3.20a), an initial upward slight decrease of the kinetic energy is observed from 50 m to 100 m above the very bottom in waters shallower than 550 m (bottom two dots of the blue line in Fig. 3.20a), which could be attributed to the coastal trapped internal tides.

The vertical energy distributions above the bottom poleward of 30° are displayed in Fig. 3.21a and 3.21b for waters shallower and deeper than 2500 m, respectively, for the K_1 internal tide. Again, the kinetic energy appears to be strong in shallow waters, yet strongest in waters shallower than 550 m, followed by a gradual reduction in the energy level from the shallow to deep waters. The energy in deeper waters (Fig. 3.21b) turns out to be much lower than that in shallower waters (Fig. 3.21a). Focusing on a specific water depth interval (along a single line), the kinetic energy is found to reduce from the bottom upward until a certain depth, a typical feature of bottom-trapped internal tides. This feature is better visualized in Fig. 3.22, in which the kinetic energy is normalized by their respective maximum, primarily located at the bottom, except for the case of water depths within 4000-4500 m.

Distinct decreasing rates are observed in Fig. 3.21 and Fig. 3.22, revealing a faster reduction of the energy in shallow than deep oceans. The strongest energy reduction occurs in waters shallower than 550 m, reducing to 50% within around 200 m above the bottom. To obtain the same reduction (about 50%), we need, however, go up to 270 m, and even to 500 m, above the bottom for water-depth intervals within 550-1000 m and 1000-1500 m, respectively. A larger distance from the bottom is further required for even deeper waters to obtain 50% energy reduction.

As clearly shown in Fig. 3.21a, there is a further intensification of energy above the level of energy minimum (at 200 m of the blue line) for shallow waters, which is even visible for waters of intermediate depth (1000-1500 m). This could be related to the near-surface intensification of energy as shown in Fig. 3.18a for the bottom-trapped K_1 internal tides. However, a comprehensive understanding would require further analysis.

3.6 Concluding remarks

In this study, we quantify the characteristics of the low-mode K_1 internal tide by using the 1/10° STORMTIDE simulation, in which the eddying circulation and tides

(a) Bottom kinetic energy at waters shallower than 2500 m

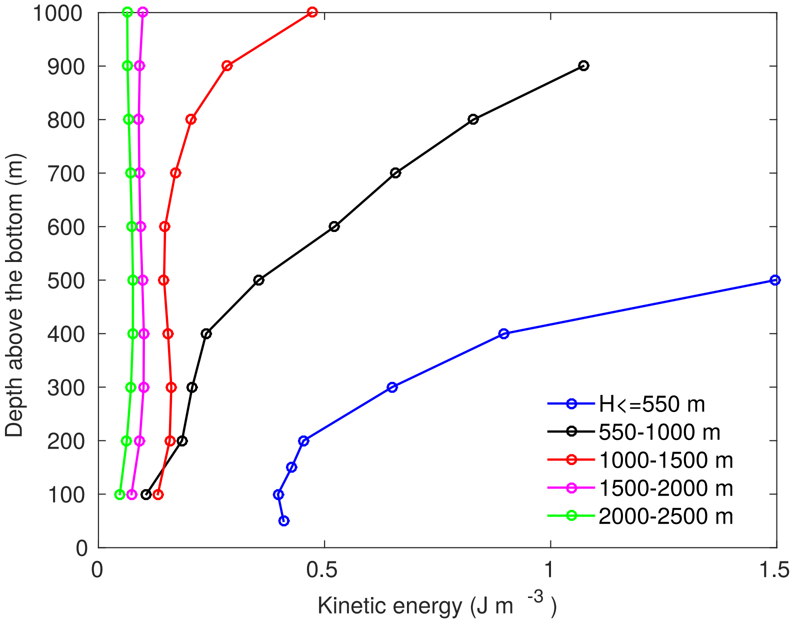

(b) Bottom kinetic energy at waters within 2500-5500 m

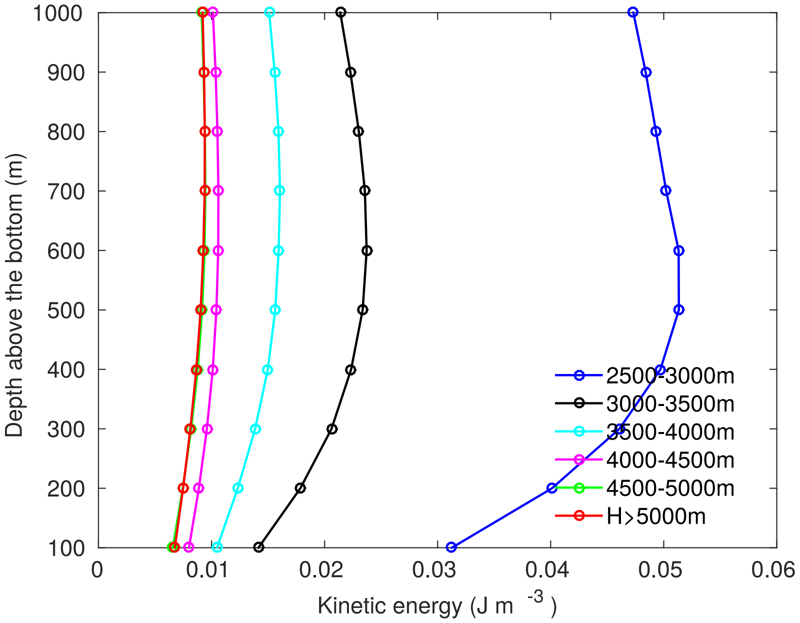

Figure 3.20: Kinetic energy (J m^{-3}) of the K$_1$ internal tide above the bottom, divided by different water depths equatorward of the K$_1$ critical latitude at 30° for (a) shallower waters (H < 2500 m) and (b) deeper waters (H > 2500 m). In general, 500 m interval is employed in the separation of regions. Note the different scales of the x-axis in both plots.

(a) Bottom kinetic energy at waters shallower than 2500 m

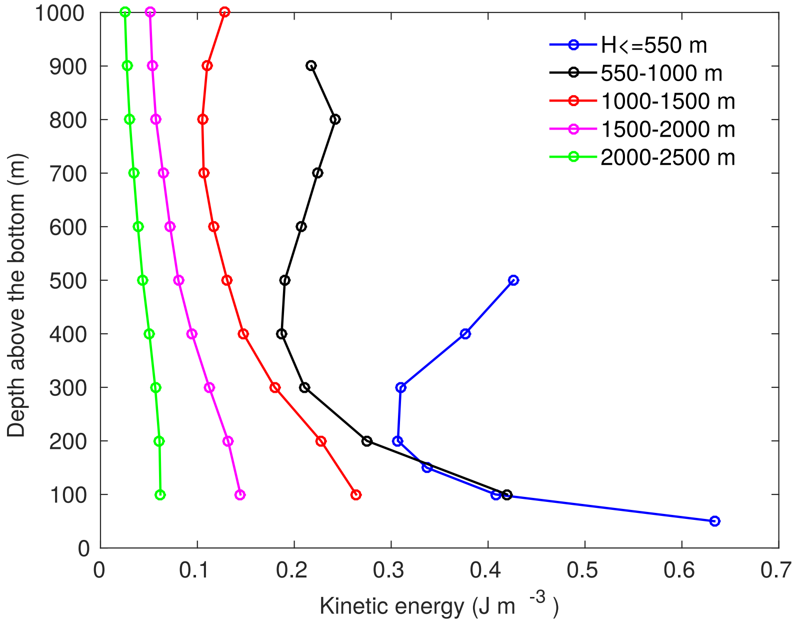

(b) Bottom kinetic energy at waters within 2500-5500 m

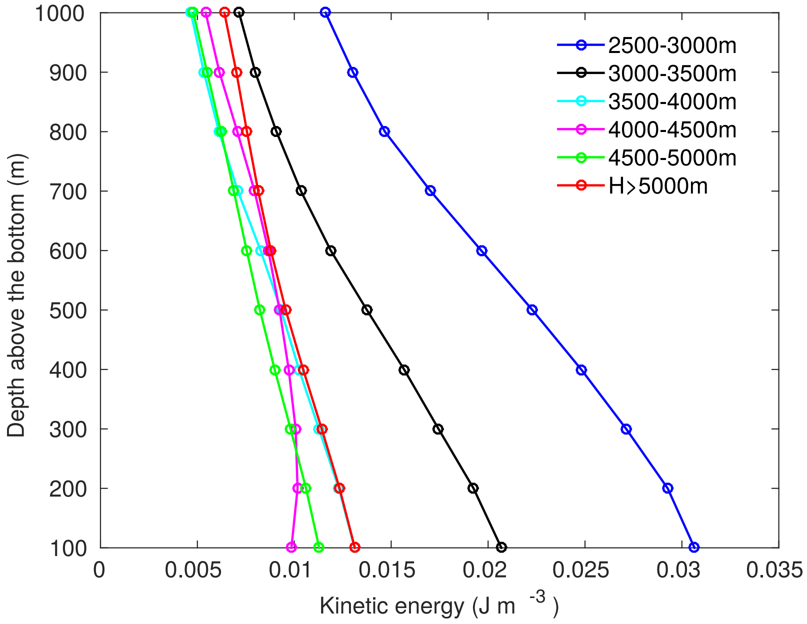

Figure 3.21: The same as Fig. 3.20, but derived in regions poleward of the K_1 critical latitude at 30°.

(a) Bottom kinetic energy at waters shallower than 2500 m

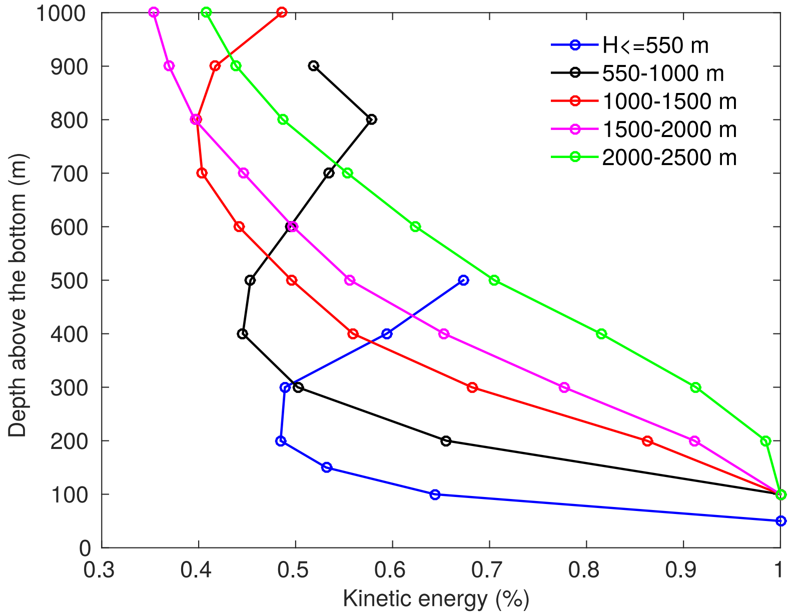

(b) Bottom kinetic energy at waters within 2500-5500 m

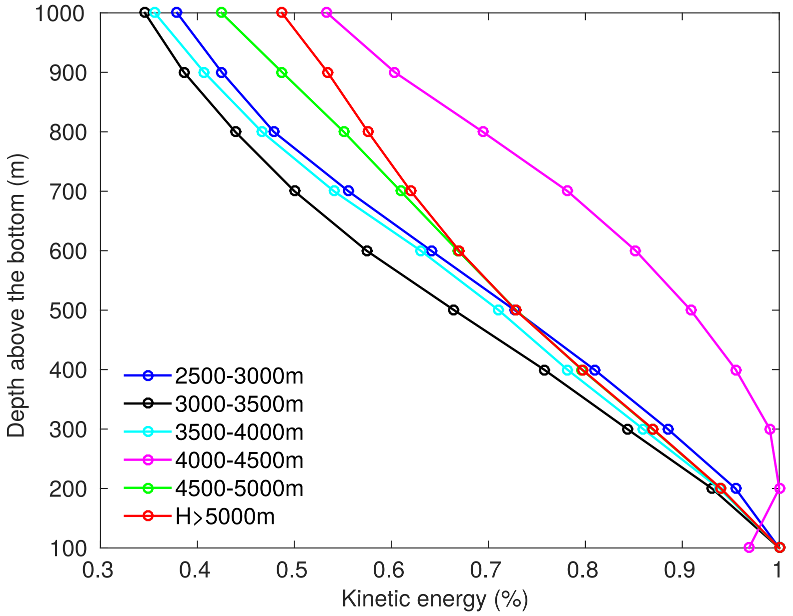

Figure 3.22: Normalized kinetic energy (%) above the bottom, divided by different water depths, and normalized by their respective maximum in each water depth interval poleward of the K_1 critical latitude 30° for (a) shallower waters ($H < 2500$ m) and (b) deeper waters ($H > 2500$ m). In general, 500 m interval is employed in the separation of regions.

are simultaneously simulated. The two-dimensional wavenumber spectral analysis is applied to the simulated baroclinic tidal velocities, which guides us into the characteristics of the wavenumber spectra, the wavelengths and their geographical distributions. By comparing these results with those of the standard and the WKB-simplified Sturm-Liouville eigenvalue problems, we analyze to what extent does the simulated K_1 internal tide satisfy the dispersion relation, and the relative roles of stratification N and the Coriolis frequency f in determining the distributions of the K_1 wavelengths.

The presence of the critical latitude (at 30° for the K_1 tides) in this high-resolution simulation enables us to study and compare the characteristics of baroclinic tidal energy above the bottom both poleward and equatorward of the critical latitude. In general, the following main conclusions are drawn in our study.

1. Three to four modes are captured in this 1/10° STORMTIDE simulation. The wavelength maps of the first three modes are provided in our study and commonly reveal a zonal asymmetry and a poleward increase of the simulated wavelengths, features that are more pronounced in the Pacific than in the other two basins. The wavelengths range in general within 200-400 km, 100-200 km, and 60-120 km for mode 1 to 3, respectively.

2. In around half of the considered ocean, the relative discrepancies between $L_{ST,m}$ and $L_{SL,m}$ are under 5%. The discrepancies, larger than 15%, occur in about 4.6%, 6%, and 12% of the considered ocean for mode 1 to 3, respectively. Hence, in most of the ocean, the simulated low-mode K_1 internal tides are, to the first approximation, linear waves that satisfy the local dispersion relation. A combined role of N and f is observed in determining the wavelengths of the first three modes, with f being dominant.

3. The relative discrepancies between $L_{SL,m}$ and $L_{WKB,m}$ are smaller than 15% for all three modes. We observe very small discrepancies ($< 5\%$) in the Atlantic for mode 2 and in the Indian Ocean for mode 3, where the WKB approximation would be well applied. Larger discrepancies ($> 10\%$) are also found in 20%, 12% and 8% of the considered region for the first three modes, respectively, where the WKB approximation would be problematic for a quantitative usage.

4. The STORMTIDE model is capable of capturing the different characteristics of the

kinetic energy of the K_1 internal tide, which are the surface concentration in subcritical latitudes and the bottom amplification in supercritical latitudes. Stratification N is found to play an important role in determining these vertical energy distributions. The kinetic energy is stronger in shallower than in deeper ocean regions, both equatorward and poleward of 30°. Furthermore, in shallow waters, we observe a strong decreasing rate of the bottom-amplified K_1 kinetic energy in supercritical latitudes, with an upward intensification above the level of the energy minima. The decreasing rate is, however, rather weak in deep waters.

The vertical model resolutions are rather coarse near the bottom in the open ocean. It leads uncertainties in our calculations of the vertical energy distributions above the bottom. However, due to a lack of global observations with a high vertical resolution directly above the bottom, this high-resolution simulation with 40 vertical layers is currently our only source of information. It also indicates the necessity of a higher vertical resolution in the model simulation, which also aids in a better understanding of the intensification of the K_1 baroclinic tidal energy above the depth of the energy minimum for shallow waters in supercritical latitudes.

Chapter 4

Concluding remarks and outlook

4.1 Concluding remarks

In this thesis, we analyze the tidal velocities that are simulated by the global high-resolution STORMTIDE model with a 1/10° horizontal resolution, in which the eddying general circulation, barotropic and internal tides are simultaneously simulated. The concurrent simulation is advanced, and to our knowledge, only two model groups have published such global concurrent simulations. This high-resolution simulation enables us to consider the three-dimensional currents globally. The only other global source of information is from satellite altimeter data, which, however, provide only the internal tide signatures at the sea surface with all modes integrated.

The tidal velocities—amplitudes and phases of the M_2 and K_1 constituents—are derived by performing the harmonic analysis with the full velocities of the model output. Subtracting the vertically integrated tidal velocities (barotropic) provides us the baroclinic tidal velocities over the 40 model layers. We present the magnitudes and geographical distributions of the horizontal baroclinic tidal kinetic energy in the upper (100 m) and deep (1085 m) ocean, as well as for the vertical integral. These distributions exhibit consistent hot spots of the internal tide generation with other studies. The baroclinic tidal energy is much stronger in the upper ocean than in the deep ocean for both tidal constituents. The kinetic energy of the K_1 internal tide clearly reveals the presence of its critical latitude at 30°N/S.

The baroclinic tidal velocities are further employed by using the two-dimensional wavenumber spectral analysis. The resulting two-dimensional wavenumber spectra $S_{KE}(k,l)$ of the kinetic energy, with k and l being the zonal and meridional wavenumbers, respectively, are displayed in a manner of energetic circles ($\sqrt{k^2+l^2} \approx$ constant). It means that the energy is concentrated at certain isotropic wavenumbers, an isotropy with respect to the amplitudes of the wavenumber vector. However, the spectra $S_{KE}(k,l)$ show strong anisotropy with respect to the directions of the wavenumber vector, and thus present us the preference of the wave propagation in each $15°/cos\varphi$ (in longitude) ×15° (in latitude) box, which is closely related to the topography and varies in space.

We summarize our main findings in the following.

1. **Which modes of the M_2 ad K_1 internal tides are simulated in the STORMTIDE model?**

The depth-dependence of each spectral peak of the one-dimensional kinetic energy spectra $S_{KE}(K)$, converted from $S_{KE}(k,l)$ using the horizontal wavenumber $K = \sqrt{k^2+l^2}$, is consistent with the vertical modal structures derived by solving the standard Sturm-Liouville eigenvalue problem with the simulated box-averaged stratification N. Hence, by performing the wavenumber spectral analysis, we capture actually the low-mode internal tides, two modes for the M_2 internal tide and three modes for the K_1 internal tide.

2. **What are the properties of the simulated internal tides, for instance, their wavelengths and the respective geographical distributions?**

By diagnosing the spectral peaks from $S_{KE}(K)$, the corresponding peak wavenumbers lead to the ultimate wavelengths. We perform the spectral analysis at fixed levels, i.e., 100 m and 1085 m, for deriving the mode 1 and mode 2 M_2 wavelengths. whose general ranges are within 100-160 km and 45-80 km, respectively.

More modes are resolved for the K_1 internal tide, which cause a more complicated vertical modal structure. Hence, we apply varying depth in space for the acquisition of the K_1 internal tide wavelengths of each mode, at 100 m for mode 1, at depths where mode 2 undergoes its interior maximum for mode 2, and at depths where mode 3 experiences its second (deeper) interior maximum for mode 3. The K_1 wavelengths of the first three modes range within 200-400 km, 100-200 km, and 60-120 km, respectively. Apparently, the K_1 internal tide exhibits a larger length scale than the M_2 internal tide at the same vertical mode, consistent with the large timescale of the K_1 internal tide.

The largest magnitudes and strongest spatial variations of the wavelengths are found in the Pacific for both the M_2 and K_1 internal tides; in general, wavelengths are larger in the western than in the eastern Pacific. There is an evident zonal asymmetry for both modes of the M_2 constituent, but a general poleward increase of the wavelength with increasing latitudes is much more pronounced for mode 1 than for mode 2. Both features are clearly observed for mode 1 to 3 of the K_1 internal tide.

3. **How are the simulated low modes consistent with the dispersion relation of linear internal waves?**

We compare the magnitudes and geographical distributions of the simulated M_2 and K_1 wavelengths ($L_{ST,m}$ with m being mode number) with those derived from the standard Sturm-Liouville eigenvalue problem ($L_{SL,m}$) with the simulated box-averaged N applied. The relative discrepancies between $L_{ST,m}$ and $L_{SL,m}$ are under 5% in around two thirds and one half of the considered ocean for the M_2 and K_1 internal tides, respectively. Discrepancies larger than 15% appear only in very limited regions. Hence, the simulated internal tides are, to a first approximation, linear internal waves that satisfy the local dispersion relation, with other effects accounting for less than 10% in terms of the relative discrepancies.

4. **What are the relative roles of local stratification N and the Coriolis parameter f in determining these geographical distributions?**

The standard Sturm-Liouville eigenvalue problem depends only on N and f. Hence, the zonal asymmetry and the poleward increase with increasing latitudes, observed in both $L_{ST,m}$ and $L_{SL,m}$, are attributed to the effect of N and f, respectively.

Ideal tests are set up in order to investigate the relative roles of N and f, by correspondingly assuming constant f and N in the Sturm-Liouville eigenvalue problem. The tests are separately carried out for the M_2 and K_1 internal tides. A combined role of N and f is observed in determining the wavelengths of the mode-1 M_2 internal tide, while N seems to play a dominant role in determining the mode-2 wavelengths. Due to the large spatial scales of the K_1 internal tide, f plays the dominant role in determining the wavelengths of the lowest three modes; the role of N is also visible, but less significant.

5. **How important are the details of the vertical variations of stratification in determining the wavelengths of internal tides when taking into account the WKB approximation?**

The relative discrepancies between the standard and the WKB-simplified Sturm-Liouville eigenvalue problems are frequency-independent. The application of the WKB-simplified eigenvalue problem, however, depends on N and f, and thus is spatially variable. The WKB-simplified Sturm-Liouville eigenvalue problem reveals the relative discrepancies up to 15% when compared to $L_{SL,m}$. Hence, the vertical details of N are important in the near-global analysis of internal tides, although small discrepancies are diagnosed in certain regions.

6. **What is the role the critical latitude in determining the characteristics of the $\mathbf{K_1}$ internal tide? How is the trapping process simulated in the STORMTIDE model?**

The critical latitude, 30° for the K_1 internal tide, separates different types of waves in both sides, freely propagating (both horizontally and vertically) waves in subcritical latitudes and bottom-trapped waves in supercritical latitudes, which can be well captured by the 1/10° STORMTIDE model. The surface concentration of the kinetic energy is observed equatorward of 30°, with the presence of the coastal-trapped K_1 internal tide, while the bottom-amplified kinetic energy is exhibited poleward of 30°. The kinetic energy is in a higher level in shallower than deeper ocean regions, and stratification N is found to play a significant role in determining the vertical distributions of the K_1 kinetic energy, both equatorward and poleward of 30° in the global ocean. Regarding the trapping process in supercritical latitudes, distinct decreasing rates of the K_1 kinetic energy away from the bottom are revealed, which are faster in shallower regions than in deeper regions. A further upward increase of the kinetic energy is also found above the energy minimum for waters shallower than 1500 m poleward of 30°.

4.2 Outlook

In this thesis, we describe the characteristics of the wavenumber spectra of the M_2 and K_1 internal tides in detail in Chapter 2 and 3, respectively. These spectra provide us the information about the directions of the wave energy propagation, which can also be studied by using the wave energy flux vector, or via ray tracing. A possible extension of our study is to compare the propagating directions of internal tides in detail that are derived by using different techniques.

The surface-concentrated kinetic energy is described in Chapter 3 for the K_1 internal tide in subcritical latitudes. There are several mechanisms that lead to this feature, whose roles are not separable in our concurrent simulation. Hence, their relative importances require further investigation by considering them separately, which can be done by theoretical studies or idealized model simulations.

The bottom-intensified kinetic energy is well captured in the STORMTIDE model simulation in supercritical latitudes as described in Chapter 3. One question that arises is that how the bottom-intensified energy is brought up to the upper ocean as shown by the hot spots of the K_1 kinetic energy at 52.05°S at the surface, since these waves are supposed to be confined at the ocean bottom and present no beams. We show in this study that these waves are found to be associated with the vertical distributions of stratification N. Hence, it is necessary to further investigate the detailed impact of N on the propagation of internal tides, not only in supercritical latitudes, but also in subcritical latitudes.

In Chapter 3, we show that the vertical distributions of the kinetic energy of the K_1 internal tide are distinct in various water-depth intervals, exhibiting different decreasing rates of the kinetic energy. These results are most reliable in shallower water regions due to the higher vertical resolution there. This is, however, the best that we can currently obtain due to the limitation of the vertical model resolution, in particular in the deep ocean. It reveals the necessity of the high vertical resolution in order to accurately simulate the vertical kinetic energy distributions above the bottom for bottom-trapped waves poleward of the critical latitude. It can help to reduce the possible uncertainties in the current study. The further upward increase of the kinetic energy above the energy minimum can also be better investigated in waters shallower than 1500 m in supercritical latitudes with the simulation of a high vertical resolution.

Appendix A

Remarks on the methods

During the peer-reviewed process of Chapter 2 that has been published in *Journal of Physical Oceanography*, the method has been revised to a large extent due to the relatively large errors induced in the previous one by using the regular 0.1° lonlat grid rather than the equidistant grid. It is documented here.

A.1 Two-dimensional wavenumber spectral analysis of the previous method

Initially, we performed the two-dimensional wavenumber spectral analysis within $15^\circ \times 15^\circ$ (rather than $15^\circ/cos\varphi \times 15^\circ$ as used in Chapter 2 and 3, with φ being the latitude) boxes, which is based on the standard two-dimensional discrete Fourier transform. We neglected the convergence of meridians within each $15^\circ \times 15^\circ$ regional box and used instead for simplicity a global regular 0.1° lonlat grid for the Fourier analysis. Moreover, the spectra in Eq. (2.4a) and (2.4b) were obtained for three time steps at three successive model hours ($t = 1, 2, 3$ hours in Eq. (2.3)), respectively, which correspond to different phases of a M_2 wave, to obtain robust signals. The corresponding time-mean wavenumber spectra in the (k,l) wavenumber plane were then converted into $S_{u_{bc}}(K)$ and $S_{v_{bc}}(K)$, which are functions of the horizontal wavenumber $K = \sqrt{k^2 + l^2}$. The average of $S_{u_{bc}}(K)$ and $S_{v_{bc}}(K)$ resulted in the spectrum of the kinetic energy of the

M_2 internal tide, denoted as $S_{KE}(K)$, from which the peak wavenumbers, hence the wavelengths, are diagnosed.

This part corresponds to section 2.3.2, presenting the differences between these two methods. Other details are the same for both methods, except that we raised the land points that are permitted in the spectral analysis from 10% (section A.1) to 15% (Chapter 2 and 3). In the following, when we talk about *the previous method*, we refer to the method described in this section.

A.2 Discussions concerning two methods

There are three major differences between these two methods. Firstly, in Section A.1 we took the zonal grid spacing as the value corresponding to the mid-latitude in the considered box. The most northern/southern box considered by us was centered at 52.5°N/S. Thus, the largest deviation was derived by (cos60° - cos52.5°)/cos52.5° =18%, which is a large deviation induced merely by using the regular lonlat grid.

We show in Fig. A.1 the the spectral width that is derived from the kinetic energy spectra $S_{KE}(K)$ at 100 m of the previous method, denoting the wavenumber interval between half of the maximum spectral energy at each location. There is an evident meridional variation. The general poleward increase of the spectral width represents the broader peaks in higher than lower latitudes, which is, at least partially, induced by ignoring the differences of the zonal grid spacing within a $15° \times 15°$ box. By employing the equidistant grid of the baroclinic velocities, this deviation would be eliminated. As shown in Fig. 2.5, larger spectral widths mainly occur in strong-current regions instead of in high latitudes in Fig. A.1.

Fig. A.2 shows the spectra of the M_2 baroclinic zonal tidal velocities $S_{u_{bc}}(k,l)$ and $S_{u_{bc}}(K)$ at both 100 m and 1085 m in the $15° \times 15°$ box centered at (167.5°W, 22.55°N). These spectra are derived by using the method described in Section A.1 and are located at the region very close to that in Fig. 2.3 (170°W, 22.55°N) . The corresponding wavelengths can be easily diagnosed from both $S_{u_{bc}}(k,l)$ and $S_{u_{bc}}(K)$. This feature

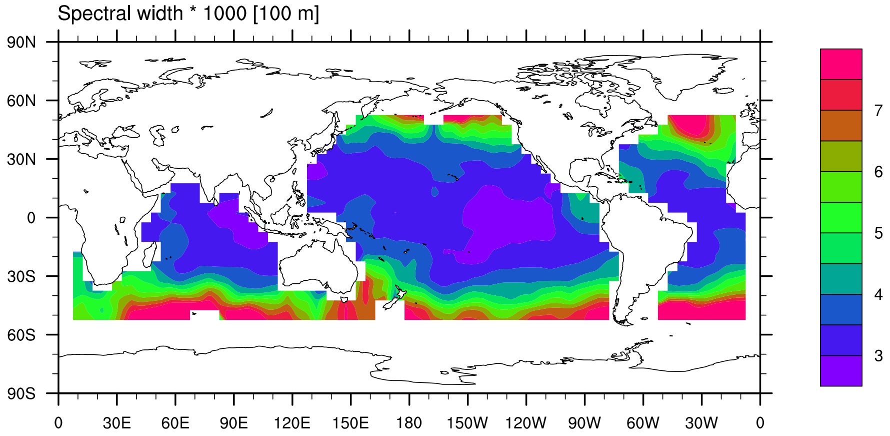

Figure A.1: Spectral width (× 1000, km^{-1}) derived from the kinetic energy spectra $S_{KE}(K)$ at 100 m of the mode-1 M$_2$ internal tide by using the previous method. The width is defined by the wavenumber internal between half of the peak energy. Nine-point smoothing has been performed after deriving the raw near-global map.

consists with those in Chapter 2 and 3 and we won't go into details. What is different here is that we observe a strong anisotropy between k and l in $S_{u_{bc}}(k,l)$ (Fig. A.2a and A.2c), in particularly at 1085 m (Fig. A.2c). This anisotropy is somewhat largely weakened and only slightly visible in Fig. 2.3, which is believed to closely related to the employment of the equidistant grid instead of the regular lonlat grid.

The second change concerns the three time slices applied in the previous method. There are exactly two linearly independent components of the signal, the in-phase and quadrature parts. The complex baroclinic zonal velocities are expressed in Eq. (2.3), and we take into account only the real part in the physical domain, which is further expressed (neglecting the indices i, j, k and t) as

$$\begin{aligned} u_{bc} =& A_{u_{bc}}\cos(2\pi\omega t - \phi_{u_{bc}}) \\ =& \underbrace{A_{u_{bc}}\cos(2\pi\omega t)\cos(\phi_{u_{bc}})}_{\text{In-phase}} - \underbrace{A_{u_{bc}}\cos(2\pi\omega t + \pi/2)\sin(\phi_{u_{bc}})}_{\text{Quadrature}}. \end{aligned} \tag{A.1}$$

Both components are offset in phase by one-quarter cycle ($\pi/2$ radians). By taking t to be $\pi/2$ apart, the complex velocities are then constructed with the in-phase $[A_{u_{bc}}\cos(\phi_{u_{bc}})]$ and quadrature $[A_{u_{bc}}\sin(\phi_{u_{bc}})]$ baroclinic velocities being the real and

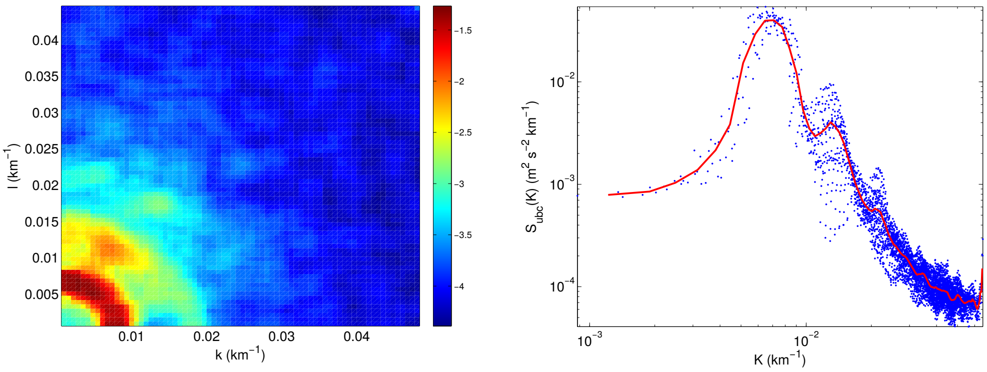

(a) *log($S_{u_{bc}}$(k,l))*, 100 m (b) *$S_{u_{bc}}$(K)*, 100 m

(c) *log($S_{u_{bc}}$(k,l))*, 1085 m (d) *$S_{u_{bc}}$(K)*, 1085 m

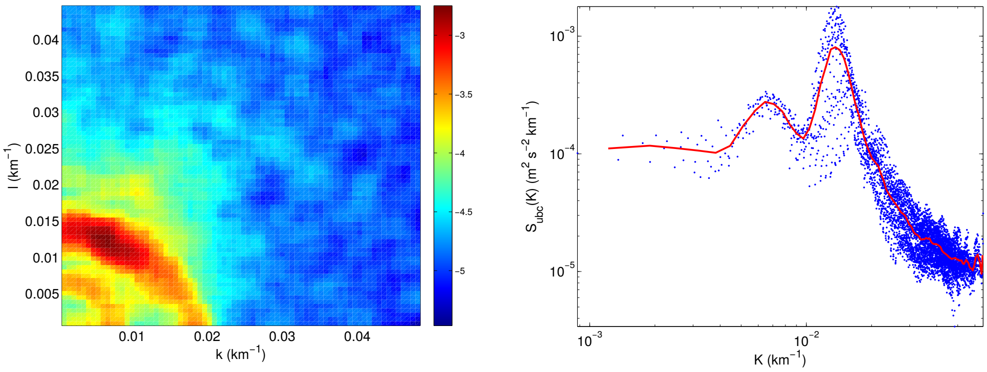

Figure A.2: Time-mean wavenumber spectra $S_{u_{bc}}(k,l)$ of the M$_2$ baroclinic zonal velocity u_{bc} at (a) 100 m and (c) 1085 m, and (b, d) the corresponding spectra $S_{u_{bc}}(K)$ converted from $S_{u_{bc}}(k,l)$ using $K = \sqrt{k^2+l^2}$, derived for the 15° × 15° box centered at (167.5°W, 22.55°N). The scattered blue dots are converted directly from each value of $S_{u_{bc}}(k,l)$. The red lines represent the bin averages of $S_{u_{bc}}(K)$, in which $S_{u_{bc}}(K_i)$ at the i^{th} interval is obtained by averaging all values of $S_{u_{bc}}(K)$ with K inside the interval (K_i,K_i+ $\triangle$). We consider a total of 100 consecutive intervals. Term $\triangle$ is obtained by dividing the total resolved wavenumber range by 100.

imaginary components, respectively. Note that a lack of any part (either the in-phase or the quadrature part) would not improve the robustness of the signal by considering more time slices in one part only.

Finally, we apply a two-dimensional Tukey window in space to the complex baroclinic velocities, which is not included in the previous method. The one-dimensional Tukey window is defined as

$$w(n) = \begin{cases} \frac{1}{2}\left[1+\cos\left(\pi\left(\frac{2n}{\alpha(N-1)}-1\right)\right)\right] & 0 \leqslant n \leqslant \frac{\alpha(N-1)}{2} \\ 1 & \frac{\alpha(N-1)}{2} \leqslant n \leqslant (N-1)(1-\frac{\alpha}{2}) \\ \frac{1}{2}\left[1+\cos\left(\pi\left(\frac{2n}{\alpha(N-1)}-\frac{2}{\alpha}+1\right)\right)\right] & (N-1)(1-\frac{\alpha}{2}) \leqslant n \leqslant (N-1) \end{cases} \tag{A.2}$$

where N is the total number of grid points that are considered in the series, $w(n)$ is the weight of the nth grid point with $0 \leqslant n \leqslant N-1$, and $\alpha = 0.3$ in our analysis. This one-dimensional Tukey function is displayed in Fig. A.3, which are further applied in both zonal and meridional directions to the complex baroclinic velocities before performing the two-dimensional wavenumber spectral analysis. The window function reduces the spectral leakage that is caused by the limitation of spatial resolution (determining the wavenumber resolution) or the limited box size, and results in ultimately the emphasis of the data in the center by tapering the signal at the endpoints.

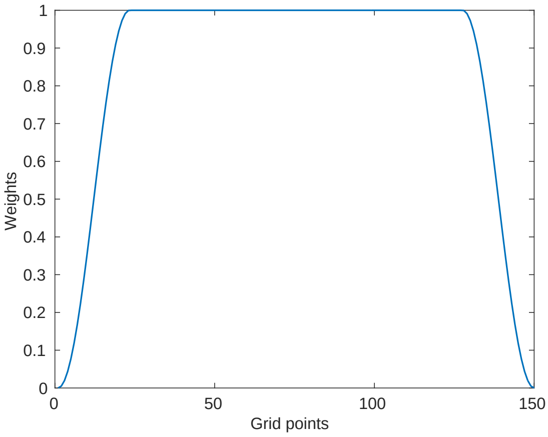

Figure A.3: Tukey window function that is used in our analysis.

Appendix B

Comparisons of $L_{SL,1}$ from model-simulated and observational N

Due to a lack of observations for three-dimensional baroclinic tidal velocities, we can take into account the results of the Sturm-Liouville eigenvalue problem applied to observed ocean stratification profiles when comparing the simulation with observations. Another method has been illustrated recently by Ray and Zaron (2016) who extracted the wavenumber distributions for the M_2 internal tide from multi satellite altimetry. In solving the eigenvalue problem, the stratification N at a resolution of 1° is interpolated vertically with a 10 m interval for both the simulation and observations. Note that there are slight differences in the calculation of the simulated and observational N. The simulated N used is the average within each $1^\circ \times 1^\circ$ boxes of the model simulation, and the observational N is located at the grid points rather than the box-averages, calculated from the temperature and salinity of the Levitus data of the 1° resolution.

The resulting mode-1 wavelengths of the M_2 internal tide are shown in Fig. B.1 for both the simulation and observations. Both distributions reveal a similar pattern, with large length scales in the northwestern Pacific, in the Gulf Stream and in the Southern Ocean. Small length scales are exhibited in the equatorial eastern Pacific and the equatorial Atlantic. The magnitudes of both distributions are comparable with only slight differences, with a similar result also presented in Ray and Zaron

(2016). In summery, the STORMTIDE wavelengths in the 1° resolution (Fig. B.1a) are comparable to those of the Levitus data (Fig. B.1b) in both magnitudes and spatial distributions.

On the other hand, the wavelengths in Fig. B.1a and Fig. 2.6b are both based on the model-simulated N, which is, however, averaged over different box sizes, with the box size of $1^\circ \times 1^\circ$ in Fig. B.1a and of $15^\circ \times 15^\circ$ in Fig. 2.6b. It is found that the magnitudes are in general larger in Fig. B.1a than those in Fig. 2.6b in strong-current regions, for instance, in the Kuroshio and Gulf Stream regions and in the Southern Ocean. These discrepancies are attributed to the different smoothing induced by various box sizes, which also accounts for the smoother patterns in Fig. 2.6b than in Fig. B.1a.

To compare the results of the two methods in Section A.1 and section 2.3.2, we show in Fig. B.2 the wavelengths of the M_2 internal tide derived by the previous method. We focus on the mode-1 wavelengths only. A remarkable discrepancy between these two methods is over the Kuroshio and its extension regions, where the mode-1 wavelengths is observed to be smaller in Fig. 2.6a than in Fig. B.2a. However, the extent of the large wavelengths of the new method (expanding from western North Pacific to the northeastern Pacific in Fig. 2.6a) is better consistent with the observations (Fig. B.1b) than the previous method (Fig. B.2a) does. Hence, the mode-1 wavelengths of the new method agree well with those of the observations (Fig. B.1b).

(a) *LSL,1* from the STORMTIDE model

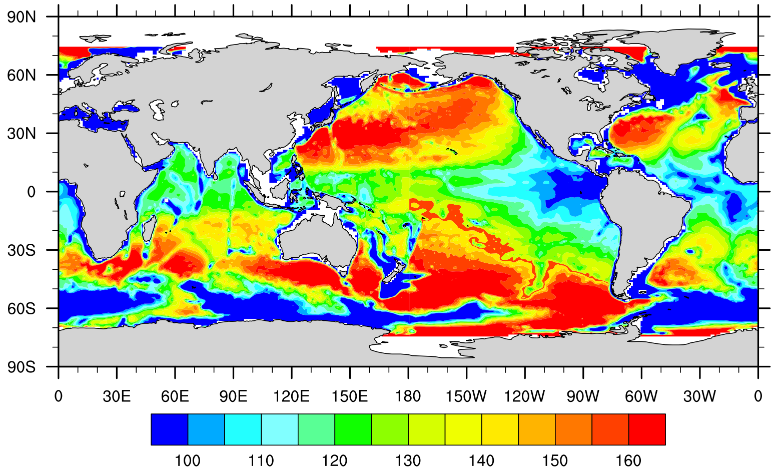
90N
60N
30N
0
30S
60S
90S
0
30E
60E
90E
120E
150E
180
150W
120W
90W
60W
30W
0
100
110
120
130
140
150
160

(b) *LSL,1* from the Levitus data

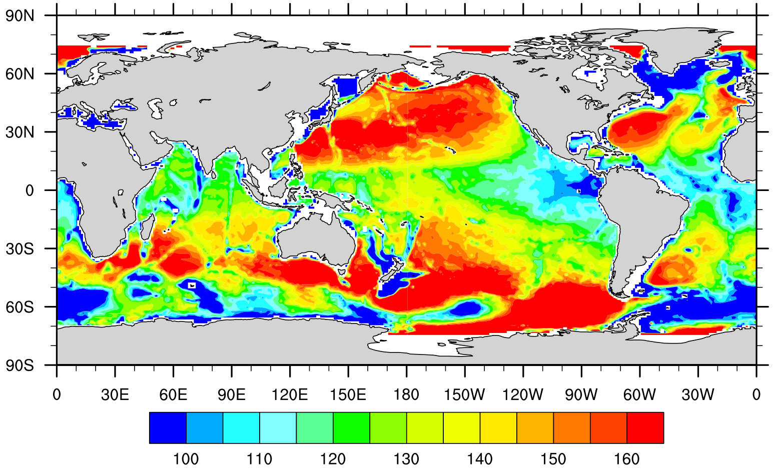
90N
60N
30N
0
30S
60S
90S
0
30E
60E
90E
120E
150E
180
150W
120W
90W
60W
30W
0
100
110
120
130
140
150
160

Figure B.1: Mode-1 wavelengths $L_{SL,1}$ (km) of the M_2 internal tide in a 1° × 1° resolution derived by solving the Sturm-Liouville eigenvalue problem (a) with the box-averaged stratification of the model simulation and (b) with the stratification derived from the Levitus temperature and salinity.

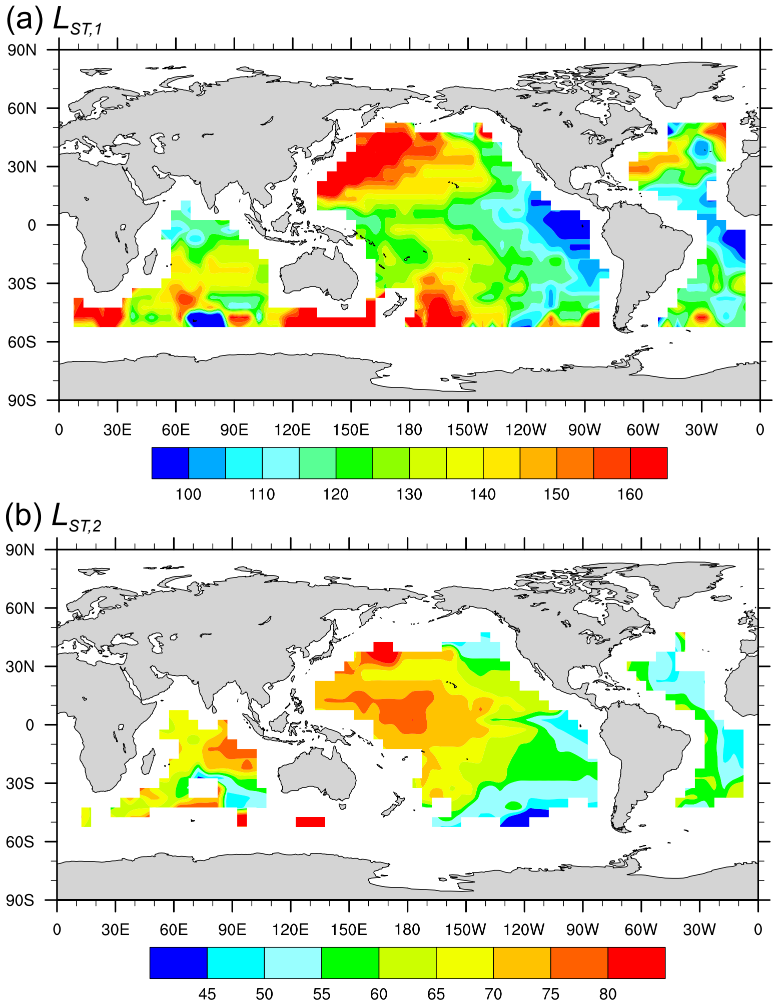
(a) $L_{ST,1}$
90N
60N
30N
0
30S
60S
90S
0
30E
60E
90E
120E
150E
180
150W
120W
90W
60W
30W
0
100
110
120
130
140
150
160
(b) $L_{ST,2}$
90N
60N
30N
0
30S
60S
90S
0
30E
60E
90E
120E
150E
180
150W
120W
90W
60W
30W
0
45
50
55
60
65
70
75
80

Figure B.2: (a) Mode-1 and (b) mode-2 wavelengths (km) of the M_2 internal tide derived from the baroclinic tidal velocities simulated by the STORMTIDE model. The box size of 15° × 15° is employed with the data interpolated onto the regular lonlat grid of 0.1°.

Appendix C

Effect of the model resolution on internal tide simulation

Tides are also implemented in the MPI-OM at a horizontal resolution of roughly 0.4°, which corresponds to a resolution of about 40 km, with 40 layers applied in the vertical. The corresponding results are shown in Fig. C.1 for the simulated kinetic energy of the M_2 and K_1 internal tides, with the colorbars consistent with those used by the 1/10° STORMTIDE simulation (Fig. 2.2 and 3.1). The hot spots of the kinetic energy are more or less captured in Fig. C.1, but in a very low energy level compared with those of the high-resolution simulation (Fig. 2.2 and 3.1).

We also find the absence of the K_1 critical latitude at 30° in this 0.4°-resolution simulation. It means that the 0.4° resolution is not sufficient to properly resolve the K_1 internal tide. It is widely accepted that eight grid points per wavelengths are required in the model in order to properly resolve these waves (e.g., Arbic et al. 2010). Hence, with a roughly 40 km resolution, even the mode-1 K_1 internal tide with the length scales of about 200-400 km cannot be always well resolved equatorward of 30°, for instance, in regions near the equator where the relatively small wavelengths cannot expand over eight grid points. Based on the fact that at least three grid points per wavelength are required for a wave to be recognized in the model, the mode-2 K_1 internal tide at least can be resolved in this 0.4° MPI-OM simulation, while mode 3 cannot be guaranteed to be resolved in the equatorial regions, which is worse for higher modes. Thus, a high-resolution model is required in simulating internal tides. Fig. C.2 shows the amplitudes and phases of the K_1 internal tide simulated by the 0.4° MPI-OM model. Again, we observe the absence of the critical latitude in the amplitudes (Fig. C.2a), which is, however, presented by the distribution of the phases (Fig. C.2b). Due to the poor capability of the 0.4° model in simulating internal tides, we will not look into details concerning this phenomenon.

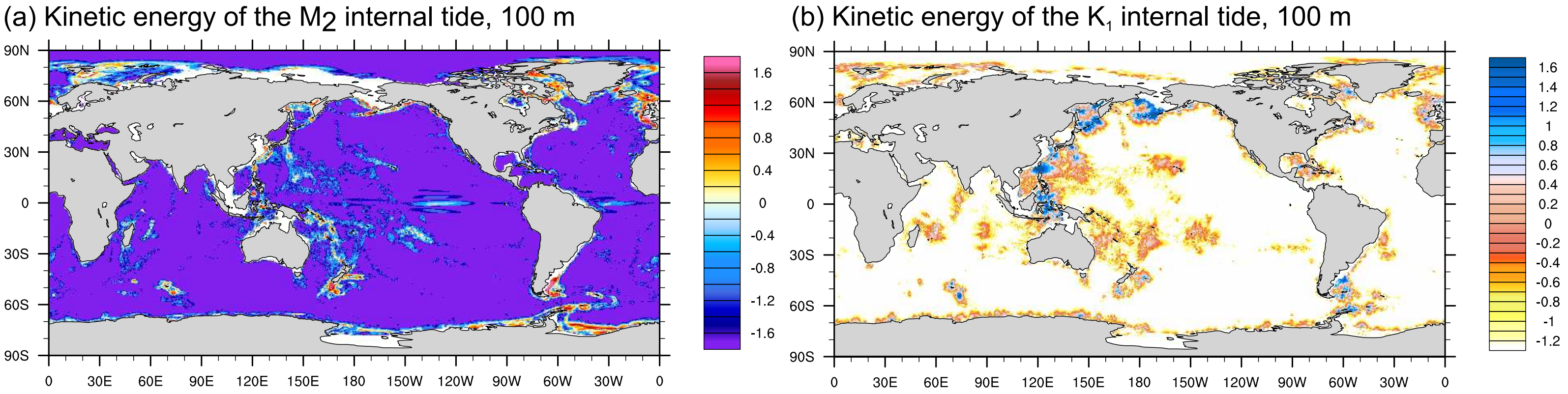
(a) Kinetic energy of the M_2 internal tide, 100 m

(b) Kinetic energy of the K_1 internal tide, 100 m

90N
60N
30N
0
30S
60S
90S
0
30E
60E
90E
120E
150E
180
150W
120W
90W
60W
30W
0
1.6
1.2
0.8
0.4
0
-0.4
-0.8
-1.2
-1.6
1.6
1.4
1.2
1
0.8
0.6
0.4
0.2
0
-0.2
-0.4
-0.6
-0.8
-1
-1.2

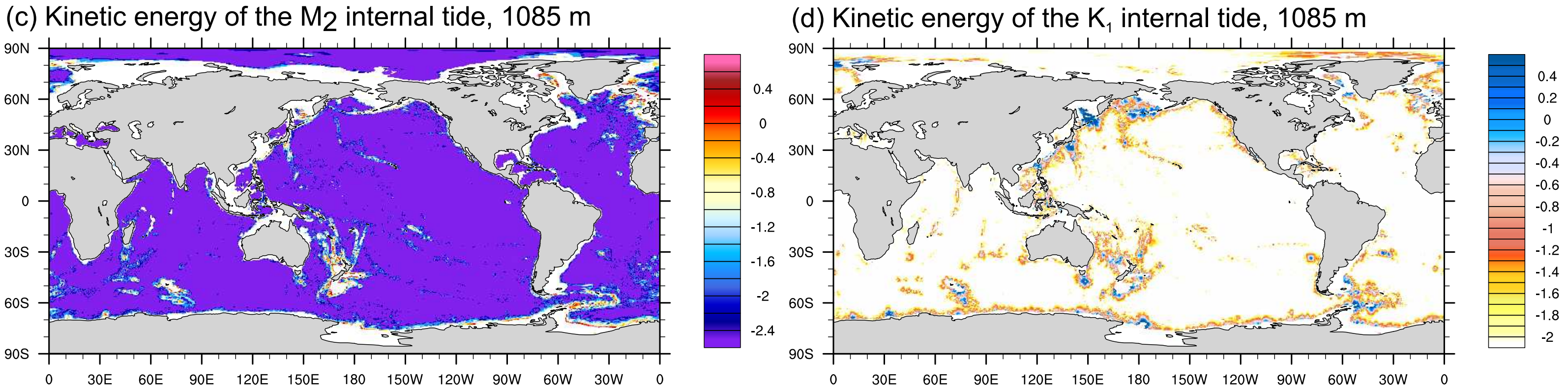
(c) Kinetic energy of the M_2 internal tide, 1085 m

(d) Kinetic energy of the K_1 internal tide, 1085 m

90N
60N
30N
0
30S
60S
90S
0
30E
60E
90E
120E
150E
180
150W
120W
90W
60W
30W
0
0.4
0
-0.4
-0.8
-1.2
-1.6
-2
-2.4
0.4
0.2
0
-0.2
-0.4
-0.6
-0.8
-1
-1.2
-1.4
-1.6
-1.8
-2

Figure C.1: Kinetic energy (cm^2 s^{-2}, in logarithmic scales) of the M_2 internal tide at (a) 100 m and (c) 1085 m, simulated by the 0.4°-resolution MPI-OM, in which tides are implemented. The kinetic energy distributions from the same model simulation are shown at (b) 100 m and (d) 1085 m for the K_1 internal tide.

(a) Amplitude of zonal velocities of the K_1 internal tide, 100 m

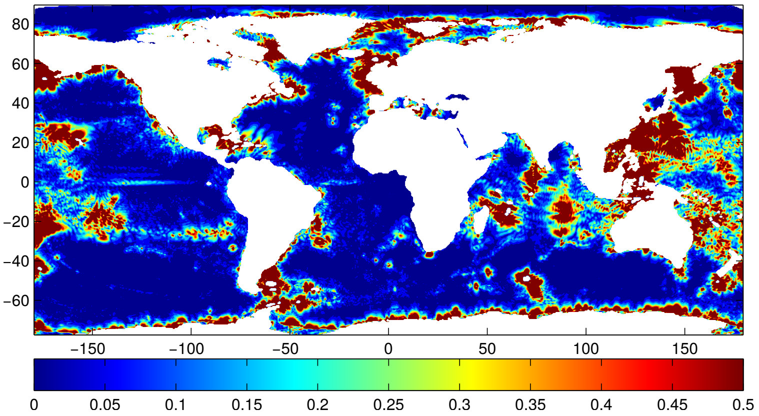
80
60
40
20
0
−20
−40
−60
−150
−100
−50
0
50
100
150
0
0.05
0.1
0.15
0.2
0.25
0.3
0.35
0.4
0.45
0.5

(b) Phase of zonal velocities of the K_1 internal tide, 100 m

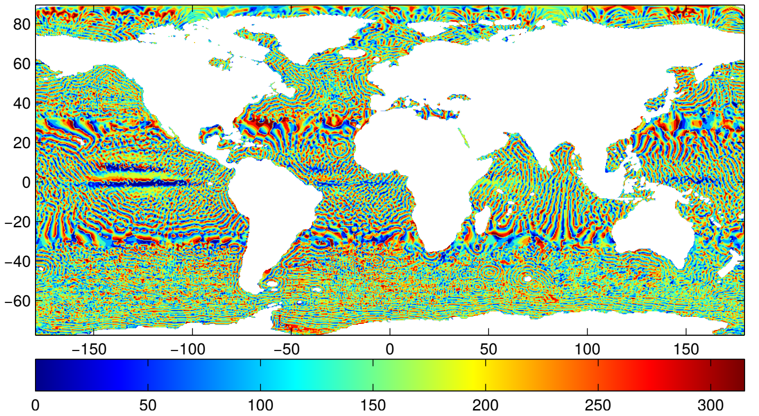
80
60
40
20
0
-20
-40
-60
−150
−100
-50
0
50
100
150
0
50
100
150
200
250
300

Figure C.2: (a) Amplitudes (cm) and (b) phases (degree) of the K_1 baroclinic zonal velocities at 100 m that are simulated by the 0.4°-resolution MPI-OM, in which tides are implemented.

Bibliography

Akylas, T. R., R. H. J. Grimshaw, S. R. Clarke, and A. Tabaei, 2007: Reflecting tidal wave beams and local generation of solitary waves in the ocean thermocline. *J. Fluid Mech.*, **593**, 297–313, doi:10.1017/S0022112007008786.

Alford, M. H., 2001: Internal swell generation: The spatial distribution of energy flux from the wind to mixed layer near-inertial motions. *J. Phys. Oceanogr.*, **31**, 2359–2368, doi:10.1175/1520-0485(2001)031<2359:ISGTSD>2.0.CO;2.

Alford, M. H., 2003: Redistribution of energy available for ocean mixing by long-range propagation of internal waves. *Nature*, **423**, 159–162, doi:10.1038/nature01628.

Alford, M. H., J. A. MacKinnon, H. L. Simmons, and J. D. Nash, 2016: Near-inertial internal gravity waves in the ocean. *Ann. Rev. Mar. Sci.*, **8**, 95–123, doi:10.1146/annurev-marine-010814-015746.

Arbic, B. K., J. G. Richman, J. F. Shriver, P. G. Timko, E. J. Metzger, and A. J. Wallcraft, 2012: Global modeling of internal tides within an eddying ocean general circulation model. *Oceanography*, **25 (2)**, 20–29, doi:http://dx.doi.org/10.5670/oceanog.2012.38.

Arbic, B. K., A. J. Wallcraft, and E. J. Metzger, 2010: Concurrent simulation of the eddying general circulation and tides in a global ocean model. *Ocean Model.*, **32**, 175–187, doi:10.1016/j.ocemod.2010.01.007.

Broutman, D., J. W. Rottman, and S. D. Eckermann, 2004: Ray methods for internal waves in the atmosphere and ocean. *Annu. Rev. Fluid Mech.*, **36**, 233–253, doi: 10.1146/annurev.fluid.36.050802.122022.

Bryan, K., and L. J. Lewis, 1979: A water mass model of the world ocean. *J. Geophys. Res.*, **84 (C5)**, 2503–2517, doi:10.1029/JC084iC05p02503.

Carrère, L., and F. Lyard, 2003: Modeling the barotropic response of the global ocean to atmospheric wind and pressure forcing - comparisons with observations. *Geophys. Res. Lett.*, **30 (6)**, 1–8, doi:10.1029/2002GL016473.

Carter, G. S., O. B. Fringer, and E. D. Zaron, 2012: Regional models of internal tides. *Oceanography*, **25 (2)**, 56–65, doi:http://dx.doi.org/10.5670/oceanog.2012.42.

Cartwright, D. E., and R. D. Ray, 1990: Oceanic tides from Geosat altimetry. *J. Geophys. Res.*, **95 (C3)**, 3069–3090, doi:10.1029/JC095iC03p03069.

Chavanne, C., P. Flament, D. Luther, and K.-W. Gurgel, 2010: The surface expression of semidiurnal internal tides near a strong source at Hawaii. Part II: Interactions with mesoscale currents. *J. Phys. Oceanogr.*, **40**, 1180–1200, doi:10.1175/2010JPO4223.1.

Chelton, D. B., R. A. DeSzoeke, M. G. Schlax, K. El Naggar, and N. Siwertz, 1998: Geographical variability of the first baroclinic Rossby radius of deformation. *J. Phys. Oceanogr.*, **28**, 433–460, doi:10.1175/1520-0485(1998)028<0433:GVOTFB>2.0.CO; 2.

Cherniawsky, J. Y., M. G. G. Foreman, W. R. Crawford, and R. F. Henry, 2001: Ocean tides from TOPEX/Poseidon sea level data. *J. Atmos. Ocean. Technol.*, **18**, 649–664, doi:http://dx.doi.org/10.1175/1520-0426(2001)018<0649:OTFTPS>2.0.CO;2.

Eden, C., and D. Olbers, 2014: An energy compartment model for propagation, nonlinear interaction, and dissipation of internal gravity waves. *J. Phys. Oceanogr.*, **44**, 2093–2106, doi:10.1175/JPO-D-13-0224.1.

Egbert, G. D., and R. D. Ray, 2000: Significant dissipation of tidal energy in the deep ocean inferred from satellite altimeter data. *Nature*, **405**, 775–778, doi:10.1038/35015531.

Egbert, G. D., and R. D. Ray, 2003: Semi-diurnal and diurnal tidal dissipation from TOPEX/Poseidon altimetry. *Geophys. Res. Lett.*, **30 (17)**, 1–9, doi:10.1029/2003GL017676.

Egbert, G. D., R. D. Ray, and B. G. Bills, 2004: Numerical modeling of the global semidiurnal tide in the present day and in the last glacial maximum. *J. Geophys. Res.*, **109**, C03 003, doi:10.1029/2003JC001973.

Exarchou, E., J.-S. von Storch, and J. H. Jungclaus, 2012: Impact of tidal mixing with different scales of bottom roughness on the general circulation. *Ocean Dyn.*, **62 (10)**, 1545–1563, doi:10.1007/s10236-012-0573-1.

Exarchou, E., J.-S. von Storch, and J. H. Jungclaus, 2014: Sensitivity of transient climate change to tidal mixing: Southern Ocean heat uptake in climate change experiments performed with ECHAM5/MPIOM. *Clim. Dyn.*, **42**, 1755–1773, doi:10.1007/s00382-013-1776-y.

Falahat, S., and J. Nycander, 2015: On the generation of bottom-trapped internal tides. *J. Phys. Oceanogr.*, **45**, 526–545, doi:10.1175/JPO-D-14-0081.1.

Faller, A. J., 1966: Sources of energy for the ocean circulation and a theory of the mixed layer. *Proc. 5th U.S. Congr. Appl. Mech., ASME, Univ. Minnesota, Minneap.*, 651–672.

Fer, I., M. Müller, and A. K. Peterson, 2015: Tidal forcing, energetics, and mixing near the Yermak Plateau. *Ocean Sci.*, **11**, 287–304, doi:10.5194/os-11-287-2015.

Foreman, M. G. G., J. Y. Cherniawsky, and V. A. Ballantyne, 2009: Versatile harmonic tidal analysis: Improvements and applications. *J. Atmos. Ocean. Technol.*, **26**, 806–817, doi:10.1175/2008JTECHO615.1.

Furuichi, N., T. Hibiya, and Y. Niwa, 2008: Model-predicted distribution of wind-induced internal wave energy in the world's oceans. *J. Geophys. Res.*, **113**, C09 034, doi:10.1029/2008JC004768.

Garabato, A. C. N., K. L. Polzin, B. A. King, K. J. Heywood, and M. Visbeck, 2004: Widespread intense turbulent mixing in the Southern Ocean. *Science*, **303**, 210–213, doi:10.1126/science.1090929.

Garrett, C., 2001: What is the "near-inertial" band and why is it different from the rest of the internal wave spectrum? *J. Phys. Oceanogr.*, **31**, 962–971, doi:http://dx.doi.org/10.1175/1520-0485(2001)031<0962:WITNIB>2.0.CO;2.

Garrett, C., and E. Kunze, 2007: Internal tide generation in the deep ocean. *Annu. Rev. Fluid Mech.*, **39**, 57–87, doi:10.1146/annurev.fluid.39.050905.110227.

Gerkema, T., C. Staquet, and P. Bouruet-Aubertot, 2006: Decay of semi-diurnal internal-tide beams due to subharmonic resonance. *Geophys. Res. Lett.*, **33 (8)**, L08 604, doi:10.1029/2005GL025105.

Gerkema, T., and H. van Haren, 2012: Absence of internal tidal beams due to non-uniform stratification. *J. Sea Res.*, **74**, 2–7, doi:10.1016/j.seares.2012.03.008.

Gerkema, T., and J. T. F. Zimmerman, 2008: *An introduction to internal waves*. 207 pp.

Green, J. A. M., and J. Nycander, 2013: A comparison of tidal conversion parameterizations for tidal models. *J. Phys. Oceanogr.*, **43**, 104–119, doi:10.1175/JPO-D-12-023.1.

Gregg, M. C., T. B. Sanford, and D. P. Winkel, 2003: Reduced mixing from the breaking of internal waves in equatorial waters. *Nature*, **422**, 513–515, doi:10.1038/nature01507.

Hasumi, H., and N. Suginohara, 1999: Effects of locally enhanced vertical diffusivity over rough bathymetry on the world ocean circulation. *J. Geophys. Res.*, **104 (C10)**, 23 367–23 374, doi:10.1029/1999JC900191.

Huang, R. X., and X. Jin, 2002: Deep circulation in the South Atlantic induced by bottom-intensified mixing over the Midocean Ridge. *J. Phys. Oceanogr.*, **32**, 1150–1164, doi:10.1175/1520-0485(2002)032<1150:DCITSA>2.0.CO;2.

Jan, S., C.-S. Chern, J. Wang, and S.-Y. Chao, 2007: Generation of diurnal K_1 internal tide in the Luzon Strait and its influence on surface tide in the South China Sea. *J. Geophys. Res.*, **112 (C6)**, C06 019, doi:10.1029/2006JC004003.

Jayne, S. R., 2009: The impact of abyssal mixing parameterizations in an ocean general circulation model. *J. Phys. Oceanogr.*, **39**, 1756–1775, doi:10.1175/2009JPO4085.1.

Jayne, S. R., and L. C. St. Laurent, 2001: Parameterizing tidal dissipation over rough topography. *Geophys. Res. Lett.*, **28 (5)**, 811–814, doi:10.1029/2000GL012044.

Jochum, M., B. P. Briegleb, G. Danabasoglu, W. G. Large, N. J. Norton, S. R. Jayne, M. H. Alford, and F. O. Bryan, 2013: The impact of oceanic near-inertial waves on climate. *J. Clim.*, **26**, 2833–2844, doi:10.1175/JCLI-D-12-00181.1.

Jungclaus, J. H., and Coauthors, 2006: Ocean circulation and tropical variability in the coupled model ECHAM5/MPI-OM. *J. Clim.*, **19**, 3952–3972, doi:10.1175/JCLI3827.1.

Köhler, J., 2013: Long-term variability of internal waves and diapycnal mixing: The role of the North Atlantic Deep Western Boundary Current. Ph.D. thesis, 1–102 pp.

Kuhlbrodt, T., A. Griesel, M. Montoya, A. Levermann, M. Hofmann, and S. Rahmstorf, 2007: On the driving processes of the Atlantic meridional overturning circulation. *Rev. Geophys.*, **45 (2)**, RG2001, doi:10.1029/2004RG000166.

Kunze, E., 1985: Near-inertial wave propagation in geostrophic shear. *J. Phys. Oceanogr.*, **15**, 544–565, doi:10.1175/1520-0485(1985)015<0544:NIWPIG>2.0.CO;2.

Ledwell, J. R., E. T. Montgomery, K. L. Polzin, L. C. St. Laurent, R. W. Schmitt, R. W. Schmitt, and J. M. Toole, 2000: Evidence for enhanced mixing over rough topography in the abyssal ocean. *Nature*, **403**, 179–182, doi:10.1038/35003164.

Ledwell, J. R., A. J. Watson, and C. S. Law, 1993: Evidence for slow mixing across the pycnocline from an open-ocean tracer-release experiment. *Nature*, **364**, 701–703, doi:10.1038/364701a0.

Maltrud, M. E., and J. L. McClean, 2005: An eddy resolving global 1/10° ocean simulation. *Ocean Model.*, **8 (1-2)**, 31–54, doi:10.1016/j.ocemod.2003.12.001.

Marshall, J., and K. Speer, 2012: Closure of the meridional overturning circulation through Southern Ocean upwelling. *Nat. Geosci.*, **5**, 171–180, doi:10.1038/ngeo1391.

Marsland, S. J., H. Haak, J. H. Jungclaus, M. Latif, and F. Röske, 2003: The Max-Planck-Institute global ocean/sea ice model with orthogonal curvilinear coordinates. *Ocean Model.*, **5 (2)**, 91–127, doi:10.1016/S1463-5003(02)00015-X.

Martin, J. P., D. L. Rudnick, and R. Pinkel, 2006: Spatially broad observations of internal waves in the upper ocean at the Hawaiian Ridge. *J. Phys. Oceanogr.*, **36**, 1085–1103, doi:10.1175/JPO2881.1.

Masumoto, Y., and Coauthors, 2004: A fifty-year eddy-resolving simulation of the world ocean: Preliminary outcomes of OFES (OGCM for the Earth Simulator). *J. Earth Simulator*, **1**, 35–56.

Mathur, M., and T. Peacock, 2009: Internal wave beam propagation in non-uniform stratifications. *J. Fluid Mech.*, **639**, 133–152, doi:10.1017/S0022112009991236.

Melet, A., R. Hallberg, S. Legg, and K. Polzin, 2013: Sensitivity of the ocean state to the vertical distribution of internal-tide-driven mixing. *J. Phys. Oceanogr.*, **43**, 602–615, doi:10.1175/JPO-D-12-055.1.

Montenegro, Á., M. Eby, A. J. Weaver, and S. R. Jayne, 2007: Response of a climate model to tidal mixing parameterization under present day and last glacial maximum conditions. *Ocean Model.*, **19 (3-4)**, 125–137, doi:10.1016/j.ocemod.2007.06.009.

Moum, J. N., D. R. Caldwell, J. D. Nash, and G. D. Gunderson, 2002: Observations of boundary mixing over the continental slope. *J. Phys. Oceanogr.*, **32**, 2113–2130, doi:10.1175/1520-0485(2002)032<2113:OOBMOT>2.0.CO;2.

Moum, J. N., and T. R. Osborn, 1986: Mixing in the main thermocline. *J. Phys. Oceanogr.*, **16**, 1250–1259, doi:10.1175/1520-0485(1986)016<1250:MITMT>2.0.CO;2.

Mowbray, D. E., and B. S. H. Rarity, 1967: A theoretical and experimental investigation of the phase configuration of internal waves of small amplitude in a density stratified liquid. *J. Fluid Mech.*, **28**, 1–16, doi:http://dx.doi.org/10.1017/S0022112067001867.

Müller, M., 2012: High resolution ocean circulation and tides. CERA-DB DKRZ LTA 510. URL http://cera-www.dkrz.de/WDCC/ui/Entry.jsp?acronym=DKRZ_lta_510.

Müller, M., 2013: On the space- and time-dependence of barotropic-to-baroclinic tidal energy conversion. *Ocean Model.*, **72**, 242–252, doi:10.1016/j.ocemod.2013.09.007.

Müller, M., B. K. Arbic, J. G. Richman, J. F. Shriver, E. L. Kunze, R. B. Scott, A. J. Wallcraft, and L. Zamudio, 2015: Toward an internal gravity wave spectrum in global ocean models. *Geophys. Res. Lett.*, **42**, 3474–3481, doi:10.1002/2015GL063365.

Müller, M., J. Y. Cherniawsky, M. G. G. Foreman, and J.-S. von Storch, 2012: Global M_2 internal tide and its seasonal variability from high resolution ocean circulation and tide modeling. *Geophys. Res. Lett.*, **39 (19)**, L19 607, doi:10.1029/2012GL053320.

Müller, M., J. Y. Cherniawsky, M. G. G. Foreman, and J.-S. von Storch, 2014: Seasonal variation of the M_2 tide. *Ocean Dyn.*, **64**, 159–177, doi:10.1007/s10236-013-0679-0.

Müller, M., H. Haak, J. Jungclaus, J. Sündermann, and M. Thomas, 2010: The effect of ocean tides on a climate model simulation. *Ocean Model.*, **35 (4)**, 304–313, doi:10.1016/j.ocemod.2010.09.001.

Munk, W., and C. Wunsch, 1998: Abyssal recipes II: energetics of tidal and wind mixing. *Deep. Res.*, **45 (12)**, 1977–2010, doi:10.1016/S0967-0637(98)00070-3.

Munk, W. H., 1966: Abyssal recipes. *Deep Sea Res. Oceanogr. Abstr.*, **13 (4)**, 707–730, doi:10.1016/0011-7471(66)90602-4.

Nakamura, T., T. Awaji, T. Hatayama, K. Akitomo, T. Takizawa, T. Kono, Y. Kawasaki, and M. Fukasawa, 2000: The generation of large-amplitude unsteady lee waves by subinertial K_1 tidal flow: A possible vertical mixing mechanism in the Kuril Straits. *J. Phys. Oceanogr.*, **30**, 1601–1621, doi:10.1175/1520-0485(2000)030<1601:TGOLAU>2.0.CO;2.

Niwa, Y., and T. Hibiya, 2001: Numerical study of the spatial distribution of the M_2 internal tide in the Pacific Ocean. *J. Geophys. Res.*, **106 (C10)**, 22 441–22 449, doi:10.1029/2000JC000770.

Olbers, D., J. Willebrand, and C. Eden, 2012: *Ocean Dynamics.* Springer Verlag, 704 pp., doi:10.1007/978-3-642-23450-7.

Oort, A. H., L. A. Anderson, and J. P. Peixoto, 1994: Estimates of the energy cycle of the oceans. *J. Geophys. Res.*, **99 (C4)**, 7665–7688, doi:10.1029/93JC03556.

Osborn, T. R., 1980: Estimates of the local rate of vertical diffusion from dissipation measurements. *J. Phys. Oceanogr.*, **10**, 83–89, doi:10.1175/1520-0485(1980)010<0083:EOTLRO>2.0.CO;2.

Pairaud, I., C. Staquet, J. Sommeria, and M. M. Mahdizadeh, 2010: Generation of harmonics and sub-harmonics from an internal tide in a uniformly stratified fluid: numerical and laboratory experiments. *IUTAM Symp. Turbul. Atmos. Ocean.*, D. Dritschel, Ed., Vol. 28, Springer Netherlands, 51–62, doi:10.1007/978-94-007-0360-5{_}5.

Parke, M. E., and M. C. Hendershott, 1980: M_2, S_2, K_1 models of the global ocean tide on an elastic earth. *Mar. Geod.*, **3 (1-4)**, 379–408, doi:10.1080/01490418009388005.

Pickering, A., and M. H. Alford, 2012: Velocity structure of internal tide beams emanating from Kaena Ridge , Hawaii. *J. Phys. Oceanogr.*, **42**, 1039–1044, doi:10.1175/JPO-D-12-018.1.

Plag, H.-P., and M. Perlman, 2009: *Global geodetic observing system: Meeting the requirements of a global society on a changing planet in 2020.* 332 pp., doi:10.1007/978-3-642-02687-4.

Polzin, K., J. Toole, J. R. Ledwell, and R. W. Schmitt, 1997: Spatial variability of turbulent mixing in the abyssal ocean. *Science*, **276 (5309)**, 93–96, doi:10.1126/science.276.5309.93.

Polzin, K. L., and Y. V. Lvov, 2011: Toward regional characterizations of the oceanic internal wavefield. *Rev. Geophys.*, **49 (4)**, RG4003, doi:10.1029/2010RG000329.

Rahmstorf, S., 2006: Thermohaline ocean circulation. Elsevier, Amsterdam, 1–10 pp.

Rainville, L., and R. Pinkel, 2006: Propagation of low-mode internal waves through the ocean. *J. Phys. Oceanogr.*, **36**, 1220–1236, doi:10.1175/JPO2889.1.

Ray, R. D., 2007: Decadal climate variability: Is there a tidal connection? *J. Clim.*, **20**, 3542–3560, doi:10.1175/JCLI4193.1.

Ray, R. D., and G. T. Mitchum, 1996: Surface manifestation of internal tides generated near Hawaii. *Geophys. Res. Lett.*, **23 (16)**, 2101–2104, doi:10.1029/96GL02050.

Ray, R. D., and G. T. Mitchum, 1997: Surface manifestation of internal tides in the deep ocean: Observations from altimetry and island gauges. *Prog. Oceanogr.*, **40 (1-4)**, 135–162, doi:10.1016/S0079-6611(97)00025-6.

Ray, R. D., and E. D. Zaron, 2011: Non-stationary internal tides observed with satellite altimetry. *Geophys. Res. Lett.*, **38 (17)**, L17 609, doi:10.1029/2011GL048617.

Ray, R. D., and E. D. Zaron, 2016: M_2 internal tides and their observed wavenumber spectra from satellite altimetry. *J. Phys. Oceanogr.*, **46**, 3–22, doi:10.1175/JPO-D-15-0065.1.

Rhines, P., 1970: Edge-, bottom-, and Rossby waves in a rotating stratified fluid. *Geophys. Fluid Dyn.*, **1 (3-4)**, 273–302, doi:10.1080/03091927009365776.

Richman, J. G., B. K. Arbic, J. F. Shriver, E. J. Metzger, and Wallcraft Alan J., 2012: Inferring dynamics from the wavenumber spectra of an eddying global ocean model with embedded tides. *J. Geophys. Res.*, **117**, C12 012, doi:10.1029/2012JC008364.

Rimac, A., 2014: The role of wind induced near-inertial waves on the energetics of the ocean. Ph.D. thesis, 116 pp.

Rimac, A., J. S. Von Storch, C. Eden, and H. Haak, 2013: The influence of high-resolution wind stress field on the power input to near-inertial motions in the ocean. *Geophys. Res. Lett.*, **40 (18)**, 4882–4886, doi:10.1002/grl.50929.

Saenko, O. A., 2006: The effect of localized mixing on the ocean circulation and time-dependent climate change. *J. Phys. Oceanogr.*, **36**, 140–160, doi:10.1175/JPO2839.1.

Saenko, O. A., and W. J. Merryfield, 2005: On the effect of topographically enhanced mixing on the global ocean circulation. *J. Phys. Oceanogr.*, **35**, 826–834, doi:10.1175/JPO2722.1.

Sandström, J. W., 1908: Dynamische Versuche mit Meerwasser. *Ann. Hydrogr. Marit. Meteorol.*, **36**, 6–23.

Schiller, A., and R. Fiedler, 2007: Explicit tidal forcing in an ocean general circulation model. *Geophys. Res. Lett.*, **34 (3)**, L03 611, doi:10.1029/2006GL028363.

Schmittner, A., and G. D. Egbert, 2014: An improved parameterization of tidal mixing for ocean models. *Geosci. Model Dev.*, **7**, 211–224, doi:10.5194/gmd-7-211-2014.

Schwiderski, E. W., 1980: On charting global ocean tides. *Rev. Geophys.*, **18 (1)**, 243–268, doi:10.1029/RG018i001p00243.

Shriver, J. F., B. K. Arbic, J. G. Richman, R. D. Ray, E. J. Metzger, A. J. Wallcraft, and P. G. Timko, 2012: An evaluation of the barotropic and internal tides in a high-resolution global ocean circulation model. *J. Geophys. Res.*, **117**, C10 024, doi:10.1029/2012JC008170.

Shriver, J. F., J. G. Richman, and B. K. Arbic, 2014: How stationary are the internal tides in a high-resolution global ocean circulation model? *J. Geophys. Res. Ocean.*, **119**, 2769–2787, doi:10.1002/2013JC009423.

Simmons, H. L., and M. H. Alford, 2012: Simulating the long-range swell of internal waves generated by ocean storms. *Oceanography*, **25 (2)**, 30–41, doi:10.5670/oceanog.2012.39.

Simmons, H. L., R. W. Hallberg, and B. K. Arbic, 2004a: Internal wave generation in a global baroclinic tide model. *Deep. Res.*, **51 (25-26)**, 3043–3068, doi:10.1016/j.dsr2.2004.09.015.

Simmons, H. L., S. R. Jayne, L. C. St. Laurent, and A. J. Weaver, 2004b: Tidally driven mixing in a numerical model of the ocean general circulation. *Ocean Model.*, **6 (3-4)**, 245–263, doi:10.1016/S1463-5003(03)00011-8.

St. Laurent, L., and C. Garrett, 2002: The role of internal tides in mixing the deep ocean. *J. Phys. Oceanogr.*, **32**, 2882–2899, doi:10.1175/1520-0485(2002)032<2882:TROITI>2.0.CO;2.

St. Laurent, L. C., H. L. Simmons, and S. R. Jayne, 2002: Estimating tidally driven mixing in the deep ocean. *Geophys. Res. Lett.*, **29 (23)**, 21–1–21–4, doi:10.1029/2002GL015633.

Stammer, D., and Coauthors, 2014: Accuracy assessment of global barotropic ocean tide models. *Rev. Geophys.*, **52 (3)**, 243–282, doi:10.1002/2014RG000450.

Steele, M., R. Morley, and W. Ermold, 2001: PHC: A global ocean hydrography with a high-quality Arctic Ocean. *J. Clim.*, **14**, 2079–2087, doi:10.1175/1520-0442(2001)014<2079:PAGOHW>2.0.CO;2.

Stommel, H., and A. B. Arons, 1959: On the abyssal circulation of the world ocean - II. An idealized model of the circulation pattern and amplitude in oceanic basins. *Deep Sea Res.*, **6**, 219–233, doi:10.1016/0146-6313(59)90075-9.

Tanaka, Y., T. Hibiya, Y. Niwa, and N. Iwamae, 2010: Numerical study of K_1 internal tides in the Kuril Straits. *J. Geophys. Res.*, **115 (C9)**, C09 016, doi: 10.1029/2009JC005903.

Thomas, M., J. Sündermann, and E. Maier-Reimer, 2001: Consideration of ocean tides in an OGCM and impacts on subseasonal to decadal polar motion excitation. *Geophys. Res. Lett.*, **28 (12)**, 2457–2460, doi:10.1029/2000GL012234.

Timko, P. G., B. K. Arbic, J. G. Richman, R. B. Scott, E. J. Metzger, and A. J. Wallcraft, 2013: Skill testing a three-dimensional global tide model to historical current meter records. *J. Geophys. Res. Ocean.*, **118 (12)**, 6914–6933, doi:10.1002/2013JC009071.

Turner, J. S., 1973: *Buoyancy effects in fluids.* Cambridge University Press, 1–368 pp., doi:http://dx.doi.org/10.1017/CBO9780511608827.

von Storch, J.-S., C. Eden, I. Fast, H. Haak, D. Hernández-Deckers, E. Maier-Reimer, J. Marotzke, and D. Stammer, 2012: An estimate of the Lorenz energy cycle for the world ocean based on the 1/10° STORM/NCEP simulation. *J. Phys. Oceanogr.*, **42**, 2185–2205, doi:10.1175/JPO-D-12-079.1.

Watanabe, M., and T. Hibiya, 2002: Global estimates of the wind-induced energy flux to inertial motions in the surface mixed layer. *Geophys. Res. Lett.*, **29 (8)**, 64–1—64–3, doi:10.1029/2001GL014422.

Wunsch, C., and R. Ferrari, 2004: Vertical mixing, energy, and the general circulation of the oceans. *Annu. Rev. Fluid Mech.*, **36**, 281–314, doi:10.1146/annurev.fluid.36.050802.122121.

Zhai, X., R. J. Greatbatch, C. Eden, and T. Hibiya, 2009: On the loss of wind-induced near-inertial energy to turbulent mixing in the upper ocean. *J. Phys. Oceanogr.*, **39**, 3040–3045, doi:10.1175/2009JPO4259.1.

Zhao, Z., M. H. Alford, and J. B. Girton, 2012: Mapping low-mode internal tides from multisatellite altimetry. *Oceanography*, **25**, 42–51, doi:http://dx.doi.org/10.5670/oceanog.2012.40.

Zickfeld, K., A. Levermann, M. G. Morgan, T. Kuhlbrodt, S. Rahmstorf, and D. W. Keith, 2007: Expert judgements on the response of the Atlantic meridional overturning circulation to climate change. *Clim. Change*, **82 (3-4)**, 235–265, doi: 10.1007/s10584-007-9246-3.

List of Figures

1.1 Simplified sketch of the global overturning circulation system. Surface currents are shown in red, deep waters in light blue and bottom waters in brown. From Kuhlbrodt et al. (2007). 3

1.2 Schematic of energy pathways in the ocean. Astronomical forcing generates barotropic tides (3.5 TW) primarily in the ocean, with 2.5 TW of barotropic tidal energy lost to bottom friction in shallow seas. Approximately 1 TW is converted to internal tides in the deep ocean, most of which enters the internal-wave-driven energy cascade from large scales to mixing scales. The wind provides about 1 TW into the internal wave spectrum. From Carter et al. (2012). 4

1.3 Time-mean spectrum of vertical displacements measured at approximately 3200 m in the open ocean. The Coriolis frequency f and the buoyancy frequency N denote the range where freely propagating energetic internal waves can exist. Additional vertical dashed lines represent the main internal tidal constituents that are the principal lunar semidiurnal tide M_2, the diurnal tide K_1 and the compound tide M_4 (=$2\times M_2$) of the semidiurnal tide. From Köhler (2013). . . 5

2.1 RMS amplitudes (m) of the M_2 internal tide obtained from (a) the 19-yr satellite altimetry data and (b) the 2-yr hourly sea surface height simulated by the STORMTIDE model. The M_2 tidal signals are high-pass filtered and then binned into 1° × 1° boxes. The black boxes mark the regions of hot spots used in Table 2.1. 19

2.2 Kinetic energy (cm^2 s^{-2}) of the M$_2$ internal tide in logarithmic scales at (a) 100 m and (b) 1085 m. (c) The vertical integral of the kinetic energy (J m^{-2}) in logarithmic scales, which is prepared in the same scales as used in Eden and Olbers (2014, their Fig. 5b). The kinetic energy at single depth is derived using $(A^2_{u_{bc}}+A^2_{v_{bc}})/2$, with $A_{u_{bc}}$ and $A_{v_{bc}}$ being amplitudes of the M$_2$ baroclinic zonal and meridional velocities, respectively. The vertical integral is then derived by $\int_{-H}^{0} \rho_w(A^2_{u_{bc}} + A^2_{v_{bc}})/2dz$ with ρ_w being the density of seawater. 27

2.3 Wavenumber spectra $S_{KE}(k,l)$ of the kinetic energy of the M$_2$ internal tide at (a) 100 m and (c) 1085 m in logarithmic scales in the 15°/$cos\varphi$ × 15° box centered at (170°W, 22.55°N). The resolved range of the zonal and meridional wavenumbers is within -0.045-0.044 km^{-1}. To enhance the readability, we only show the range of -0.025-0.025 km^{-1} that involves the most energetic motions and leave out wavenumber regions with very weak energy. In the right column, wavenumber spectra $S_{KE}(K)$ of the M$_2$ internal tide are shown at (b) 100 m and (d) 1085 m, converted from $S_{KE}(k,l)$ using $K=\sqrt{k^2+l^2}$ in the same box. The scattered blue dots are converted directly from each value of $S_{KE}(k,l)$. The red lines represent the bin averages of $S_{KE}(K)$, in which $S_{KE}(K_i)$ at the i^{th} interval is obtained by averaging all values of $S_{KE}(K)$ with K inside the interval (K_i,K_i+ $\triangle$). We consider a total of 100 consecutive intervals. Term $\triangle$ is obtained by dividing the total resolved wavenumber range by 100. 29

2.4 (a) Bin-averaged spectra $S_{KE}(K)$ of the horizontal kinetic energy of the M$_2$ internal tide derived for the 15°/$cos\varphi$ × 15° box centered at (170°W, 22.55°N). (b) shown are (right) the vertical modal structures of mode 1 (solid) and mode 2 (dashed) of the kinetic energy in the considered box, which are proportional to $[dw_m(z)/dz]^2$ with $w_m(z)$ being the eigenfunction of Eq. (2.5). These structures are derived by solving the Sturm-Liouville eigenvalue problem with (left) the box-averaged stratification profile simulated by the STORMTIDE model. . . . 31

2.5 Normalized spectral width (×10) derived from the mode 1 wavenumber spectra. The width is defined by the wavenumber interval between half of the peak energy, and is then normalized by the wavenumber related to the spectral peak. Nine-point smoothing has been performed after deriving the raw near-global map. 33

2.6 Distributions of the mode 1 wavelengths (km) for the M_2 internal tide as derived (a) by applying two-dimensional wavenumber spectral analysis to the M_2 baroclinic velocities at 100 m simulated by the STORMTIDE model for overlapping $15°/cos\varphi \times 15°$ boxes, (b) by numerically solving the Sturm-Liouville eigenvalue problem, and (c) by analytically solving the WKB-simplified eigenvalue problem. Both eigenvalue problems use the same stratification profiles averaged over the same boxes as used in the spectral analysis. 34

2.7 Distributions of the mode 2 wavelengths (km) for the M_2 internal tide. The same methods are used as described in Fig. 2.6, except that the spectral analysis is performed for the STORMTIDE M_2 baroclinic velocities at 1085 m for deriving $L_{ST,2}$. 35

2.8 Differences (%) between $L_{ST,m}$ and $L_{SL,m}$ $(m = 1, 2)$ for (a) mode 1 and (b) mode 2 normalized by values of $L_{ST,m}$. Red shading indicates that the values of $L_{ST,m}$ are larger than those of $L_{SL,m}$, whereas blue shading suggests the opposite. 37

2.9 Zonal-mean wavelengths of (a) mode 1 and (b) mode 2. The solid line represents $L_{ST,m}$, which is obtained from the STORMTIDE simulation, and the dashed line represents $L_{SL,m}$, which is derived by solving the Sturm-Liouville eigenvalue problem. 38

2.10 Zonal-mean wavelengths of (a) mode 1 and (b) mode 2 derived by the spectral analysis with the simulated M_2 baroclinic velocities (red), by setting constant N, hence constant ν_m in Eq. (2.7) (blue), by setting constant f in Eq. (2.7) with ν_m directly from solving the eigenvalue problem Eq. (2.5) (black). These wavelengths are normalized by their respective maximum. The latitude space is further divided into characteristic regions, denoted by A-C for mode 1 and denoted by A for mode 2, which are further described in the text. 39

2.11 Differences (%) between $L_{SL,m}$ and $L_{WKB,m}$ ($m = 1, 2$) for (a) mode 1 and (b) mode 2 normalized by the values of $L_{SL,m}$. Red shading indicates that values of $L_{SL,m}$ are larger than those of $L_{WKB,m}$, whereas blue shading suggests the opposite. 42

3.1 Kinetic energy (cm^2 s^{-2}) of the K_1 internal tide in logarithmic scales at (a) 100 m and (b) 1085 m, which are simulated by the 1/10° STORMTIDE model. They are derived by $(A^2_{u_{bc}} + A^2_{v_{bc}})/2$, with $A_{u_{bc}}$ and $A_{v_{bc}}$ being amplitudes of the K_1 baroclinic zonal and meridional velocities, respectively. (c) The vertical integral of the K_1 kinetic energy (J m^{-2}) in logarithmic scales derived by $\int_{-H}^{0} \rho_w (A^2_{u_{bc}} + A^2_{v_{bc}})/2dz$, with ρ_w being the density of seawater and H water depth. Boxes denote the regions in which the wavenumber spectra will be be introduced later. 51

3.2 Wavenumber spectra $S_{KE}(k,l)$ (m^2 s^{-2} km^{-1}, in logarithmic scales) of the kinetic energy of the K$_1$ internal tide in the 15°/$cos\varphi$ × 15° box centered at (135°E, 7.55°N) at (a) 100 m, (c) 560 m, and (e) 1220 m. The resolved ranges of k and l are within -0.045-0.044 km^{-1}, but we show only the energetic range of -0.025-0.025 km^{-1} to enhance the readability. In the right column, wavenumber spectra $S_{KE}(K)$ are converted from the respective $S_{KE}(k,l)$ using $K = \sqrt{k^2 + l^2}$. The scatters are converted directly from each value of $S_{KE}(k,l)$. The red lines represent the bin averages of $S_{KE}(K)$, in which $S_{KE}(K_i)$ at the i^{th} interval is obtained by averaging all values of $S_{KE}(K)$ with K inside the interval (K_i,K_i+ $\triangle$). We consider a total of 100 consecutive intervals. Term $\triangle$ is obtained by dividing the total resolved wavenumber range by 100. 54

3.3 Wavenumber spectra $S_{KE}(k,l)$ (m^2 s^{-2} km^{-1}, in logarithmic scales) of the STORMTIDE-simulated kinetic energy of the K$_1$ internal tide in the 15°/$cos\varphi$× 15° box centered at (110°W, 7.45°S) at (a) 100 m, (c) 740 m, and (e) 1365 m. In the right column, wavenumber spectra $S_{KE}(K)$ converted from the respective $S_{KE}(k,l)$ using $K = \sqrt{k^2 + l^2}$, with K, k and l being the horizontal, zonal and meridional wavenumbers, respectively. Other details are the same as described in Fig. 3.2. 57

3.4 Wavenumber spectra $S_{KE}(k,l)$ (m^2 s^{-2} km^{-1}, in logarithmic scales) of the STORMTIDE-simulated kinetic energy of the K$_1$ internal tide in the 15°/$cos\varphi$× 15° box centered at (165°E, 22.55°N) at (a) 100 m, (c) 845 m, and (e) 1365 m. In the right column, wavenumber spectra $S_{KE}(K)$ are converted from the respective $S_{KE}(k,l)$. Other details are the same as described in Fig. 3.2. . . . 59

3.5 (a) Bin-averaged spectra $S_{KE}(K)$ of the kinetic energy of the K_1 internal tide for the box centered at (135°E, 7.55°N). (c) The vertical modal structures of the first three modes of the kinetic energy in the considered box, which are proportional to $[dw_m(z)/dz]^2$ with $w_m(z)$ being the eigenfunction. These structures are derived by solving the Sturm-Liouville eigenvalue problem with (b) the box-averaged stratification profile simulated by the STORMTIDE model. The zero crossings of mode 1 to 3 diagnosed from the modal structures are at (1260 m), at (200 m, 1870 m), and at (120 m, 650 m, 2360 m), respectively. 60

3.6 The same as Fig. 3.5, but for the box centered at (110°W, 7.45°S). The zero crossings of mode 1 to 3 diagnosed from the modal structures are at (1280 m), at (280 m, 1900 m), and at (110 m, 740 m, 2270 m), respectively. 62

3.7 The same as Fig. 3.5, but for the box centered at (165°E, 22.55°N). The zero crossings of mode 1 to 3 diagnosed from the modal structures are at (1340 m), at (390 m, 2340 m), and at (190 m, 860 m, 2910 m), respectively. 63

3.8 Mode-1 wavelengths (km) of the K_1 internal tide, derived (a) by applying the spectral analysis to the STORMTIDE-simulated baroclinic tidal velocities at 100 m, (b) by solving the Sturm-Liouville eigenvalue problem with the box-averaged stratification that are simulated by the STORMTIDE, and (c) by solving the WKB-simplified Sturm-Liouville eigenvalue problem. The same box-averaged stratification has been used for both eigenvalue problems. 64

3.9 Mode-2 wavelengths (km) of the K_1 internal tide, derived by the same methods as described in Fig. 3.8. Instead of 100 m used for the simulated mode-1 wavelengths, (a) the simulated mode-2 wavelengths are derived at depths where the vertical modal structures of mode 2 undergo their respective interior maxima. 65

3.10 Mode-3 wavelengths (km) of the K_1 internal tide, derived by the same methods as described in Fig. 3.8. Instead of 100 m used for the simulated mode-1 wavelengths, (a) the simulated mode-3 wavelengths are derived at depths where the vertical modal structures of mode 3 undergo their respective second (deeper) interior maxima. 66

3.11 Relative discrepancies (%) between the simulated and theoretical wavelengths for (a) mode 1, (b) mode 2, and (c) mode 3, that is, $(L_{ST,m} - L_{SL,m}) \times 100/L_{ST,m}$, $m = 1, 2, 3$. Blue shading indicates that the values of $L_{ST,m}$ are larger than those of $L_{SL,m}$, whereas brown shading suggests the opposite. . . . 68

3.12 Zonal-mean wavelengths (km) of (a) mode 1, (c) mode 2, and (e) mode 3, derived from the model simulation (solid lines) and by solving the standard Sturm-Liouville eigenvalue problem (dashed lines). In the right column, comparisons of the normalized zonal-mean wavelengths of the simulation (red lines) with the ideal tests, for mode (b) 1, (d) 2 and (f) 3, by assigning constant N (blue lines) and f (black lines), respectively, when solving the standard Sturm-Liouville eigenvalue problem. These wavelengths are normalized by their respective maxima in order to bring them to a comparable range of 0-1. 69

3.13 Relative discrepancies (%) between $L_{SL,m}$ and $L_{WKB,m}$ for mode (a) 1, (b) 2, and (c) 3, respectively, that is, $(L_{SL,m} - L_{WKB,m}) \times 100/L_{SL,m}$, $m = 1, 2, 3$. Blue shading indicates that the values of $L_{SL,m}$ are larger than those of $L_{WKB,m}$, whereas brown shading suggests the opposite. 73

3.14 Vertical distributions of (a) the K_1 kinetic energy (J m^{-3}) in logarithmic scale, and (b) stratification (s^{-1}) over the section along (140°-170°E, 20.05°N) in the northern Pacific. Both plots are derived at the regular lonlat grid, i.e., $0.1° \times 0.1°$, which are converted from the non-regular model resolution. In (a), the black lines indicate internal wave beams, and the two boxes indicate the regional breakups of wave beams. 75

3.15 Vertical profiles of the K_1 kinetic energy at single points, located at (130°E, 20.05°N) (blue) and at (170°W, 20.05°N) (red), derived at the regular lonlat grid with a resolution of $0.1° \times 0.1°$. 76

3.16 Vertical distribution of the K_1 kinetic energy (J m^{-3}) at (160°E, 52.05°N). . . 78

3.17 Vertical distributions of (a) the K_1 kinetic energy (J m^{-3}) in logarithmic scale and (b) stratification (s^{-1}) for a section between 159°-175°E along 52.05°N in the northern Pacific. This section is located at poleward of the K_1 critical latitude ($\varphi_c = 30°$), and both distributions are derived from the distributions at the regular lonlat grid with a resolution of 0.1° × 0.1°. 79

3.18 Vertical distributions of (a) the kinetic energy (J m^{-3}) in logarithmic scale and (b) stratification (s^{-1}) between 140°-165°E along 52.05°S in the Southern Ocean poleward of the K_1 critical latitude. 80

3.19 Layer thickness (m) of the STORMTDIE model. Y-axis shows the averaged depths of every two neighbouring model layers. 81

3.20 Kinetic energy (J m^{-3}) of the K_1 internal tide above the bottom, divided by different water depths equatorward of the K_1 critical latitude at 30° for (a) shallower waters ($H < 2500$ m) and (b) deeper waters ($H > 2500$ m). In general, 500 m interval is employed in the separation of regions. Note the different scales of the x-axis in both plots. 83

3.21 The same as Fig. 3.20, but derived in regions poleward of the K_1 critical latitude at 30°. 84

3.22 Normalized kinetic energy (%) above the bottom, divided by different water depths, and normalized by their respective maximum in each water depth interval poleward of the K_1 critical latitude 30° for (a) shallower waters ($H < 2500$ m) and (b) deeper waters ($H > 2500$ m). In general, 500 m interval is employed in the separation of regions. 85

A.1 Spectral width (× 1000, km^{-1}) derived from the kinetic energy spectra $S_{KE}(K)$ at 100 m of the mode-1 M_2 internal tide by using the previous method. The width is defined by the wavenumber internal between half of the peak energy. Nine-point smoothing has been performed after deriving the raw near-global map. 97

A.2 Time-mean wavenumber spectra $S_{u_{bc}}(k,l)$ of the M_2 baroclinic zonal velocity u_{bc} at (a) 100 m and (c) 1085 m, and (b, d) the corresponding spectra $S_{u_{bc}}(K)$ converted from $S_{u_{bc}}(k,l)$ using $K = \sqrt{k^2 + l^2}$, derived for the 15° × 15° box centered at (167.5°W, 22.55°N). The scattered blue dots are converted directly from each value of $S_{u_{bc}}(k,l)$. The red lines represent the bin averages of $S_{u_{bc}}(K)$, in which $S_{u_{bc}}(K_i)$ at the i^{th} interval is obtained by averaging all values of $S_{u_{bc}}(K)$ with K inside the interval (K_i,K_i+ $\triangle$). We consider a total of 100 consecutive intervals. Term $\triangle$ is obtained by dividing the total resolved wavenumber range by 100. 98

A.3 Tukey window function that is used in our analysis. 99

B.1 Mode-1 wavelengths $L_{SL,1}$ (km) of the M_2 internal tide in a 1° × 1° resolution derived by solving the Sturm-Liouville eigenvalue problem (a) with the box-averaged stratification of the model simulation and (b) with the stratification derived from the Levitus temperature and salinity. 103

B.2 (a) Mode-1 and (b) mode-2 wavelengths (km) of the M_2 internal tide derived from the baroclinic tidal velocities simulated by the STORMTIDE model. The box size of 15° × 15° is employed with the data interpolated onto the regular lonlat grid of 0.1°. 104

C.1 Kinetic energy (cm^2 s^{-2}, in logarithmic scales) of the M_2 internal tide at (a) 100 m and (c) 1085 m, simulated by the 0.4°-resolution MPI-OM, in which tides are implemented. The kinetic energy distributions from the same model simulation are shown at (b) 100 m and (d) 1085 m for the K_1 internal tide. . . 107

C.2 (a) Amplitudes (cm) and (b) phases (degree) of the K_1 baroclinic zonal velocities at 100 m that are simulated by the 0.4°-resolution MPI-OM, in which tides are implemented. 108

List of Tables

2.1 The surface signals (cm) of the M_2 internal tide averaged as quantities by RMS over various hot spots regions indicated in Fig. 2.1. TPJ and STORMTIDE refer to the observations and model simulation, respectively. The last column shows the RMS ratios of observations to model results. 20

Acknowledgements

Foremost I would like to thank my advisors Jin-Song von Storch and Malte Müller for their continuous guidance and support in my research. Their efforts in taking the arduous job of advising me during my PhD research makes it possible for this thesis to see the light of the day. I really appreciate the patience, encouragement, appropriate push and trust from Jin-Song, which gives me the courage for being independent. I benefit not only from her vast knowledge, but also from her attitude that is curious and enthusiastic towards the basic science. I thank Malte for sharing his model simulation, Matlab codes with me, and for his patient explanations when I have questions even though we basically have to discuss via email. His interest in tides encourages me to pursue further.

I am very grateful to Jochem Marotzke for serving as my panel chair and taking the responsibility to supervise the whole process of my research, who is in charge only to make sure that my project turns out to be a success for me.

Special thanks to Carsten Eden for his constructive comments and suggestions on Chapter 2, and for his willingness to serve as one of my thesis evaluator. Many thanks to Helmuth Haak for all the technical support.

I would like to express my gratitude to the International Max Planck Research School on Earth System Modelling (IMPRS-ESM). I really appreciate the opportunity to be a part of the IMPRS. My sincere thanks to Antje Weitz for her valuable advice on finishing the thesis and on my job hunting, and also for being always available when I have questions or doubts during the final days as a PhD, which helped me to put a foot down in science more firmly. I thank Wiebke Böhm and Cornelia Kampmann for

all the support I received in the past years. They have done a great job in organizing the wonderful annual IMPRS retreat, from which I benefit by presenting, listening and communicating.

I take the chance to thank Christina Rieckers for being always kind and helpful ever since I came to Germany. All her efforts made my life much easier and more comfortable to study and live in Germany.

I express my gratitude to Josiane Salameh, Jan Ackmann, Hongmei Li and Fangxing Tian for being my office mate and for the joyful time we spent together.

My sincere thanks to my fellow students and friends, Chao Li, Feifei Liu, Xueyuan Liu, Thomas Keitzl, Mirjana Sakradzija, Philipp Johannes Griewank and the IMPRS fellows for their kindness, support and help.

My deepest gratitude goes to all the brothers and sisters in HIM I've met in Hamburg and Kiel. My life has been totally changed when I met them in HIM. My lovely wedding would be impossible without their love, support and help.

I would like to thank my parents for their unconditional love and support, encouragement and trust. Thanks to my brothers and sisters who are willing to take the responsibilities to take care of our parents and parents-in-law so that we can pursue our study in Germany with no worries. I thank my niece for being so lovely and bringing so much happiness to our family. My special thanks to my dear husband Guidi for being by my side through my life in Germany. Thanks to him for all the care, support, and the endless love.

Finally, I am grateful to the China Scholar Council for the supporting my study in Germany financially.

List of publications

- Chapter 2: **Li, Z.**, J.-S. von Storch, and M. Müller, 2015: The M_2 internal tide simulated by a 1/10° OGCM, *J. Phys. Oceanogr.*, **45**, 3119-3135, doi:10.1175/JPO-D-14-0228.1.
- Chapter 3: **Li, Z.**, J.-S. von Storch, and M. Müller, 2016: The K_1 internal tide simulated by a 1/10° OGCM, in preparation.

Eidesstattliche Versicherung

Declaration on oath

Hiermit erkläre ich an Eides Statt, dass ich die vorliegende Dissertationsschrift selbst verfassst und keine anderen als die angegebenen Quellen und Hilfsmittel benutzt habe.

I hereby declare, on oath, that I have written the present dissertation by myself and have not used other than the acknowledged resources and aids.

Hamburg, den ________________

____

Zhuhua Li